Modeling and Optimal Control of Parallel HEVs and Plug-in HEVs for Multiple Objectives

by

Dongsuk Kum

A dissertation submitted in partial fulfillment
of the requirements for the degree of
Doctor of Philosophy
(Mechanical Engineering)
in The University of Michigan
2010

Doctoral Committee:

Professor Huei Peng, Chair
Professor Zoran S. Filipi
Professor Jing Sun
Professor A. Galip Ulsoy

To my parents, my lovely wife Seungyoun Lee, and parents-in-laws

ACKNOWLEDGEMENTS

I would like to express my earnest gratitude to my advisor, Professor Huei Peng. His guidance, assistance, patience, and encouragement have been of enormous importance to my research and the completion of the dissertation. I would also like to thank my other committee members, Professor Zoran Filipi, Professor Galip Ulsoy, and Professor Jing Sun, for their helpful advices.

I am indebted to Dr. Norman Bucknor and Dr. Madhu Raghavan from General Motors R&D for their academic inputs and financial support during my doctoral studies.

It has been a great pleasure working in the Vehicle Dynamics Lab as a doctoral student. Many thanks to my fellow graduate students for their help, discussion, and all the good times we have had in the office: Jinming Liu, Daekyun Kim, Minjoong Kim, Jing Zhou, Yong-Song Chen, Youseok Kou, Jeong-Seok Kim, Sehyun Chang, Sean Yang, Gayathri Seenumani, Changsun Lee, Chiao-Ting Li, and Namwook Kim.

Finally, my deepest thanks to my parents for all the love and support they have given me. I would also like to thank my wife, Seungyoun Lee, for her support and companionship.

TABLE OF CONTENTS

LIST OF FIGURES

LIST OF TABLES

ABSTRACT

The sharp rise in fuel prices and deteriorating environmental conditions over the last decade motivated automobile manufacturers to develop fuel efficient and clean automobiles. As a promising technology, hybrid electric vehicles (HEV) have been successfully introduced to the consumer market. In addition, the Plug-in HEV (PHEV), which can avoid fuel use and tail-pipe emissions by using grid electricity as the main source of energy within its designed "all electric range", is expected to be launched in late 2010. These advanced vehicles require sophisticated design methods to optimize and balance multiple performance objectives due to the system complexity and an additional control degree of freedom. Past studies have focused on fuel economy, and other vehicle performance metrics, such as emissions, drivability, and NVH (noise, vibration, and harshness) received much less attention, despite their practical significance. The main goal of this doctoral study is to develop models and systematic design methods that optimize multiple objectives, including fuel economy, emissions, and drivability, for both HEVs and Plug-in HEVs (PHEVs).

This dissertation investigates three optimal control problems; 1) optimal control of HEVs for fuel economy and emissions, 2) optimal control of PHEVs for fuel economy and emissions, and 3) optimal control of rapid engine-starts for drivability. The first two problems optimize fuel economy and tail-pipe emissions simultaneously for selected drive cycles, but the engine-start control problem has a much shorter horizon and can be designed separately.

For the simultaneous optimization of fuel economy and emissions, we first develop a parallel HEV (and PHEV) model that can efficiently evaluate both fuel economy and tail-pipe emissions, and then solve the optimal control problem that minimizes fuel consumption and emissions for a cold-start driving cycle using Dynamic Programming (DP). Based on DP results, a

comprehensive extraction method is developed to extract implementable optimal control strategies over the entire state space, instead of a single optimal trajectory. This method is applied to both HEVs and PHEVs to extract both optimal energy management and catalytic converter temperature management strategies. For the optimal energy management of PHEVs under known trip distances, a new variable Energy-to-Distance Ratio (EDR) is introduced to quantify the level of battery state-of-charge (SOC) with respect to the remaining distance. The extracted results show that the engine on/off, gear-shift, and power-split strategies must be properly adjusted to optimize fuel economy and tail-pipe emission. Based on the extracted results, a DP-based cold-start supervisory powertrain controller (SPC) is designed and compared with instantaneous optimization methods. Simulation results show that instantaneous optimization methods are good for the optimization of fuel economy despite frequent engine on/off and gear-shift events, but the DP-based SPC performs better when multiple objectives are considered.

For the engine-start control problem, a more detailed powertrain model, including clutch and crank-angle domain engine models, is developed. Assuming that the clutch torque can be accurately estimated and perfectly cancelled, the optimal engine-start control problem is formulated to minimize engine-start time while accurately supplying the driver torque demand. This nonlinear optimal control problem is solved both analytically and numerically. Under special cases, the optimization problem can be analytically solved to obtain a closed form solution. DP, on the other hand, is used to obtain numerical solutions for all cases, and the results confirm that the numerical solution matches with the analytical solution. More importantly, the DP control policy is found to be time-invariant, and thus can be directly implemented in the form of a full state feedback controller.

CHAPTER 1
INTRODUCTION

1.1 Motivations

An important event that happened over the last decade in the automotive world was the introduction of Hybrid Electric Vehicles (HEVs) to the consumer market. HEVs attracted public attention and have been successful in the market due to the sharp rise of fuel prices. High fuel prices motivated many researchers in both industry and academia to focus on the fuel economy of HEVs. While fuel economy is important for HEVs, other vehicle performance metrics, such as emissions, drivability, as well as noise, vibration, and harshness (NVH), are also very important due to emission regulations and consumer perceptions. However, optimizing these performance metrics are more difficult to achieve than optimizing fuel economy alone because corresponding models and optimal control problems are more complex. In addition, optimized design for a single objective may lead to poor performance of others, and these objectives must be properly coordinated for optimal and balanced performance. The main goal of this doctoral study is to develop models and systematic design methods that optimize multiple performance objectives, including fuel economy, emissions, and drivability for the HEV and Plug-in HEV (PHEV). In the following subsections, these performance objectives are discussed in order to illustrate the detailed motivations of this study.

1.1.1 Fuel Economy

Fuel economy has been a major focal point in the automotive world over the last decade, and has been a mainstream research area of the HEV [8,22,52,54,68,77,79]. In spite of numerous

efforts to reduce fuel consumption, the improvement in fuel economy of HEVs will eventually reach a plateau. On the other hand, the number of automotive vehicles has been rapidly growing and is expected to grow in the future as Figure 1.1 shows. As a result, the global oil dependency of the transportation sector is also expected to increase unless the main source of energy is replaced by another, e.g. electricity.

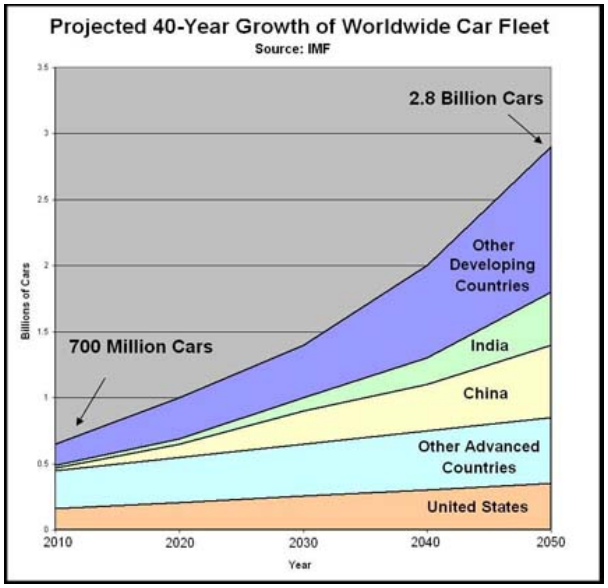

Figure 1.1: Projected number of global vehicles [60]

Recently, Plug-in Hybrid Electric Vehicles (PHEVs) have received much attention as a promising technology to dramatically lower ground transportation's dependency on fossil fuel and to reduce carbon dioxide (CO_2) emissions. The dramatic reduction in fossil fuel consumption in PHEVs is achieved by substituting fossil fuels with grid electricity. As an example, when the All Electric Range (AER) of a PHEV is 30 miles, it will be possible to use little or no fossil fuel from the tank when the travel distance is less than 30 miles, assuming the electric power source is capable of satisfying the propulsion power need. When the trip distance exceeds the AER, and especially when emissions are considered, the optimal control of the PHEV is non-trivial–an energy management strategy that properly blends the electric energy and the internal combustion engine is necessary. In this study, we seek to develop a systematic method for the synthesis of the

supervisory powertrain controller (SPC) to achieve near-optimal fuel economy and emission performance of a PHEV regardless of trip distance.

1.1.2 Emissions

Over the past few decades, environmental concerns and awareness have increased around the globe. Driven by these concerns, many countries have enforced ever-tightening emission regulations on automobiles, a major source of air pollutants [12,23,98]. Since automobile manufacturers are not allowed to sell vehicles that do not comply with these regulations, these rules must be considered in the design of vehicles. With the recent introduction of HEVs, manufacturers now have the option to leverage hybrid technology to follow these stringent emission standards. In the following, the emission standards of the United States are summarized.

a) Federal standard

In 1990, two federal emission standards Tier 1 and Tier 2 were defined as an amendment to the Clean Air Act (CAA) and consecutively implemented [40]. The Tier 1 standard was gradually phased-in starting in 1994, and took full effect from 1997 through 2004 [23]. Tier 1 was a weight-based standard, which had a single emission certification level for each class of vehicle weight. On the other hand, Tier 2, which phased-in from 2004 and took full effect in 2007, is a fleet-average program. The fleet-average program requires that all vehicles sold by a manufacturer must have the average Nitrogen Oxides (NO_x) emissions below 0.07g/mi. In addition to the average requirement, all new vehicles are categories into one of the certification levels, called Bins. Tier 2 is composed of 8 permanent Bins (1~8) and 3 temporary Bins (9~11), 1 being zero emission and 11 being the dirtiest certification. Bins 9~11 were temporarily available during the phase-in period along with relaxed fleet-average requirements to give manufacturers time to adapt to the new standard. Each Bin specifies limits of five harmful exhaust gases listed as follows [34,40].

- Non-Methane Organic Gases (NMOG): are precursors to the formation of ground-level ozone which leads to smog. Hydrocarbons are considered as NMOG.
- Carbon Monoxide (CO): competes with oxygen in the bloodstream and is especially dangerous to those with heart disease.
- Nitrogen Oxides (NO_x): causes ground level ozone which aggravates respiratory conditions and causes smog. NO_x also contributes to acid rain.
- Particulate Matter (PM): has been shown to affect the respiratory function and has been found to be carcinogenic in some studies.
- Formaldehyde (HCHO): can irritate the eyes and mucous membranes; cause headaches, allergies and trigger or aggravate asthma symptoms.

Table 1.1 shows details of the eight permanent Bins of Tier 2 standard. The average NO_x requirement of 0.07g/mi is comparable to Bin 5. Thus, if a manufacturer sells a vehicle certified as Bin 8, it must be offset by selling a sufficient number of cleaner vehicles certified as Bin 4 or below [40].

Table 1.1: Tier 2 emission standards for passenger cars and Light-Duty Trucks, FTP 75 [40]

	miles	Bin 8	Bin 7	Bin 6	Bin 5	Bin 4	Bin 3	Bin 2	Bin 1
NMOG	50k	0.100	0.075	0.075	0.075				
	120k	0.125	0.090	0.090	0.090	0.070	0.055	0.010	0
CO	50k	3.4	3.4	3.4	3.4				
	120k	4.2	4.2	4.2	4.2	2.1	2.1	2.1	0
NO_x	50k	0.14	0.11	0.08	0.05				
	120k	0.20	0.15	0.10	0.07	0.04	0.03	0.03	0
PM	120k	0.02	0.02	0.01	0.01	0.01	0.01	0.01	0
HCHO	50k	0.015	0.015	0.015	0.015				
	120k	0.018	0.018	0.018	0.018	0.011	0.011	0.004	0

b) California's standard

California was granted to develop its own emission standards due to the severity of the state's air pollution [97]. As a result, the California Air Resources Board (CARB) has been setting state emission standards more stringent than the federal standard, and other states may choose to adopt

California's standards at their will. In 1990, the CARB adopted the Low-Emission Vehicle (LEV) standard, which phased-in with Tier 1. The LEV was a fleet-average standard similar to Tier 2, but the restriction was applied to NMOG instead of NO_x. For gasoline engines, hydrocarbon (HC) dominates the total amount of NMOG, and the yearly-tightening average NMOG restriction, shown in Figure 1.2, is one of the key challenges manufacturers face.

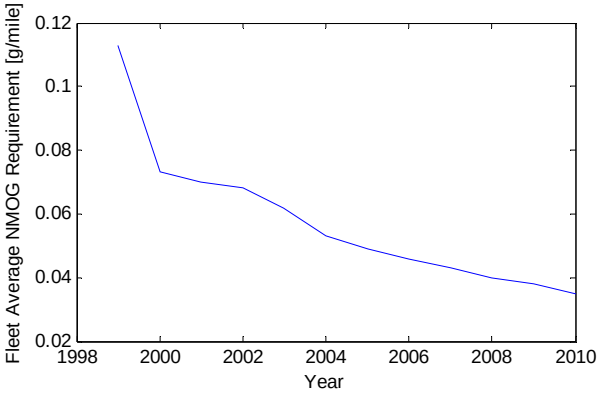

Figure 1.2: Fleet average California NMOG requirements

In 1998, the LEV was amended to define the LEV II standard, as shown in Table 1.2. The phase-in period of LEV II started in 2004 along with the Tier 2, and took full effect in 2007.

Table 1.2: LEV II standards for passenger cars and Light-Duty Trucks (LDT), FTP 75 [40]

	miles	**LEV**	**ULEV**	**SULEV**	**ZEV**
NMOG	50k	0.075	0.040		0
	120k	0.090	0.055	0.01	
CO	50k	3.4	1.7		0
	120k	4.2	2.1	1.0	
NO_x	50k	0.05	0.05		0
	120k	0.07	0.07	0.02	
PM	50k	0	0		0
	120k	0.01	0.01	0.01	
HCHO	50k	0.015	0.008		0
	120k	0.018	0.011	0.004	

Supplemental requirements of LEV II include:

- 10% Zero Emission Vehicle (ZEV) production requirement
- Extended durability limit of 120k miles

These requirements coupled with the fleet-average NMOG requirement make the LEV II standard the most stringent emission standard in the world. Fortunately, the 10% ZEV production requirement can be credited with production of Partial ZEV (PZEV) or Advanced Technology PZEV (AT-PZEV) up to 60%. Typically, PZEV applies to gasoline-fueled vehicles with comprehensive after-treatment system, and AT-PZEV applies to HEVs or vehicles using alternative fuels [40]. In summary, the emission goals of many HEVs including PHEVs are meeting the AT-PZEV certification, which requires SULEV certification with near-zero evaporative emissions and extended durability of 15 years/150k miles.

Optimizing energy management strategy of HEVs and PHEVs for fuel economy does not necessarily optimize tail-pipe emissions because they are mainly emitted during cold-start before the three-way catalytic converter (TWC) reaches the light-off temperature. Therefore, fuel efficient engine operation and frequent engine shut-off during cold-start are not the best strategy for fast catalyst warm-up and will hurt emissions. In this study, we seek to develop an emission model and a control strategy that simultaneously optimizes emissions and fuel economy of HEVs and PHEVs for a cold-start by the catalyst temperature management.

1.1.3 Drivability

Despite significant increases in recent sales of hybrid electric vehicles (HEVs), the profits on these vehicles are low due to the high cost of the electric motors, batteries, and power-electronics. It is thus important to identify cheaper and higher value-added hybrid vehicle designs. As a more practical near-term solution, the pre-transmission parallel HEV configuration (P2) offers a cost-effective alternative with a single motor/generator (M/G). However, this configuration suffers a drivability issue during engine-starts because the single motor must simultaneously provide the traction torque as well as to start the engine via an engine-disconnect clutch without perceptible levels of noise, vibration, and harshness (NVH), especially in the form of driveline torque ripple. Drivability and NVH are non-negotiable performance measures because they are highly related to

perceived vehicle quality and have direct impacts to reliability and repair. In this study, we focus on drivability aspect of the engine-start control and seek to develop models and design methods that can be used to obtain a control strategy with optimal or sub-optimal drivability.

Note that the time-horizon of this control problem is very short. Therefore, it is not necessary to consider fuel economy and emissions in the design of the engine-start. Instead, they could be determined either before or after the HEV/PHEV power management control design.

1.2 Mathematical Background

Many of the existing HEV control strategies have been developed based on optimal control theories. Three optimal control theories that are widely used are discussed in this section. Readers are referred to the Appendix for more details.

1.2.1 Classical Optimal Control Theory: Variational Approach

The variational approach is widely used in various applications, including the HEV control problem, owing to its elegant mathematical formulation and results. The main feature of the variational approach is that it converts the optimal control problem into a two-point boundary value problem, which is solvable. However, this approach does not guarantee the globally optimal solution because the necessary conditions are developed based on the first order calculus of variations. In addition, the two-point boundary value problem often must be solved iteratively to find the solution. Despite these disadvantages, it is a very useful tool to solve the optimal control problem and will be extensively used in this study.

As an example, the Equivalent Consumption Minimum Strategy (ECMS) is a well-known energy management strategy of conventional HEVs for the optimization of fuel economy, which is a special case of the Variational Approach [80]. The idea behind instantaneous optimal control approaches is that instantaneously optimized control commands may result in near-optimal performance over the entire horizon. The near-optimality is true when the open circuit voltage

and internal resistance maps are not functions of the battery State-of-Charge (SOC) [80]. However, the near-optimality no longer holds when horizon-based performance objectives (e.g. emissions and drivability) are considered. For instance, tail-pipe emissions are highly correlated with the catalyst temperature, and this leads to a dynamic costate. This two-point boundary value problem must be numerically solved by an iterative search algorithm, and the results guarantee neither convergence nor global optimality.

1.2.2 Deterministic Dynamic Programming

Another widely used optimization algorithm is Deterministic Dynamic Programming (DDP or DP). Unlike the variational approach, DP searches all possible solutions in a more efficient way than enumeration using the Principle of Optimality [4,6,41]. Thus, the main advantage of DP over the variational approach is that the global optimality is guaranteed even for non-convex constrained nonlinear optimal control problems, and it is often used to obtain performance limits. A major drawback is that its computational efforts increase exponentially with the number of state and control variables, also known as the curse of dimensionality [4,5,41]. Thus, DP can be a very powerful tool to find the globally optimal solution, but only for nonlinear optimal control problems with a low number of states and inputs. Another disadvantage is that the resulting optimal control sequence often cannot be directly implemented, and the optimal strategy needs to be properly analyzed and extracted from DP results to design a real-time controller.

1.2.3 Stochastic Dynamic Programming

Stochastic Dynamic Programming (SDP), also known as Markov decision processes, is a variation of DP developed to optimize stochastic systems that can be described by the Markov Chain [4,6,49,71]. As a matter of fact, Bellman first developed SDP, and the DDP problem was defined and solved later [4]. The underlying concept of SDP is also the principle of optimality. The main advantage of this method is that the stochastic nature of real-world problems can be included in the optimal control problem, and the resulting optimal control policy is robustly

optimal for the stochastic process included in the model. Another important strength of SDP is that the output of the algorithm, which is in the form of a full-state feedback controller, can be directly implemented. The main drawbacks of SDP are that the system must be described by the Markov Chain in order to apply this method, and the performance of the optimal control policy is optimal for the given Markov Chain, but not for any deterministic case. In other words, the optimal control policy of SDP will perform near-optimally under various scenarios, but will experience some loss of optimality compared to DDP results for a specified scenario. In addition, SDP also requires heavy computations. Although SDP is a powerful optimization algorithm that outputs an optimal control policy that can be directly implemented with robust performance under uncertainties, DDP will be used in this study for detailed engineering insights via the extensive analysis of optimization results.

1.3 Literature Review

1.3.1 Emission Model and Control

Modeling and simulations are essential tools for the design and control studies of HEVs. Unlike fuel economy, modeling and control studies for emission reduction relatively have not received much attention despite of their importance. In this section, existing emission models and control studies in the literature are summarized.

a) Emission models

To develop a powertrain and after-treatment model for the supervisory emission control strategy of HEVs, existing emission reduction techniques and models must be understood. Since the source of emissions for a parallel HEV is the Internal Combustion Engine (ICE), it is logical to investigate how conventional vehicles reduce tail-pipe emissions using the Three-Way Catalytic Converter (TWC), which is activated only after the catalyst brick temperature reaches the light-off temperature [9,78,85].

A number of researches investigated the physics of the TWC and developed chemical kinetics based models, which describe the heat and mass transfer in the after-treatment system and conversion efficiency as a function of the catalyst brick temperature and A/F ratio [16,17,38,43,51,70,86,87,101]. Koltsakis *et al*. proposed a detailed 2-D exhaust pipe and TWC model based on fundamentals of mass, heat transfer, and chemical kinetics [43]. They also discussed its possible applications including emissions prediction over driving cycles and assessment of fast light-off techniques. Due to its heavy computational demand, researchers often used this model as a basis to develop 1-D exhaust system models. Multiple variations of the model have been developed by different groups of researchers with slightly different focuses and levels of details [16,17,38,51,86,101]. Throughout these studies, a common objective was to efficiently evaluate tail-pipe emissions for after-treatment design purposes, and these models are usually too complex for control studies.

As an alternative for the 1-D models, Eriksson proposed a mean value model to predict exhaust system temperatures via a lumped parameter approach [24]. Another simplified exhaust system model proposed by Murrell *et al*. utilizes engine thermal networks and empirical data to describe exhaust system temperatures for rapid cold-start performances over different driving cycles [62]. These two models are sufficiently simple and yet accurate enough for control studies.

Recently, control-oriented TWC models were proposed. Studies by Brandt *et al*. and Sun *et al*. initiated interest in the control-oriented TWC model [9,90]. Sun *et al*. discussed the cold-start emission control problem and the trade-off between the rapid catalyst light-off and tail-pipe HC reduction [90]. Brandt *et al*. developed a control-oriented TWC model for tail-pipe emissions reduction of conventional vehicles via A/F ratio and spark ignition control [9]. This model has been further improved [75,76,83,84,85]. These models are very useful for low-level control because they captured the effect of A/F ratio and spark timing on exhaust gas temperature, which can then be used to control catalytic converter temperature during a cold-start.

b) Emission controls

A few HEV studies considered emissions and analyzed the trade-off between fuel economy and emissions [37,42,52,55,92]. However, most of the past studies considered the minimization of fuel consumption and engine-out emissions, instead of tail-pipe emissions [37,52,55]. Although reducing engine-out emissions helps to reduce tail-pipe emissions for extended driving cycles, reduction of engine-out emissions is not the key to tail-pipe emissions reduction for the normal use of vehicles. Since emission conversion efficiency of a cold TWC is very limited, fast catalyst warm-up and catalyst temperature management are the key to minimizing total tail-pipe emissions. Therefore, the thermal transient dynamics of engine and after-treatment systems must be considered in order to properly evaluate and reduce tail-pipe emissions. A study by Kolmanovsky *et al*. [42] considered catalyst temperature as a dynamic state for a simplified hybrid powertrain model, and the optimal fuel economy problem with maximum NO_x constraint was solved by SQP, which is a local search algorithm. A study by Tate *et al*. [93] formulated the tail-pipe emission control problem for HEVs and solved it by shortest-path stochastic dynamic programming (SP-SDP), using a simplified after-treatment model. The study demonstrated that reduction of tail-pipe emissions trades off with fuel economy, but a steady-state (hot) engine was assumed and no analysis was discussed about the optimal control strategy and results.

1.3.2 Plug-in HEVs

Past PHEV studies can be classified into three areas; 1) energy and environmental impact, 2) design, and 3) control studies. The literature will be given separately in these sub-topics.

a) Energy and environment impact

The focus of the early studies of PHEVs has been in the energy and environmental impact areas to assess the feasibility of the PHEV concept. Bradley and Frank surveyed the literature and summarized that the reductions in fuel consumption and CO_2 of a PHEV are around 51-88% and 40-67%, respectively, depending on design, driving conditions, and electricity sources [7]. Other

studies discussed improvements in fuel economy (FE) and CO_2 at different levels of electrification of vehicles, from conventional vehicles to HEV, PHEV, and Extended-Range Electric Vehicles (E-REVs) [93,94]. These studies focused on tank-to-wheel FE analysis, but a broader view of the energy and emission analysis is necessary for nationwide feasibility of the PHEV. A number of studies performed well-to-wheels energy and greenhouse gas analysis and concluded that the choice of electricity sources is critical for reduction of CO_2 when a large number of PHEVs are introduced [25,45,74,89,106].

b) Design

Assuming that use of grid electricity for transportation energy is viable and beneficial, significant research has been conducted on the design and its influence on performance and cost of the PHEV for assessment of its market penetration. The National Renewable Energy Laboratory (NREL) and Argonne National Laboratory (ANL) conducted studies that focused on the component sizing problem and its influence on fuel economy and cost. These studies concluded that a smaller battery with a low power-to-energy (P/E) ratio is desirable for near-future market penetration, because a smaller battery leads to much lower battery and power electronics cost with little reduction in FE for typical daily driving [58,88]. Other studies also reached similar conclusions from the fact that many people drive less than 30km each day and operate under 40kw of propulsion power, based on a daily driving distance and propulsive power distribution analysis [44,81]. However, aggressiveness of driving cycles influences these analyses and should be considered during the vehicle design process [50,26,15]. Another important design decision, powertrain configuration, has also been studied [28,39].

c) Control

Despite extensive research in control of the HEV, a relatively small number of studies have been conducted for the PHEV. The focus of the PHEV control studies is how to distribute the available battery energy throughout the driving cycle when the travel distance exceeds the AER, while control strategy for trips shorter than AER is trivial: the minimum engine use. Gonder and

Markel proposed and compared three control strategies, electric vehicle/charge sustaining (EV/CS), engine-dominant, and electric-dominant strategy [30]. Since performance of each strategy is sensitive to trip distance and driving conditions, they suggested that the control strategy can be manually or automatically switched from one to another for improved FE based on the future driving information. Another study by Sharer *et. al*. performed similar analysis on EV/CS, full engine power, and optimal engine power strategies, and emphasized sensitivity of their performances with respect to travel distances [82]. These strategies are designed based on engineering intuition and do not guarantee optimality. Recent study by Moura *et. al*. used the stochastic dynamic programming approach to solve the optimal control problem of the PHEV [61]. However, the stochastic approach does not properly address the dependency of the optimal SOC management on various travel distances exceeding AER despite their importance.

When emissions are considered, the optimal control problem becomes an even more complex problem to solve because the PHEV is designed to reduce fuel consumption by frequent and extended engine shut-down. The study by Carlson *et. al*. showed that PHEVs may produce more noxious emissions than conventional HEVs, if not carefully designed and/or controlled [14].

1.3.3 Engine-start Control

Optimal fuel economy and/or emission have been the mainstream research focus of HEV control in the past. Few drivability studies exist in the literature despite of its importance. A recent study by Canova *et al*. investigated the engine-start control problem of the belted starter/alternator (BSA) diesel HEV [13]. They developed a BSA-engine system model and a closed-loop controller that starts the engine following a given speed profile. Another study by Zhang *et al*. conducted experiments to analyze jerk responses of an integrated starter/generator (ISG) HEV as a measure of drivability during shifts and powertrain mode changes [108]. These BSA/ISG HEVs have a dedicated electric starter at an additional cost, and the difficulty of the clutch-controlled rolling-start with a single electric motor is not present. Several studies

addressed the difficulty of the engine-start control for the P2 configuration [18,67]. Colvin *et al*. conducted tests to show that the desired level of drivability was achieved by using proper control strategies in various real-world scenarios [18]. The authors intentionally slip the input clutch (between the transmission and motor) to dampen out the vibration during a rolling-start. This is certainly a good way to reduce NVH, but it comes at the cost of reduced responsiveness because an increase in the driver torque demand will be difficult to meet with the input clutch slipping. Several other engine-start control studies focusing on NVH can be found in the literature [104,46,35]. The scope of this study, however, is limited to drivability, and the focus is on the optimization of vehicle drivability, which is characterized by two measures; engine-start time and torque error between the demanded and supplied torque.

1.4 Contributions

In the previous sections, we reviewed the literature in modeling and control of HEVs and PHEVs for fuel economy, emissions, and drivability. It is clear that past studies mainly focused on fuel economy, and other performance metrics received less attention. In particular, models and design methods for optimization of these performance objectives were not adequately studied. The following list shows the main contributions of this work.

- **Development of a simplified cold-start tail-pipe emission model**

The lack of a computationally efficient emission model hindered studies in the design and control of HEVs for emission reductions. The main reasons for this are complicated and highly transient mechanisms of the combustion and after-treatment. By focusing on catalyst temperature dynamics and conversion efficiency, a simplified but sufficiently accurate model was developed. A supervisory control algorithm for emission reduction is also formulated.

- **Development of a comprehensive extraction method**

Use of Dynamic Programming (DP) has been limited due to its difficulty with real-time control implementations, and often it is only used to find the achievable performance benchmark. In order to make further use of the DP results for the design of a real-time controller, an extraction method was previously developed to extract an implementable near-optimal control strategy based on a single optimal trajectory [52]. This method, however, does not provide enough information during the cold-start phase due to the short warm-up time, and a comprehensive extraction method is proposed. This new extraction method utilizes all of the optimal control information found from the DP to reconstruct a near-optimal controller that covers the entire state space. The concept of the comprehensive extraction method is generic and can be applied to other DP problems.

- **Introduction of Energy-to-Distance Ratio (EDR) for control of PHEVs**

Under various trip distance and SOC conditions, a supervisory powertrain controller (SPC) of PHEVs needs to adjust its control strategy for optimal fuel economy and emission performance. Assuming that the remaining trip distance is known, a new variable Energy-to-Distance Ratio (EDR) is introduced in order to quantify the level of battery SOC with respect to the remaining trip distance. This variable is found to play an important role in adjusting the SPC of PHEVs for optimal fuel economy and emission performance. In particular, the cold-start control strategy needs to be properly adjusted under various EDR conditions.

- **Identification of the importance of the optimal engine on/off and shift strategies**

The engine on/off and shift strategies are often left out, and pre-determined control strategies are used when the optimal control problems of parallel HEVs are formulated. In this study, these control variables are included in the optimal control problem, and the results show that they are crucial control variables in optimizing multiple performance objectives. In addition, these control variables must be adjusted to optimize emissions and fuel economy of PHEVs under various SOC and travel distance conditions as well as emissions.

- **Development of an adaptive DP-based SPC algorithm**

The instantaneous (static) optimization method inherently has difficulty dealing with horizon performance metrics such as emissions and drivability, and the modification of individual control variables without loss of optimality is difficult to achieve. For instance, late-shift for fast catalyst warm-up or avoiding gear-shifts for drivability will likely lose optimality. Based on DP results, an adaptive near-optimal SPC algorithm is proposed. Owing to its modular control architecture, this algorithm can be easily adjusted to optimize multiple performance objectives without a significant loss of optimality.

- **Modeling and optimal control of the engine-start for drivability of parallel HEVs**

Control of the engine-start has been a challenging control problem of parallel HEVs due to drivability and NVH issues. Fast engine-clutch engagement is desired, but this often creates drivability and NVH problems. In order to accurately predict the engine, clutch, and vehicle dynamics during the engine-start, detailed compression/firing torque and clutch models are developed. Using this model, the optimal control problem that minimizes the engine-start time while providing the torque demanded is solved by both analytical and numerical approaches. The DP control policy is found to be time-invariant, and thus can be directly implemented in the form of a full state feedback controller.

1.5 Outline of the Dissertation

This dissertation is organized as follows: In Chapter II, a system-level HEV/PHEV powertrain model was developed for accurate predictions of both fuel economy and tail-pipe emissions. In Chapter III, this model is used to solve an optimal supervisory control problem that minimizes both fuel consumption and emissions using DP, and a comprehensive extraction method is proposed to extract DP results and to develop a cold-start supervisory powertrain controller (SPC) that can change engine on/off, shift, and power-split strategies during a cold-

start. Chapter IV presents the new variable Energy-to-Distance Ratio (EDR), and an adaptive SPC algorithm that adjusts engine on/off and shift strategies based on EDR is developed. In Chapter V, a powertrain model of a parallel HEV is developed for control of the engine-start, and an optimal control problem of the engine-start is formulated and solved. Finally, conclusions are discussed in Chapter VI.

CHAPTER 2
MODELING OF THE HEV AND PLUG-IN HEV FOR FUEL ECONOMY AND EMISSIONS

In this chapter, a system-level HEV model is developed in the Matlab/Simulink environment. Many component models of the HEV model are shared with the Plug-in HEV (PHEV) model except for the motor and battery, of which the power and capacity increased. The purpose of the present HEV model is to develop an accurate but simple model appropriate for efficient evaluation of fuel economy and tail-pipe emissions.

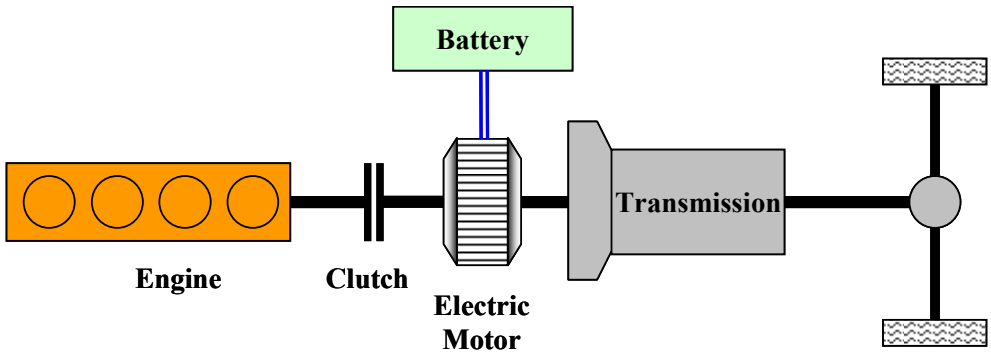

Figure 2.1: Schematic of a pre-transmission parallel HEV powertrain

2.1 System Configuration

The target vehicle is a compact SUV with the pre-transmission parallel hybrid configuration, also known as Input Power Assist (IPA) or P2. Figure 2.1 shows the schematic of the target vehicle. An engine-disconnect clutch replaces the torque converter for pure electric vehicle (EV) mode. The pre-transmission configuration allows a smaller M/G, easier packaging, and reduced spin losses over the post-transmission type [59]. Parameters of the vehicles are listed in Table 2.1.

Table 2.1: Parameters of the target vehicles; conventional, HEV, and Plug-in HEV

		Conventional vehicle	HEV	Plug-in HEV
Mass		1479kg	1579kg	1679kg
SI Engine		127kw (170hp) @5300rpm		
		217Nm (160lbft) @4500rpm		
Transmission		4 speed [2.95 1.62 1 0.68]		
Motor	**Rated power**	N/A	20kw	40kw
	Max torque		200Nm	400Nm
NiMH Battery	**Rated power**	N/A	20kw	40kw
	Capacity		1.3kwh	7.75kwh

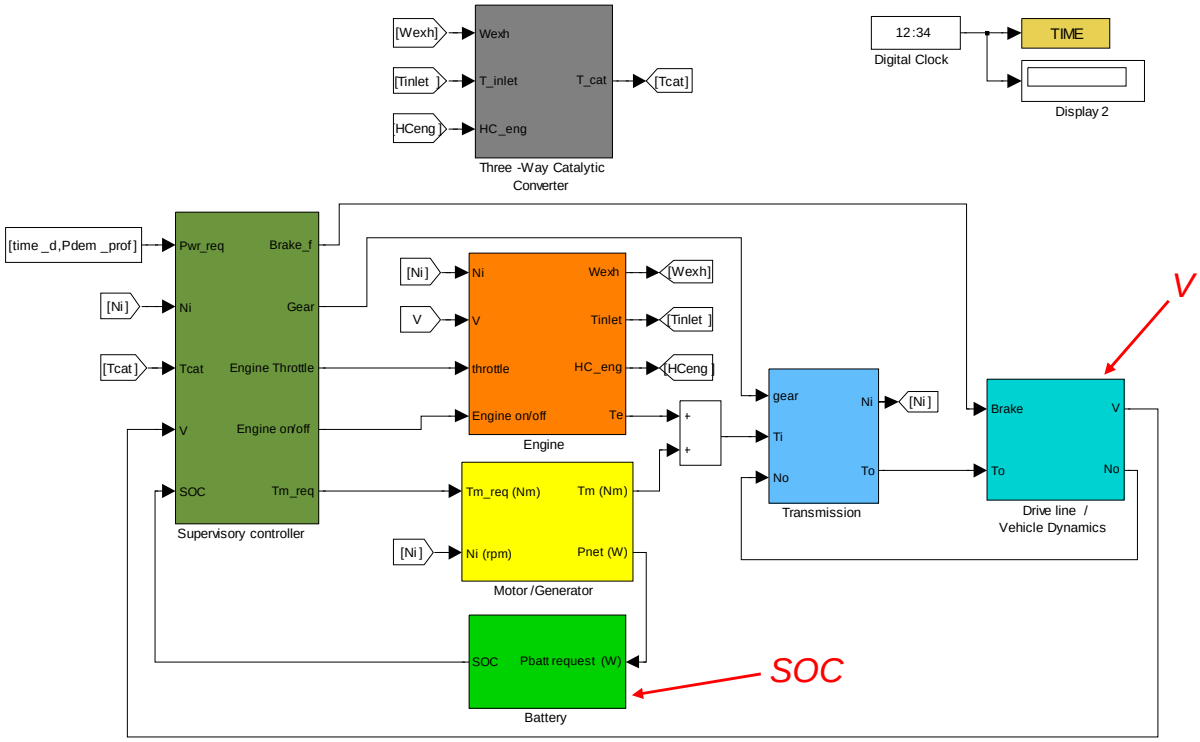

Figure 2.2: Overview of the Simulink HEV powertrain model

2.2 Fuel Economy Model

2.2.1 Overview of the fuel economy model

A simple two-state (vehicle speed and SOC) vehicle model is used to predict power and energy flows for the fuel economy evaluation. Other fast dynamics, such as intake manifold filling and motor dynamics, are assumed to be much faster than energy dynamics and neglected. Figure 2.2 shows the overview of the Simulink HEV powertrain model.

2.2.2 Sub-system models

2.2.2.1 Spark Ignition (SI) Engine

The quasi-static engine model is suitable for supervisory control studies assuming that the engine transients, e.g. intake manifold and combustion dynamics, are much faster than the system-level energy flow dynamics. This model is efficient and requires low computational load. All the engine outputs (e.g. torque, fuel consumption, and emissions) are described by static nonlinear maps with two inputs; throttle (φ) and engine speed (ω_e). The torque and fuel maps, shown in Figure 2.3 and Figure 2.4, are generated from the steady-state test bench provided by General Motors (GM).

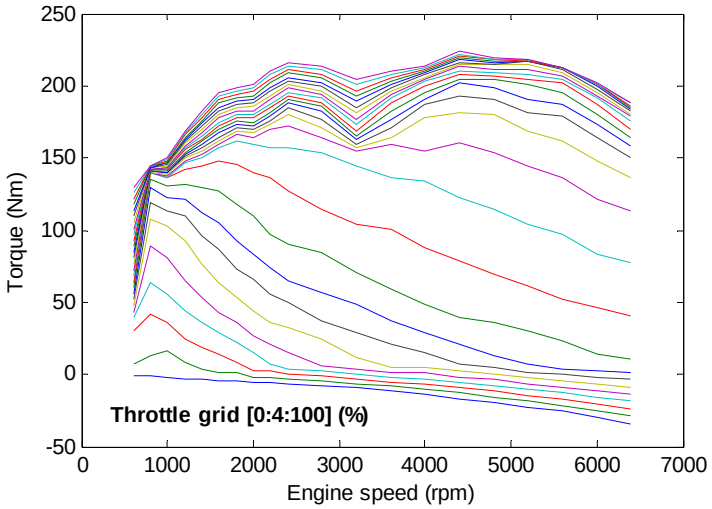

Figure 2.3: Engine torque map as a function of throttle and engine speed

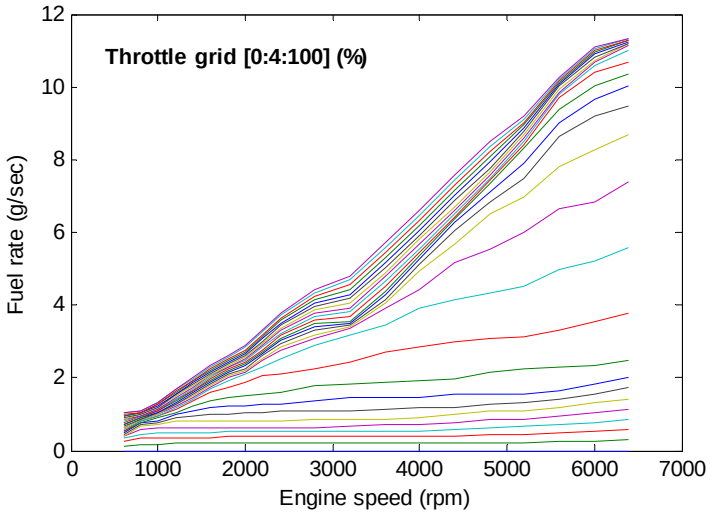

Figure 2.4: Engine fuel rate map as a function of throttle and engine speed

The accessory losses are not included in the engine torque map, but they are separately added for more accurate prediction of fuel economy as Equation (2.1) shows. The losses include power steering, fan, and brake pump losses, which are also modeled by look-up tables as functions of the throttle (φ) and engine speed (ω_e).

$$T_e = T_{eng}(\varphi, \omega_e) - T_{loss}(\varphi, \omega_e) \tag{2.1}$$

2.2.2.2 Motor/Generator (M/G)

The M/G subsystem includes a 20kW (40kW for PHEV) permanent magnet AC motor, an inverter, and an M/G controller. To reduce computational effort, it is assumed that the low-level controls, e.g. motor torque tracking, have sufficiently high bandwidth, and thus the effects of transients on energy flow dynamics are negligible. The requested M/G torque ($T_{M/G,req}$) signal from the supervisory controller and the angular M/G velocity ($\omega_{M/G}$), which equals the transmission input speed (ω_i), are the inputs to the M/G subsystem. The M/G model outputs the required electric power ($P_{M/G}$) and supplied M/G torque ($T_{M/G}$), which is assumed to perfectly track the requested torque ($T_{M/G,req}$) unless it is limited by the maximum M/G or battery power.

The following two equations mathematically describe the aforementioned relationships between the inputs and outputs of the M/G subsystem.

$$T_{M/G} = sign(T_{M/G,req}) \cdot \left| \min(T_{M/G,req}, T_{M/G,\max}, T_{batt,\max}) \right| \tag{2.2}$$

$$P_{M/G} = T_{M/G} \omega_{M/G} \eta_{M/G}^{\ k} \tag{2.3}$$

where $T_{M/G,max}$ is the maximum torque limited by M/G, $T_{batt,max}$ is the maximum torque limited by the battery, and $\eta_{M/G}$ is the M/G efficiency as a function of $T_{M/G}$ and $\omega_{M/G}$. The lumped efficiency map $\eta_{M/G}$, shown in Figure 2.5, accounts for all the energy lost during the energy conversion between mechanical and electrical domains for both directions including constant inverter efficiency of 95%. k indicates the direction of the power flow, and it is required for proper use of the efficiency map. If M/G is used as a motor, k = -1 and the motor provides propulsion power to the vehicle. When generating, k = 1 and the vehicle kinetic energy is converted to electrical energy and then stored in the battery.

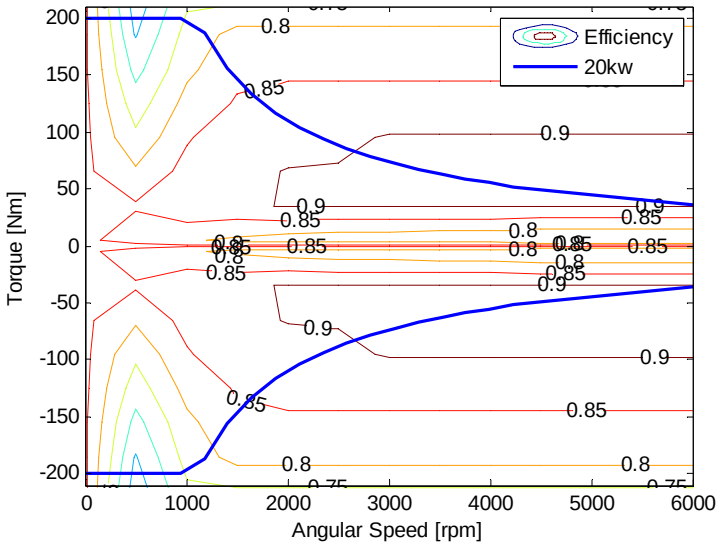

Figure 2.5: Efficiency contour map of the Motor/Generator (20kW)

2.2.2.3 Energy storage system (Battery)

A 20kW battery is selected for the target HEV (40kW for the PHEV), and the equivalent circuit battery model from ADVISOR package is adopted. The schematic diagram of the

equivalent circuit model is shown in Figure 2.6. The required M/G power ($P_{M/G}$) is the input, and SOC and the charge/discharge power limits ($P_{batt,max}$) are the outputs of the battery model.

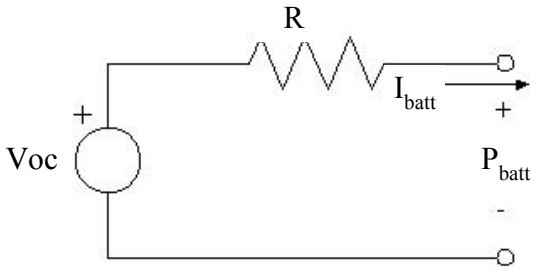

Figure 2.6: Internal resistive battery model

The model is divided into four sub-models where each sub-model computes open circuit voltage (V_{oc}) and internal resistance (R_{int}), power flow limit ($P_{batt,max}$), current (I_{batt}), and SOC sequentially. V_{oc} and R_{int} determine the battery efficiency and are functions of SOC and battery operating temperature (T_{batt}). We, however, assume isothermal operations in this study, and thus the open circuit voltage and internal resistance become functions of only SOC as Equation (2.4).

$$V_{oc} = f(SOC),\ R_{\text{int}} = f(SOC) \tag{2.4}$$

V_{oc} and R_{int} are then used to compute requested battery power, power limit, and the actual current flowing through the battery.

$$P_{batt} = f(P_{m/g}, SOC, V_{oc}, R_{\text{int}}) = V_{oc} I_{batt} - I_{batt}^2 R_{\text{int}} \tag{2.5}$$

Solving the quadratic Equation (2.5) for I_{batt}

$$I_{batt} = \frac{V_{oc} - \sqrt{V_{oc}^2 - 4(P_{batt} R_{\text{int}})}}{2R_{\text{int}}} \tag{2.6}$$

Knowing the amount of current flow, the SOC dynamics can be calculated as follows.

$$\dot{SOC} = -\frac{I_{batt}}{C_{batt}} \tag{2.7}$$

Note that the battery model contains only a single dynamic state, SOC. There are other battery models involving a larger number of dynamic states with more parameters for higher fidelity. However, it is commonly accepted that the single-state battery model sufficiently captures the key

dynamics and corresponding battery efficiency for supervisory control studies. Figure 2.7 shows the battery efficiency map as a function of SOC and P_{batt}, where the positive P_{batt} indicates battery discharge and the negative indicates charge. This contour map indicates that the battery efficiency is nearly constant with respect to the SOC.

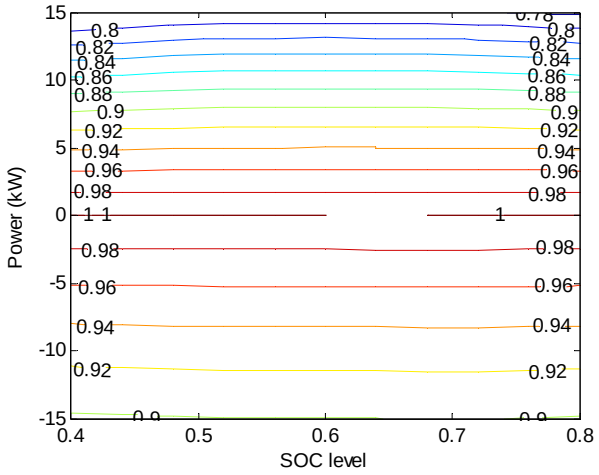

Figure 2.7: Efficiency contour map of the battery (20kW)

2.2.2.4 Drivetrain

The drivetrain is defined as the system from the transmission input shaft to the wheel. Although a drivetrain model can be quite complicated if the purpose of the model is for NVH analysis or servo level control, the model can be much simplified for the energy analysis purposes. Assuming perfect clutches and gear-shifts, the following equations describe the transmission and final drive gear models.

$$T_{wheel} = \eta_{GR}\eta_{FD} GR \cdot FD \cdot T_i - C_{TM}\omega_i \tag{2.8}$$

$$\omega_i = GR \cdot FD \cdot \omega_{wheel} \tag{2.9}$$

where GR is transmission gear ratio; FD is final drive gear ratio; η_{GR} and η_{FD} are transmission and final drive efficiency, respectively; T_i is transmission input torque, C_{TM} is transmission viscous-loss coefficient; ω_i is transmission input speed; and ω_{wheel} is wheel speed.

2.2.2.5 Vehicle dynamics

For fuel economy and emission performance evaluations, it is a common practice that only the vehicle longitudinal dynamics is considered. The longitudinal vehicle dynamics is modeled as a single point mass with various forces acting on it. The vehicle speed and road load are computed by Equation (2.10)-(2.11).

$$\dot{V} = \frac{T_{wheel} R_{tire} - F_{brake} - F_{road}}{M_r} \tag{2.10}$$

$$F_{road} = f_0 + f_1 V + f_2 V^2 \tag{2.11}$$

where R_{tire} is the tire radius, F_{brake} is the friction brake force, and F_{road} is the road load. The road load includes road grade (f_0), rolling (f_1), and aerodynamic (f_2) resistances. Note that the tire dynamics (e.g. tire slip) is not included in this model, and it is assumed that all torque is transmitted to the vehicle.

2.2.2.6 Regenerative braking

The regenerative braking algorithm plays an important role in evaluating HEV performance because it determines how much vehicle kinetic energy is recuperated for future use, and thus, affects the overall vehicle efficiency. Figure 2.8 shows two types of regenerative braking algorithms: parallel and series [59].

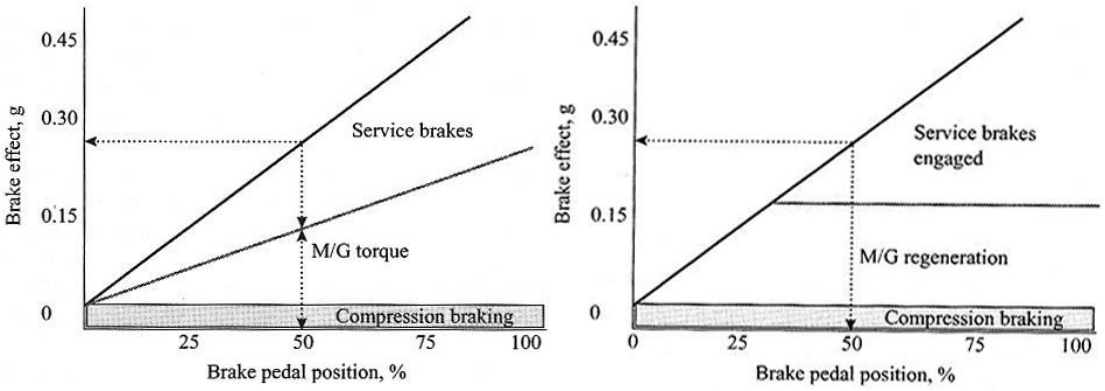

(a) Parallel type (b) Series type

Figure 2.8: Parallel and series regenerative braking algorithms [59]

Although the parallel type does not require a sophisticated braking torque proportioning controller, it does not recuperate the maximum possible kinetic energy. Thus, the series type will be used in this study, assuming that the braking torque proportioning algorithm works properly and all vehicle kinetic energy is regenerated as long as the braking power is lower than the M/G and battery power limits. The friction brake is applied only when the requested brake level cannot be met by the regenerative braking. Equation (2.12) shows the regenerative braking algorithm.

$$T_{M/G,req} = W_{SOC} W_V \min\left(T_{i,dem}, T_{M/G,\max}, T_{batt,\max}\right) \tag{2.12}$$

where $W_{SOC} = f(SOC)$ and $W_V = f(V)$. Weighting functions W_{SOC} and W_V are used to avoid overcharge and NVH issue at low vehicle speed, since overcharge may damage the battery and the M/G control at low vehicle speed may cause passenger discomfort [103]. Figure 2.9 shows these two weighting factors.

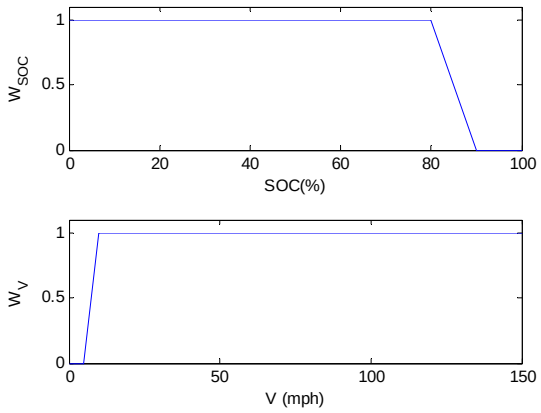

Figure 2.9: Regenerative braking weighting factors

2.3 Emission Model

Balancing model fidelity and computational efficiency is a key factor to be considered for a successful emission model. In particular, the number of states must be kept small for Dynamic Programming implementation. In this section, a simplified emission model suitable for supervisory control of HEVs is developed, and integrated with the fuel economy model developed in Section 2.2.

2.3.1 Emission fundamentals

Key chemical reactions that determine the amount of noxious emissions in the exhaust gases can be described by a two-step process: (1) emission production during combustion and (2) emission reduction via the after-treatment system. In the cylinders, fuel and air chemically react to produce power and exhaust gases with harmful emissions, which travel through the exhaust manifold and then into the Three-Way Catalytic Converter (TWC), where a part of the harmful emissions are converted into safe gases. The following subsections summarize the essentials of these two processes.

2.3.1.1 Emission production during combustion

The chemical reaction and emission production during combustion in a gasoline engine is significantly influenced by the engine temperature as well as air/fuel ratio, engine speed, manifold pressure, air temperature, intake/exhaust valve timing, and spark timing. The production mechanism of three noxious emissions (hydrocarbon, carbon dioxide, and nitrogen oxide) and the influence of the engine temperature on the emission production are of particular importance to this study.

***Hydrocarbon* (*HC*) –** The crevice and cylinder head are the main areas that produce HC when fully warmed-up. During a cold-start, HC is the most challenging emission to be reduced because the amounts of unburned and partially burned fuel greatly increase due to poor combustion quality when engines are cold. A cold engine with cold cylinder walls tends to produce more HC due to multiple factors including the following five major causes [32].

1. Misfiring
2. Incomplete flame propagation
3. Wall wetting
4. Rich fuel-air charge
5. Crevice storage of the fuel-air charge and its release

Figure 2.10 shows the steady-state HC production rate as a function of throttle and engine speed, when the engine is fully warmed up. Note that the HC map is very similar to the fuel rate map.

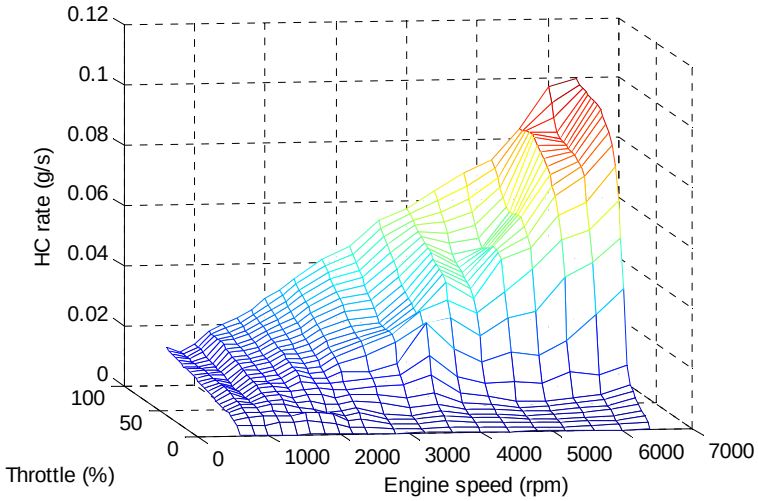

Figure 2.10: Engine-out HC rate map of a fully warmed-up engine.

***Carbon Monoxide* (*CO*) –** The amount of CO production is primarily influenced by the air-fuel (A/F) ratio where low A/F ratio generally increases CO production [78]. Many conventional vehicles are equipped with a fuel rich (low A/F ratio) strategy for faster catalyst warm-up during cold-start because fuel rich combustion results in higher exhaust gas temperature. Thus, two design objectives, lower fuel consumption and lower CO, conflict each other and a control strategy during cold-start must be carefully designed to minimize total CO over the driving cycles. Figure 2.11 illustrates that the CO rate increases very rapidly above 4000 rpm.

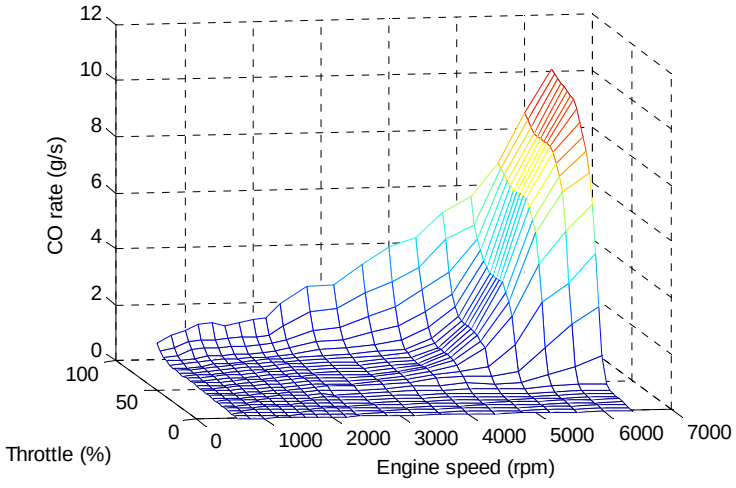

Figure 2.11: Engine-out CO rate map of a fully warmed-up engine.

***Nitrogen Oxide* (NO_x) –** Dissociation, the main NO_x producing reaction, decreases with lower engine temperature, because a cold engine lowers the flame temperature and hinders the flame propagation [17]. Thus, NO_x reduction during cold-start is a lesser concern. Figure 2.12 shows the NO_x rate map for a fully warmed-up engine.

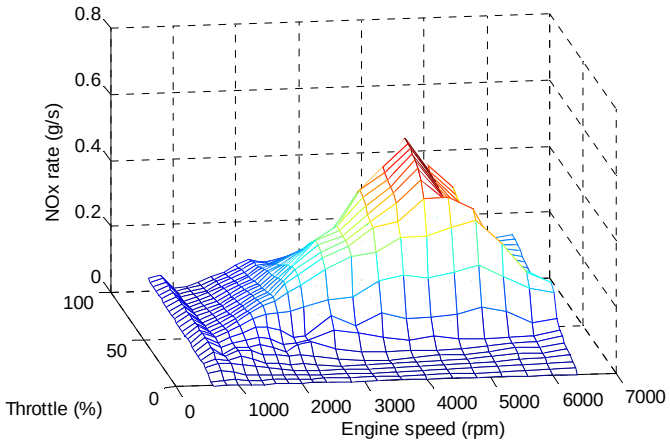

Figure 2.12: Engine-out NO_x rate map of a fully warmed-up engine.

2.3.1.2 Emission reduction via after-treatment system

Since the early 1980's the TWC has been rapidly developed and widely used to reduce noxious exhaust gases (HC, CO, and NO_x). In the TWC, the engine-out exhaust gases undergo five major chemical reactions listed below [17].

$$CO + 0.5O_2 \rightarrow CO_2 \tag{2.13}$$

$$C_3H_6 + 4.5O_2 \rightarrow 3CO_2 + 3H_2O \tag{2.14}$$

$$CH_4 + 2O_2 \rightarrow CO_2 + 2H_2O \tag{2.15}$$

$$H_2 + 0.5O_2 \rightarrow H_2O \tag{2.16}$$

$$CO + NO \rightarrow CO_2 + 0.5N_2 \tag{2.17}$$

Note that these chemical reactions are activated only after the catalyst reaches its light-off temperature and it take significant time for the catalyst to warm up. As a result, an automobile typically produces 70~90% of its emissions before the catalyst warms-up [17,78]. Therefore, fast catalyst warm-up is important during a cold-start.

2.3.2 Modeling for supervisory control approach

For conventional vehicles, the control problem of emission minimization has focused on A/F ratio and spark timing control for fast catalyst warm-up during cold-start idle operations. When positive power is demanded by a driver, the engine must provide the requested power. In contrast, HEVs have an additional control degree of freedom, and the power demand can be split between two power sources: battery and engine. Different power-split strategies lead to different engine operations, thermodynamic responses of the catalyst, and thus different tail-pipe emission responses. Therefore, the present model development will focus on the dynamic effects of various engine operations (or power-split strategies) on the TWC dynamics and total tail-pipe emissions. In addition, all low-level controllers (e.g. A/F control and spark timing during a cold-start) are assumed to be previously designed and perfectly controlled in this study.

2.3.3 Overview of the tail-pipe emission model

Figure 2.13 shows the overview of the emission model. The emission model can be divided into two sub-models; engine thermal dynamics and after-treatment dynamics. Since quasi-static engine model only outputs steady-state (hot) engine data, the role of engine thermal dynamics is to take the engine temperature into account for accurate prediction of cold engine outputs. The after-treatment system dynamics includes catalyst brick temperature dynamics, which is required for computing conversion efficiency of the TWC.

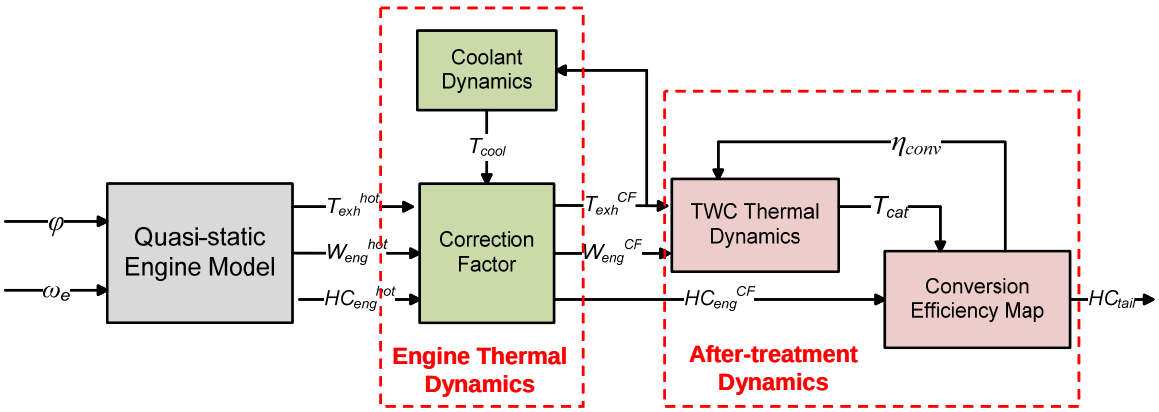

Figure 2.13: Block diagram of the tail-pipe emission model

2.3.4 Sub-system models

2.3.4.1 Engine thermal dynamics

The engine thermal dynamics and its effects on engine-out emissions are important to accurately predict engine-out emissions during cold-start. The engine thermal dynamics is further divided into two sub-blocks, coolant temperature dynamics and correction factor.

Coolant temperature dynamics

Although the cylinder wall temperature is the key variable that affects the combustion kinetics, the coolant temperature is frequently selected to represent the cylinder wall temperature because of 1) rapid response to the cylinder wall temperature, 2) ease of measurement, and 3) ease of modeling [62].

Under the assumption that the cooling system controller activates circulation of the coolant when the coolant temperature reaches a threshold value $T_{cool,max}$, a simple lumped thermal capacitor model with saturation is:

$$\frac{dT_{cool}}{dt} = \frac{1}{\tau_{gain}}\left(T_{exh}^{CF} - T_{cool}\right) + \frac{1}{\tau_{loss}}\left(T_{atm} - T_{cool}\right) \text{ where } T_{cool} \le T_{cool,\max} \tag{2.18}$$

where T_{cool} is coolant temperature, T_{atm} is atmospheric temperature, and τ_{gain} and τ_{loss} are heat transfer time constants. T_{exh}^{CF} indicates the corrected (cold) exhaust gas temperature. Although combustion flame temperature would be more appropriate for heat-gain source temperature, T_{exh} is used instead due to its accessibility. The following section describes how a correction factor is computed.

Cold-engine correction factor

For supervisory control purposes, we seek a simplified model that predicts cold engine outputs as a function of coolant temperature. One approach is to simply multiply hot engine outputs by a Correction Factor (*CF*), which is essentially a cold/hot ratio as a function of the coolant temperature. Murrell *et al*. collected experimental cold-start data from various engines

and showed a clear correlation between *CF* and coolant temperature [62]. It was observed that *CF* can be approximated by an exponential function:

$$CF_j = 1 \pm \exp(-(T_{cool} - T_{0,j}) / K_{CF,j}) \tag{2.19}$$

where $T_{0,j}$ and $K_{CF,j}$ are curve-fitting parameters for each engine output j. Figure 2.14 shows *CF* of emission components, fuel consumption rate, torque, and exhaust temperature, as a function of coolant temperature. Note that the appropriate sign must be selected in Equation (2.19) for each engine output. The cold engine outputs can be computed by multiplying hot engine outputs by *CF* as in Equation (2.20).

$$j^{CF} = CF_j \cdot j \tag{2.20}$$

where j represents engine outputs such as HC, CO, NO_x, T_{inlet}, T_e (engine torque), and $\dot{m}_f$ (fuel consumption rate). The parameters of the correction factor functions will be estimated and listed in Section 2.4.

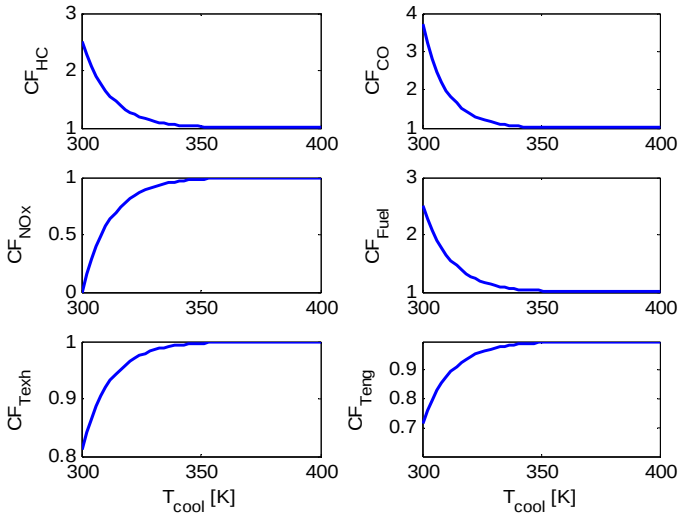

Figure 2.14: Correction factors (cold/hot ratio) of various engine outputs as a function of the coolant temperature

2.3.4.2 After-treatment dynamics

The after-treatment system model (Figure 2.15) is divided into two parts; the TWC thermal dynamics and the conversion efficiency map. The TWC thermal dynamics calculates the catalyst

brick temperature. Then, conversion efficiencies are calculated based on the catalyst brick temperature.

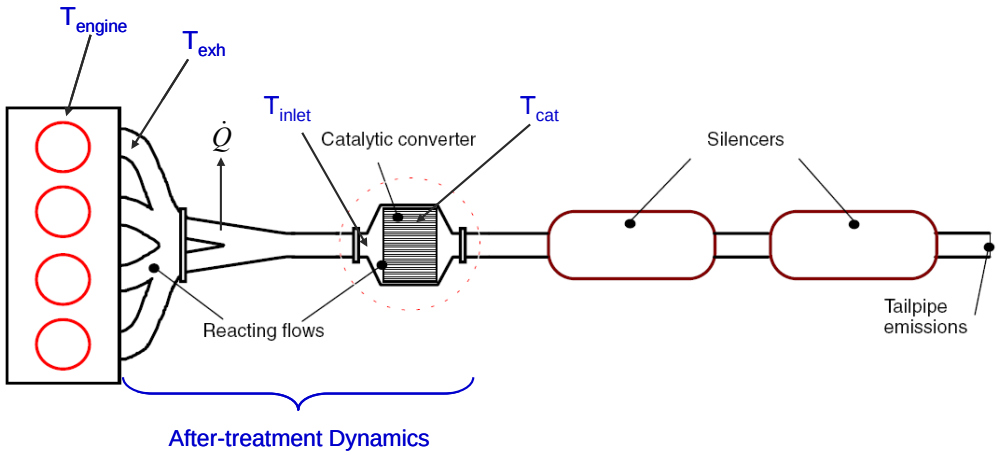

Figure 2.15: Schematic of the after-treatment system [66]

TWC thermal dynamics

Let us first define exhaust gas temperatures at two locations in the after-treatment system as shown in Figure 2.15. T_{exh} and T_{inlet} are the exhaust gas temperatures at the exhaust manifold and TWC inlet, respectively. T_{inlet} is available from the steady-state engine data and is plotted in Figure 2.16.

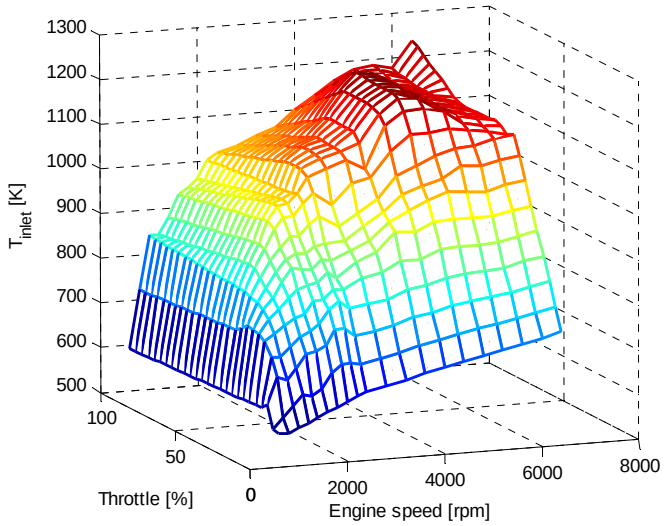

Figure 2.16: Test-based exhaust gas temperature map at the catalytic converter inlet

If the exhaust gas temperature is not available, the gas inlet temperature can be empirically estimated based on published data. Eriksson collected steady-state exhaust gas temperature data at several locations from an experiment for exhaust system modeling, and concluded that there is a clear relationship between the exhaust gas flow rate and exhaust gas temperatures [24]. In particular, the exhaust gas temperature at the converter inlet can be approximated by a logarithmic function of the exhaust flow rate (2.21) as Figure 2.17 shows, whereas the gas temperature at the manifold near the exhaust port can be approximated by a linear function.

$$T_{inlet} = T_{0,exh} + K_{inlet} \ln(W_{eng}) \tag{2.21}$$

The logarithmic function and large temperature drop at the low gas flow rate can be explained by the heat transfer over the exhaust pipe. In other words, the temperature drop decreases with increasing gas flow rate. Also, the cycle-to-cycle variation and varying engine operating conditions are responsible for the scattered data of T_{exh}, since the thermocouple is located very close to the cylinder [24].

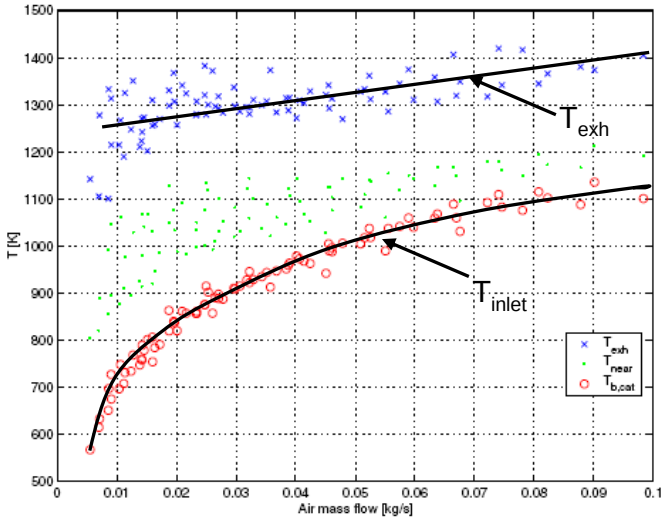

Figure 2.17: Exhaust gas temperatures as a function of the gas flow rate [24]

Given the inlet gas temperature, the brick temperature dynamics are modeled by a lumped thermal capacitor as shown in Figure 2.18.

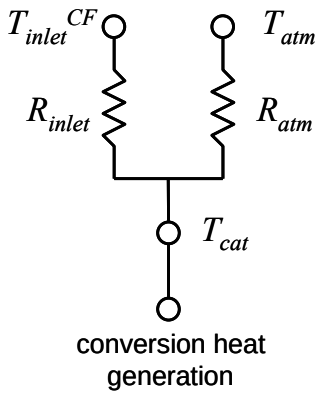

Figure 2.18: Thermal resistance diagram of the after-treatment system

The governing equation for the lumped capacitor model is described as follows.

$$\rho Vc\frac{dT_{cat}}{dt} = h_{cat}(W_{eng})A_{s,i}\left(T_{inlet}^{CF} - T_{cat}\right) + h_{atm}A_{s,o}\left(T_{atm} - T_{cat}\right) + \sum_i K_{c,i}\eta_{conv,i}W_{eng,i} \tag{2.22}$$

where T_{cat} is the catalyst brick temperature. The first term on the right side is heat gain from the exhaust gas, the second term is heat loss to the atmosphere, and the last term is the heat generated from emission conversion. Note that the heat transfer coefficient (h_{cat}) is significantly influenced by the gas flow rate, W_{eng}. Assuming that the heat transfer coefficient is a linear function of W_{eng}, Equation (2.23) can then be expressed as following:

$$C_t\frac{dT_{cat}}{dt} = \frac{W_{eng}}{R_{inlet}}\left(T_{inlet}^{CF} - T_{cat}\right) + \frac{1}{R_{atm}}\left(T_{atm} - T_{cat}\right) + \sum_i K_{c,i}\eta_{conv,i}W_{eng,i} \tag{2.23}$$

$$\frac{dT_{cat}}{dt} = \frac{W_{eng}}{\tau_{inlet}}\left(T_{inlet}^{CF} - T_{cat}\right) + \frac{1}{\tau_{atm}}\left(T_{atm} - T_{cat}\right) + \sum_i K_{conv,i}\eta_{conv,i}W_{eng,i} \tag{2.24}$$

where C_t is the lumped thermal capacitance of the catalyst brick; R_{inlet} and R_{atm} are the thermal resistance with respect to exhaust gas temperature at the inlet and atmosphere, respectively; $K_{conv,i}$ is a conversion energy generation constant for each reacting emission; $\eta_{conv,i}$ is conversion efficiency of each emission; $W_{eng,i}$ is flow rate of each emission; and i represents each type of emission.

Conversion efficiency map

With the catalytic converter brick temperature computed above, we can use this information to predict the emission conversion efficiency [17,38,51,86], which is defined as:

$$\eta_{conv,i} \equiv 1 - \frac{W_{tail,i}}{W_{eng,i}} \tag{2.25}$$

where $W_{tail,i}$ is tail-pipe flow rate of emission i. Both exponential and *arctan* functions are commonly used to describe the relationship between the brick temperature and conversion efficiency. Among these two candidate functions, *arctan* is selected due to its ease of parameter tuning:

$$\eta_{conv,i} = \left(0.5 + 0.4 \cdot \arctan\left(\frac{T_{cat} - T_{lightoff,i}}{K_{eff,i}} \right) \right) \cdot \xi_{exh,i} \tag{2.26}$$

where $\xi_{exh,i}$ is a weighting factor for the exhaust gas flow rate, $K_{eff,i}$ is a tuning parameter that represent a slope of the efficiency function, and $T_{lightoff,i}$ is the light-off temperature of each type of emissions. Note that $\eta_{conv,i}$ is saturated by a minimum and a maximum conversion efficiencies (e.g. 0 and 0.99). Figure 2.19 illustrates a conversion efficiency map and what each parameter represents.

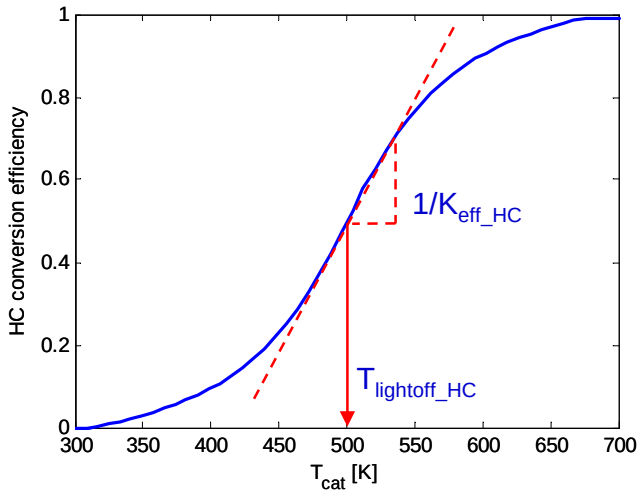

Figure 2.19: Conversion efficiency map of HC using an *arctan* function.

Finally, the efficiency of the catalytic converter should be a function of exhaust gas flow rate, which could be approximated by a linear function as shown below [75].

$$\xi_{exh,i} = a_i \cdot W_{eng} + b_i \tag{2.27}$$

The exhaust gas flow rate weighting factor becomes significant when tuning tail-pipe CO response in the subsequent section.

2.4 Parameter Estimation and Model Validation

Model validation for fuel economy has been extensively conducted in the literature, and we focus on parameter estimation and model validation of the emission model in this section. Parameters of the emission model are calibrated by comparing the model's response with the test data. Note that only limited cold-start test data are available to the author due to the difficulty of experiment set-ups for the transient engine performance, and thus, complete model validation over the entire state space is not performed. Instead, a set of cold-start FTP cycle data for the target vehicle is used for parameter estimation and model validation.

The parameter estimation is done in a two-step process. The availability of engine-out emission data allows for a decoupled parameter tuning of the engine and catalytic converter models. First, using engine-out emissions and engine-load test data as inputs to the model, the parameters of the converter model are tuned to match the tail-pipe emission responses of the model to those of the cold-start FTP cycle data. Figure 2.20 shows that the TWC model very accurately predicts three tail-pipe emissions during a cold-start despite some discrepancy in conversion efficiencies. In theory, if both engine-out and tail-pipe emissions of the model and data match, conversion efficiencies must match as well. It is possible that the definition of the conversion efficiency is different or there are computational errors. If converter temperature data are available, tuning parameters of the catalytic converter model can further be divided into two separate steps (catalyst brick temperature and conversion efficiency map).

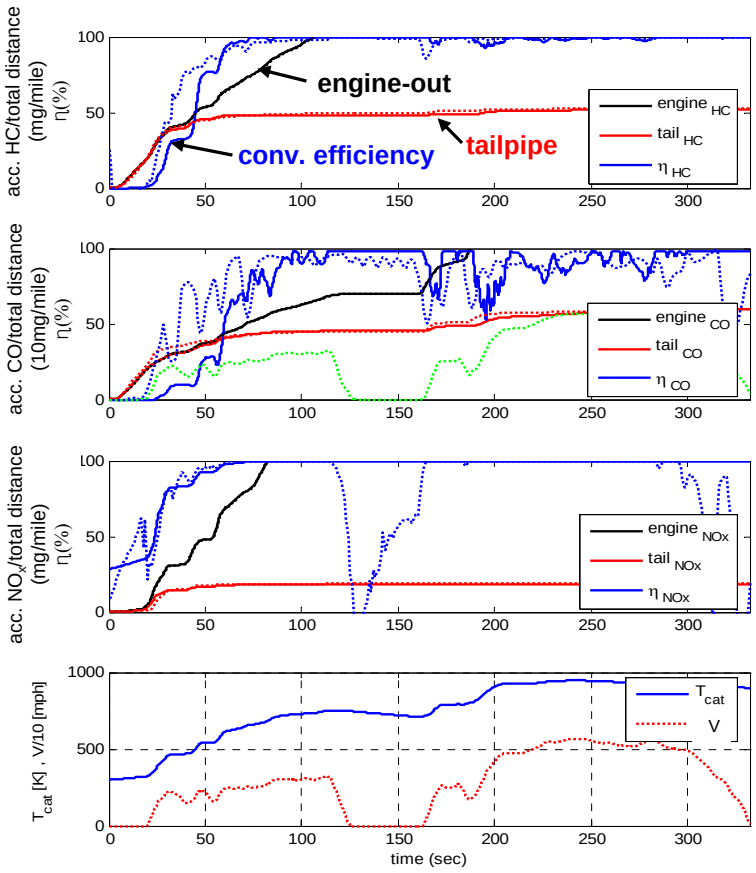

Figure 2.20: Comparison of TWC model (solid) vs. test data (dashed) emission responses for the cold-start FTP urban cycle

After the catalytic converter model is tuned properly, parameters of the cold engine model are then tuned to generate both engine-out and tail-pipe emission responses that match with those of the cold-start FTP cycle data. Table 2.2 shows the list of parameters that are obtained from the tuning process. Overall, Figure 2.21 shows a good match of the emission model (solid lines) to the test data (dashed lines). Predictions of tail-pipe HC show a great match with those of test data, while NO_x and CO predictions are not as good. These errors mainly come from an engine-out emissions mismatch due to the interpolation error of the engine-out emission map, and this error can be reduced by collecting more engine data in those operating regions. In the next two chapters, this HEV model will be extensively used to optimize both fuel economy and tail-pipe emissions.

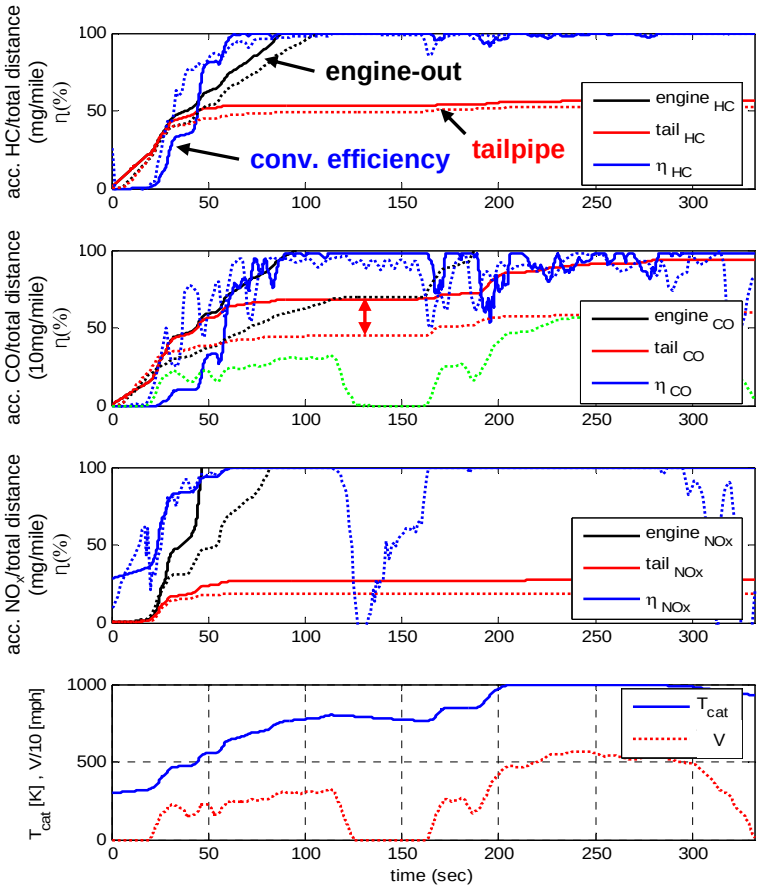

Figure 2.21: Comparison of complete model (solid) vs. test data (dashed) emission responses for cold-start FTP urban cycle

Table 2.2: Emission model parameters determined from model tuning and validation

Parameter	Value	Parameter	Value	Parameter	Value
$T_{lightoff,HC}$	500 K	$K_{eff,HC}$	20π	$K_{conv,HC}$	20
$T_{lightoff,CO}$	600 K	$K_{eff,CO}$	25π	$K_{conv,CO}$	20
$T_{lightoff,NOx}$	360 K	$K_{eff,NOx}$	32π	$K_{conv,NOx}$	20
a_{HC}	-0.002	b_{HC}	1.04	τ_{inlet}	1000
a_{CO}	-0.011	b_{CO}	1.17	τ_{atm}	600
a_{NOx}	0	b_{NOx}	0	τ_{gain}	500
				τ_{loss}	400

CHAPTER 3
OPTIMAL CONTROL OF THE HEV FOR FUEL ECONOMY AND EMISSIONS

In this chapter, a systematic design method of a cold-start supervisory powertrain controller (SPC) was developed based on the Dynamic Programming (DP) technique. Despite guaranteed global optimality, DP cannot be directly implemented in a real-time controller because the optimal control policy computed by DP is time-dependent on a specified speed profile. Thus, more useful control strategies are extracted from the DP solution, and a cold-start SPC algorithm is designed based on the extracted results.

3.1 Optimal Control via Dynamic Programming

Dynamic Programming (DP) is a powerful tool for solving dynamic optimization, also known as trajectory optimization, problems due to its guaranteed global optimality even for nonlinear dynamic systems with constraints. Although the near-optimality of the static optimization technique was validated for the fuel economy control problem of a parallel HEV (discussed in the Appendix), the near-optimality does not hold when emissions are considered because tail-pipe emissions heavily depend on the catalyst temperature. Thus, DP, a dynamic optimization technique, will be used to obtain the globally optimal solution of this multiple objective optimal control problem. Knowing that faster catalyst warm-up generally trades off with fuel economy and that there is an additional control degree of freedom (power-split), it is interesting to see if DP will be able to reduce tail-pipe emissions without significant loss of fuel economy.

3.1.1 DP problem formulation

Inclusion of emission dynamics in the vehicle model introduces two additional dynamic states (T_{cat}, T_{cool}), in addition to the original dynamic state, SOC. Note that the vehicle speed is specified by the driving cycle and is no longer a state variable. The well-known *curse of dimensionality* makes it exponentially difficult to solve DP problems with increasing number of states and/or control inputs [4,6,41]. Therefore, a simplified model is preferred, and further simplification of the model is necessary for reduced computational load. Since tailpipe emissions are dominated by the catalyst temperature dynamics and its conversion efficiency, we decided to simplify the coolant temperature model based on the assumption that the warm-up and cool-down rates of the coolant temperature during a cold-start are proportional to those of the converter brick temperature. Verification of the above assumption can be found from the literature [62], and the coolant temperature is approximated by a linear function of the catalyst temperature until it reaches the coolant circulation threshold temperature, $T_{cool,max}$.

$$T_{cool} = \begin{cases} T_{atm} + K_{T\_ratio}(T_{cat} - T_{atm}) & ,\text{if } T_{cool} < T_{cool,\max} \\ T_{cool,\max} & ,\text{if } T_{cool} \geq T_{cool,\max} \end{cases} \tag{3.1}$$

Replacing the original coolant temperature dynamics (Equation (2.19)) with Equation (3.1) reduces the number of dynamic states down to two, which results in a DP problem with manageable computation load. Table 3.1 summarizes the key variables of the DP problem, which consists of a discrete and a continuous control input and two dynamic states, whereas vehicle velocity (V) and power demand (P_{dem}) are specified by the FTP-72 driving cycle.

Note that the engine-off command is included in this DP problem by augmenting T_{eng} grid with a node with a value equal to -1. Also, a control variable, motor torque ($T_{m/g}$), is eliminated by the drivability constraint defined as

$$T_{M/G} = T_{i,dem} - T_{eng} \tag{3.2}$$

where T_{dem} is torque demand at the transmission input. Table 3.1 also indicates that the gear position is a control input, which allows the DP to have full control over the powertrain.

Table 3.1: Variables and grids of the HEV DP problem for fuel economy and emissions

	Variables	Grid
Stage (k)	Time	[0:1:final time]
Control (u)	Gear (Gr)	[1 2 3 4]
	Engine torque (T_e)	[-1 0:5:210]
State (x)	SOC	[0.5:0.01:0.7]
	Catalyst temperature (T_{cat})	[300:40:700 900]

Let us define a cost function and identify constraints of the multi-objective optimal control problem. The objective of the optimal supervisory control is to minimize fuel economy and tail-pipe emissions, while sustaining SOC level at the end of a cycle. Although three types of major harmful emissions (HC, CO, and NO_x) were modeled for a wide range of applications, the emission regulations put emphasis on reducing cold-start HC for gasoline engines (see section 1.1.2). Thus, only HC is penalized in the cost function to focus on the trade-off between HC and fuel economy and the design method of a cold-start SPC in this study.

$$\text{Minimize } J = \sum_{k=0}^{N-1} \left(FC_k + \beta HC_k \right) \tag{3.3}$$

$$\text{Subject to } SOC_{final} = SOC_{initial} \tag{3.4}$$

Although equations (3.3) and (3.4) reflect a well-defined optimal control problem, the final SOC constraint in (3.4) is numerically difficult to implement because large costs are often applied to constrained states, and these costs tend to propagate throughout the entire state space due to the interpolation method used to compute previous state costs (J_{k-1}). Unfortunately, use of the interpolation cannot be avoided because this is a two-dimensional DP problem, for which the exact DP algorithm (no interpolation) is difficult to implement. Therefore, an alternative optimal control problem that can be numerically implemented is defined as follows with component limits.

$$\text{Minimize } J = \sum_{k=0}^{N-1} \left(\alpha \Delta SOC_k + FC_k + \beta HC_k + \gamma \Delta Gr + \lambda \Delta E_{on/off} \right) \tag{3.5}$$

$$\text{Subject to} \quad \begin{aligned} & SOC_{final} = SOC_{initial} \\ & \omega_{e,\min} \le \omega_{e,k} \le \omega_{e,\max} \\ & T_{e,\min} \le T_{e,k} \le T_{e,\max} \\ & T_{M/G,\min} \le T_{M/G,k} \le T_{M/G,\max} \\ & P_{bat,\min} \le P_{batt,k} \le P_{batt,\max} \end{aligned} \tag{3.6}$$

where ω_e is engine speed, T_e is the engine torque, $T_{m/g}$ is the motor torque, and P_{batt} is the battery power. Note that the ΔSOC penalty is added in the cost function to implement the charge sustenance, and α needs to be adjusted for a charge sustaining strategy. In addition, penalties on engine on/off and gear-shift events are added to avoid an excessive number of these events. Readers are referred to the Appendix for the detailed DP algorithm.

3.1.2 DP results

The trade-off between fuel economy and *HC* is studied by varying coefficient β in Equation (3.5). Table 3.2 indicates that a trade-off exists between fuel economy and tailpipe *HC*, and a substantial tailpipe *HC* reduction can be achieved by a slight fuel economy loss, through a significantly shortened light-off time.

Table 3.2: DP results showing trade-off between fuel economy and *HC*

	$\beta = 0$	**$\beta = 20$**	**$\beta = 50$**	**$\beta = 200$**	**$\beta = 500$**
Penalty Coefficients	$\alpha = 413$ $\gamma = 0.02$ $\lambda = 0.05$	$\alpha = 417$ $\gamma = 0.02$ $\lambda = 0.05$	$\alpha = 419$ $\gamma = 0.02$ $\lambda = 0.05$	$\alpha = 432$ $\gamma = 0.02$ $\lambda = 0.05$	$\alpha = 451$ $\gamma = 0.02$ $\lambda = 0.05$
MPG [adjusted, coldstart]	40.26 (0%)	40.11 (-0.4%)	39.90 (-0.9%)	39.66 (-1.5%)	39.30 (-2.4%)
HC (mg/mile)	43.7 (0%)	37.7 (-13.7%)	28.7 (-34.3%)	25.2 (-42.3%)	22.9 (-47.6%)
Light-off time (sec)	45	43	28	28	28

Pareto-curve that represents this trade-off is shown in Figure 3.1. DP results show that ULEV standard can be met by penalizing HC, but the target vehicle would need comprehensive HC reduction techniques, e.g. HC adsorber or air-injection, to meet the SULEV standard (10 mg/mile).

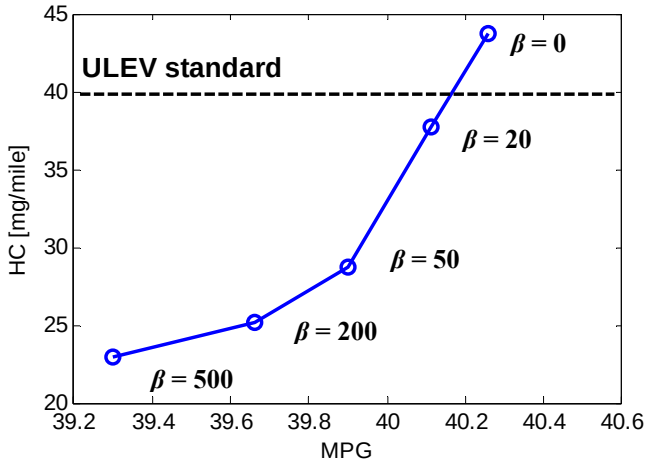

Figure 3.1: Trade-off between fuel economy and HC over various β.

Figure 3.2 compares two DP solutions; $\beta = 0$ and $\beta = 200$. This comparison shows that tail-pipe HC emissions are reduced by commanding extra load from the engine early on in the drive cycle, so that the TWC rapidly warms up during the first vehicle launch. Although this initially leads to increased fuel consumption, the extra power is stored in the battery, and the increased fuel consumption is later offset by spending the additional energy stored in the battery. Therefore, significant emission reduction can be achieved with minimal loss of fuel economy.

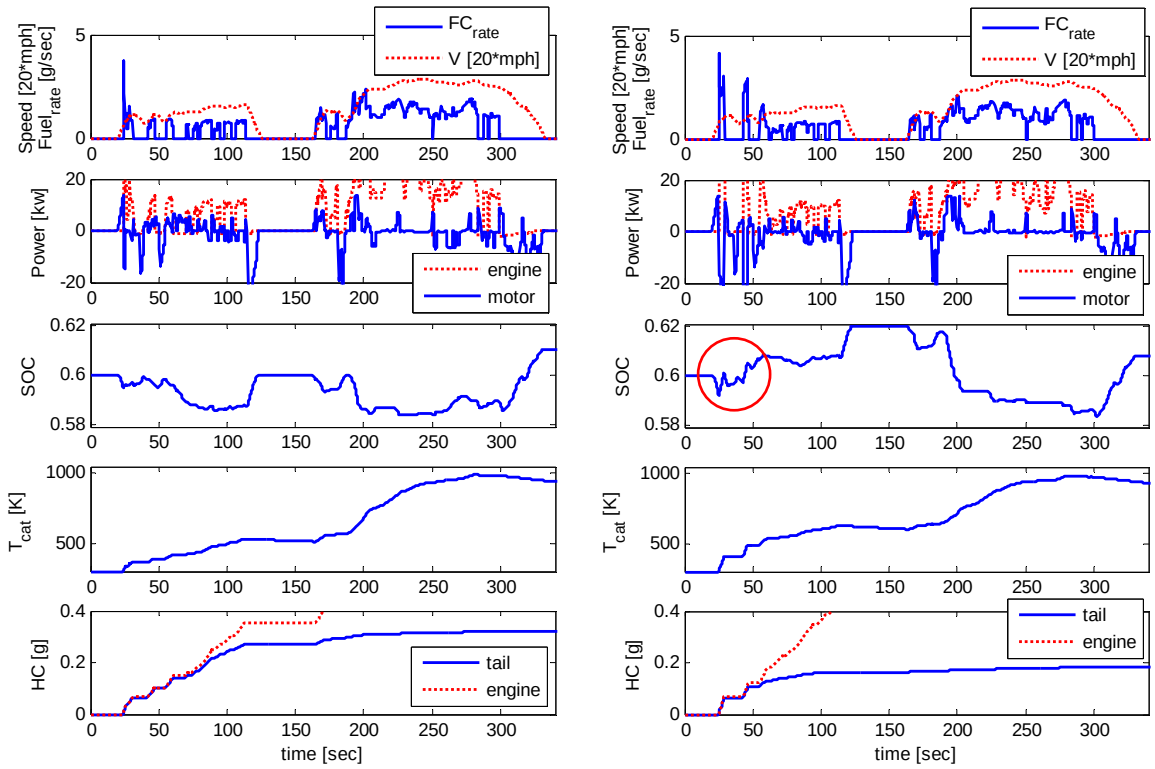

(a) $\beta = 0$ (b) $\beta = 200$

Figure 3.2: Simulation results of the DP solution for $\beta = 0$ and $\beta = 200$ on the FTP urban cycle

3.2 Comprehensive Extraction Method

Despite guaranteed optimality of the DP solution, its solution cannot be directly implemented because the output of the DP algorithm is a time-varying control sequence. The time dependence of this control sequence is strong because the vehicle speed and driver power demand is fixed at time step k, and extraction of an implementable feedback controller is necessary. The conventional extraction method previously developed at the University of Michigan extracted near-optimal gear-shift and power-split strategies from a single optimal trajectory [53]. This method, when applied to cold-start optimization results, does not provide enough information to extract cold-start control strategy due to the short warm-up time. Thus, a comprehensive extraction method is proposed to learn and extract cold-start optimal control strategies over the entire state space.

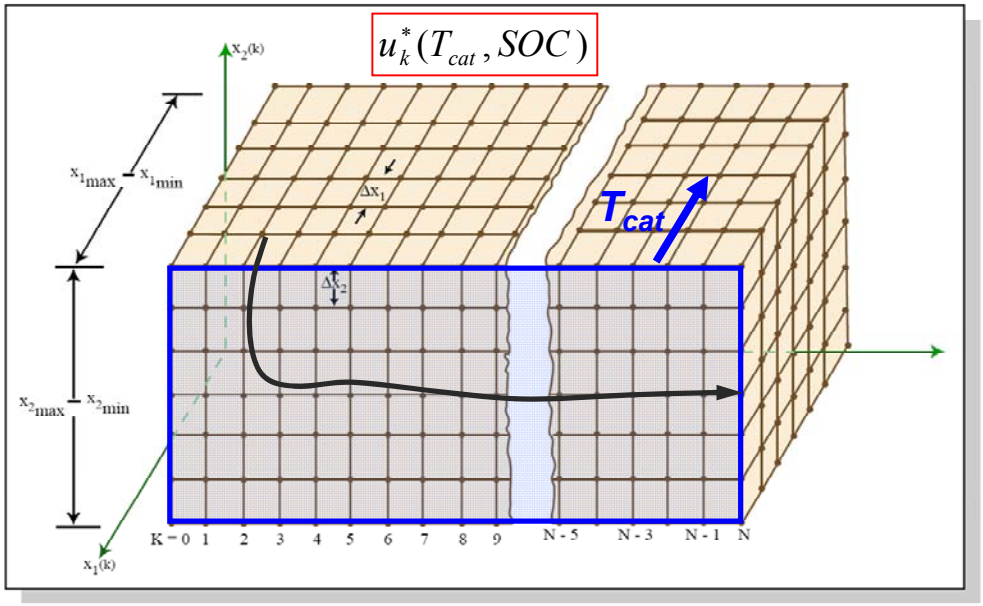

Figure 3.3: State space of the optimal control policy (u_k^*) showing the comprehensive extraction algorithm with a T_{cat} sweep.

3.2.1 Extraction algorithm

The idea of the comprehensive extraction method is to utilize all of the optimal control information found through DP, instead of a single optimal trajectory. Suppose that DP stores the optimal control information in the form of $u_k^*(T_{cat}, SOC)$, where values of u_k^* are stored for all state grid points at each time step k. Then, all u_k^* elements can be grouped together for each T_{cat} grid point as shown in Figure 3.3. The rectangular box represents the optimal control policy u_k^* in a state and time space, where x_1 is T_{cat} and x_2 is SOC, and k indicates the time step. Each node in the box contains the optimal control information for the given state (x_1,x_2) and time step k, and the curve represent the optimal trajectory. The following algorithm converts u_k^* into three useful forms of optimal control strategies, engine on/off ($u_{on/off}^*$), gear-shift (u_{Gear}^*), and Power Split Ratio (PSR) (u_{PSR}^*), where PSR is defined as

$$PSR \equiv \frac{P_{eng}}{P_{dem}} \tag{3.7}$$

Note that torque split ratio (TSR), which is defined as T_{eng}/T_{dem}, equals PSR for the pre-transmission parallel HEV since the engine speed (ω_e) equals transmission speed (ω_i) when the

clutch is engaged. Prior to the extraction algorithm, a designer must choose β that balances fuel economy and *HC* and obtain u_k^* for the chosen β. In this study, a relatively high penalty coefficient (β = 200) is chosen to see a cold-start control strategy that is clearly distinguishable from the hot strategy.

The extraction algorithm is described below:

a) Let time step k = 1 and obtain optimal control signal u_k^*.
b) Obtain driving cycle information (P_{dem}, T_{wheel}, V) at k = 1.
c) If $T_{wheel} > 0$, then continue to d). Otherwise, skip to step g).
d) For all T_{cat} and *SOC* grid points, convert u_k^* into two separate optimal control signals, gear selection (u_{gear}^*) and engine torque (T_{eng}^*). $u_{on/off}^*$ can be simply obtained by checking whether $T_{eng}^* = 0$ or not.
e) Find the optimal T_{dem}^* and ω_i^* using u_{gear}^*, and compute $u_{PSR}^* = \frac{T_{eng}^*}{T_{dem}^*}$
f) Store all u_{PSR}^*, u_{Gear}^*, and $u_{on/off}^*$ values into the new optimal control matrices to obtain $u_{PSR}^*(\omega_i, T_{dem}, T_{cat})$, $u_{Gear}^*(V, P_{dem}, T_{cat})$, $u_{on/off}^*(V, T_{wheel}, T_{cat})$, and $u_{on/off}^*(\omega_i, T_{dem}, T_{cat})$.
g) Repeat steps a) through f) for all k.

3.2.2 Extracted results

Two representative sets of optimal control matrices are selected for cold and hot strategies, T_{cat} = 420K and 700K respectively, and plotted in Figure 3.5-3.7. Extracted results for other temperatures are very similar to either T_{cat} = 420K or 700K results because the catalyst temperature quickly changes over a relatively narrow range of efficiency curve as Figure 2.19. Figure 3.5-3.7 indicate that all three control strategies, engine on/off, gear-shift, and *PSR*, should be adjusted during a cold-start for *HC* reduction. Figure 3.5(a) shows that the optimal engine on/off decision can be made based on the power demand at the wheel when the catalyst is hot. On the other hand, data points for the cold catalyst did not show a clear separation of engine on/off data. Instead, engine on/off data are much more distinguishable when they are plotted on a transmission input speed (ω_i) vs. torque demand at the transmission input (T_{dem}) plane as Figure 3.5(b) shows.

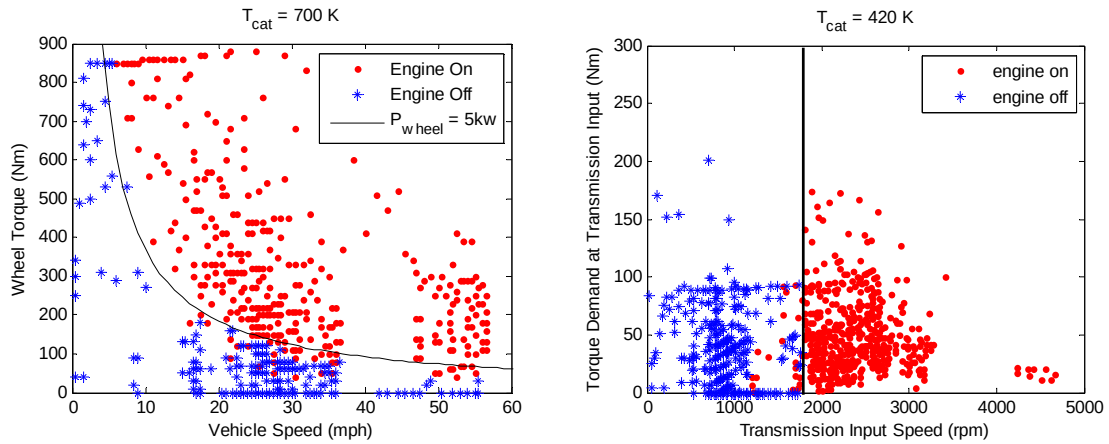

(a) T_{cat} = 700K (b) T_{cat} = 420K

Figure 3.4: Extracted DP engine on/off strategy at T_{cat} = 700K and 420K

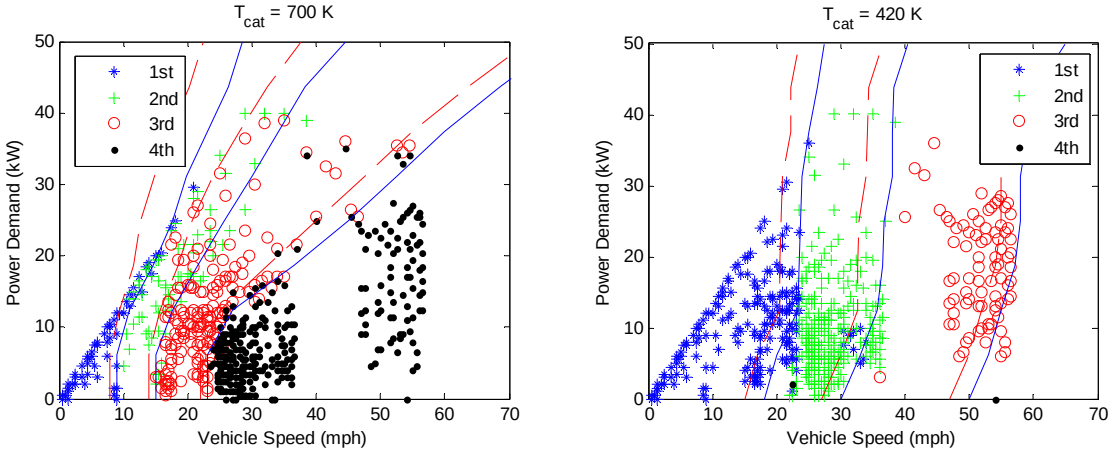

(a) T_{cat} = 700K (b) T_{cat} = 420K

Figure 3.5: Extracted DP shift strategy at T_{cat} = 700K and 420K

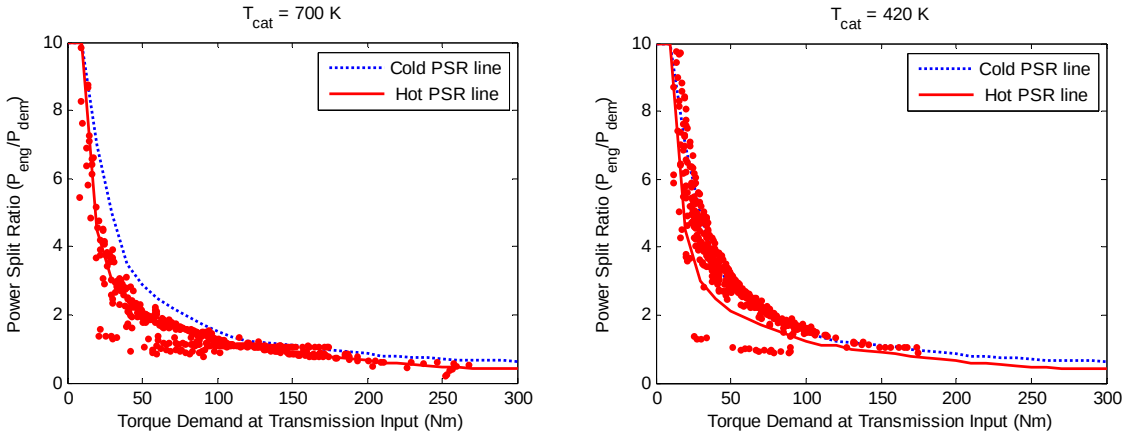

(a) T_{cat} = 700K (b) T_{cat} = 420K

Figure 3.6: Extracted DP power-split strategy at T_{cat} = 700K and 420K

Note that when the catalyst is cold, the engine is not turned on until ω_i reaches 1500 rpm, even when high power is demanded by the driver. This is to make sure that the engine operates at higher speed during cold-start. Figure 3.6 indicates that both cold and hot optimal shift strategies have clearly separable gear data on a V vs. P_{dem} plane, which allows use of a conventional shift-map. During cold-start, a late-shift strategy is necessary to promote faster catalyst warm-up by operating the engine at higher speeds. Figure 3.6 shows that cold and hot optimal *PSR* data points can be approximated by two separate lines. The cold *PSR* line is located higher than the hot *PSR* line for increased T_{exh} and faster catalyst warm-up. Note that *PSR* lines can be replaced by the optimal engine torque map, $T_{eng}^*(\omega_e, T_{dem}, T_{cat})$, where T_{eng}^* data are plotted on a T_e vs. T_{dem} vs. ω_e space to form optimal engine torque surfaces. This method includes ω_e as an additional axis for better approximation of DP results. In summary, the extracted results show that the engine on/off and shift strategy play key roles in achieving optimal charge management and fast catalyst warm-up by determining the optimal engine speed, while *PSR* mainly focuses on optimizing engine operations for the given speed. Therefore, the engine on/off and gear-shift control must be included in the optimal control problem formulation of the parallel HEV.

3.3 Design of Cold-start Supervisory Powertrain Controller

As discussed in the previous section, all extracted results can be classified by either a cold or hot strategy depending on whether the catalyst temperature reached the light-off temperature or not. Relatively fast catalyst warm-up coupled with switch-like performance of the catalyst is responsible for such results. These results allow us to design the DP-based cold-start SPC with two control modes, Hot and Cold SPC; each mode focuses on fuel economy and emissions respectively. Figure 3.4 shows the flowchart of the cold-start SPC with two modes. In this section, a cold-start SPC algorithm is developed based on the previous extracted results, and its hot-start and cold-start performances are compared to those of the instantaneous optimization methods.

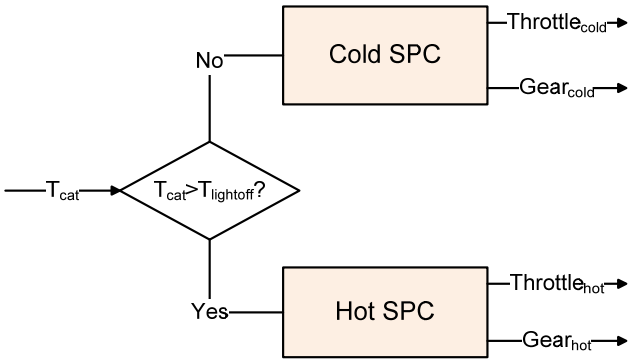

Figure 3.7: Flowchart of the cold-start SPC

3.3.1 Hot SPC algorithm

3.3.1.1 Instantaneous optimal controller (IOC)

The instantaneous optimization method, also known as static optimization method, is widely used for fuel economy optimization of the HEV due to its computational efficiency and easy implementation [68,80]. The Equivalent Consumption Minimization Strategy (ECMS) is a well-known instantaneous optimization strategy. This approach attempts to minimize the total fuel consumption by minimizing sum of the fuel consumption rate and battery energy consumption rate at every instant. Although the instantaneous approach does not guarantee a globally optimal solution as Equation (3.8) shows, researchers showed that the instantaneous approach achieves near-optimal performance when the battery efficiency map is independent of the battery SOC [80]. Readers are referred to the Appendix for more rigorous development of these cases.

$$J^* = \min J = \min \sum_{k=0}^{N} FC_k \le \sum_{k=0}^{N} \min FC_k \tag{3.8}$$

The instantaneous optimization problem is formulated as follows.

Problem formulation

The instantaneous optimization problem is formulated as follows.

$$\text{Minimize } J = Fuel_{rate}(x,u) - p \cdot \frac{dSOC}{dt}(x,u,d) \tag{3.9}$$

$$\text{Subject to } SOC_{final} = SOC_{inital} \tag{3.10}$$

where x is the state vector (V, SOC=0.6), u is the control input (Gr, T_{eng}), d is the disturbance input (P_{dem}), and p is a Lagrange multiplier, which is a weighting factor for the electric energy consumption rate and needs to be adjusted for the charge sustenance. SOC is fixed at 0.6 for reduced computation time, assuming small SOC deviation from a nominal value of 0.6. Note that the engine on/off and gear-shift penalties shown in Equation (3.5) inherently cannot be applied to the instantaneous optimization problems because they are horizon-based performance objectives. Since $dSOC/dt = -I_{batt}$, where I_{batt} is the current through the battery, Equation (3.9) is rewritten as follows.

$$\text{Minimize } J = Fuel_{rate}(x,u) + p \cdot I_{batt}(x,u,d) \tag{3.11}$$

Algorithm

The above instantaneous optimization problem is solved off-line, and the solution can be implemented as a supervisory control algorithm in the form of a full state feedback controller. The optimal control policy (u^*) is generated by the following algorithm.

a) Compute two instantaneous cost matrices ($Fuel_{rate}(x,u)$ and $I_{batt}(x,u,d)$) for all x, u, and d space using a quasi-static HEV model.
b) Choose p, and compute the cost matrix $J(x,u,d)$.
c) Find the optimal control policy, $u^*(x,d)$, that minimizes J.
d) Simulate the HEV model with $u^*(x,d)$ found. Check if $SOC_{final} = SOC_{min}$. If not, adjust p, and repeat c) and d) until the charge sustenance condition is met.

Note that the optimal control policy $u^*(x,d)$ is solved in a single computation step, but instantaneous costs must be computed over the entire state, control, and disturbance space. Also, no separate design of control algorithms for engine on/off, shift, and power-split strategies are necessary. Although such a centralized control algorithm is convenient to implement, it is difficult to modify or calibrate each control strategy for practical issues (e.g. frequent shift and engine on/off) without a loss of optimality, since two control inputs (T_e and Gr) are strongly coupled with each other in this policy.

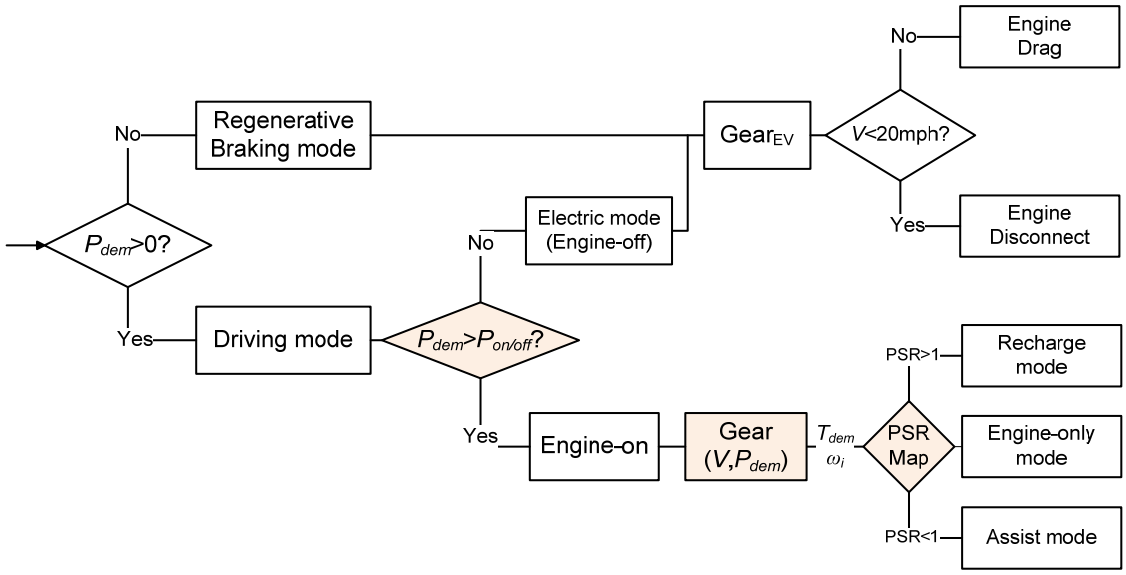

Figure 3.8: Flowchart of the DP-based SPC algorithm

3.3.1.2 DP-based Hot SPC

The logic of the DP-based Hot SPC algorithm for a hot TWC is described as follows.

If $P_{dem}<P_{on/off}$,
Turn off the engine and select the gear using the Electric Vehicle (EV) shift-map
$P_{m/g} = P_{dem}$
If V<20mph, then disengage the engine clutch
Else, engage the clutch.
Else,
Turn on the engine
Select the gear using the engine-on mode shift-map and find T_{dem} *and* ω_i
Find PSR from T_{dem} *and* N_i *and compute* $P_{eng} = PSR \cdot P_{dem}$
Compute M/G power: $P_{m/g} = P_{dem} - P_{eng}$
End

Core design parameters of the above algorithm to achieve near-optimal performance are engine on/off threshold power ($P_{on/off}$), shift-map, and *PSR* map. The flow chart of the proposed SPC algorithm is illustrated in Figure 3.8 to help visualize the rules described above. In this algorithm, the optimal engine on/off, gear, and *PSR* commands are determined sequentially because the *PSR* decision requires T_{dem} and N_i, which can only be determined after gear selection is made, and shift-map selection depends on the engine on/off decision. Embedding DP

information in this intuitive rule-based control structure provides implementable, near-optimal, and decoupled control logics of three sub-control modules: engine on/off, shift, and *PSR*.

3.3.2 Cold SPC algorithm

Two Cold SPCs are developed using horizon-based and instantaneous-based approaches. The Map-based SPC was developed based on the instantaneous optimization approach, and used as a benchmark to assess the performance of the DP-based Cold SPC.

3.3.2.1 DP-based Cold SPC

Since the extracted strategy of the cold-start DP solutions can be illustrated in the same state space as the hot results, the control algorithm of the DP-based Hot SPC shown in Figure 3.8 can be reused for the DP-based Cold SPC except for the engine on/off algorithm. Figure 3.4(b) shows that during a cold-start, the engine on/off logic is triggered by the transmission input speed (ω_i), instead of P_{dem}. For the gear-shift and power-split strategies, the hot-strategies (Figures 3.5(a) and 3.6(a)) are simply replaced by the cold-strategies (Figures 3.5(b) and 3.6(b)).

3.3.2.2 Map-based Cold SPC

No standard emission control algorithm was found in the literature to use as a benchmark, and an instantaneous optimization method using engine maps is proposed to design a benchmark cold-start control strategy for HC reduction. The idea of the Map-based Cold SPC is to find the optimal throttle and shift strategy that minimizes engine-out HC but maximizes the exhaust gas temperature for fast catalyst warm-up using transient engine maps. The static optimization problem is formulated and solved as follows.

Objective

Find the throttle (φ) and gear (Gr) that maximizes the following value function.

$$\begin{aligned} f(T_{inlet}, HC_{rate}, T_{cool}) &= T_{inlet}^{CF} - \delta \cdot HC_{rate}^{CF} \\ &= CF_{T_{inlet}}(T_{cool}) \cdot T_{inlet} - \delta \cdot CF_{HC}(T_{cool}) \cdot HC_{rate} \end{aligned} \tag{3.12}$$

where T_{inlet} and HC_{rate} are hot engine-maps, δ is a weighting factor for hydrocarbon, and CF_i is the correction factor for the engine output i. Maximizing the value function of Equation (3.12) will result in increased exhaust gas temperature at the catalyst inlet (T_{inlet}) and reduced engine-out hydrocarbon rate (HC_{rate}).

In Figure 3.9, a sample contour plot of the value function illustrates how the optimal throttle and gear combination that maximizes the value function can be computed. δ is selected by balancing fast warm-up and lower HC. The dashed line represents the optimal throttle line that maximizes the value function at each engine speed (ω_e), and this line changes as T_{cool} increases. Four x marks represent each gear selection on the optimal throttle line for a given vehicle speed. The optimal gear is selected by evaluating value functions at these four points. These points will move along the optimal throttle line as the vehicle accelerates.

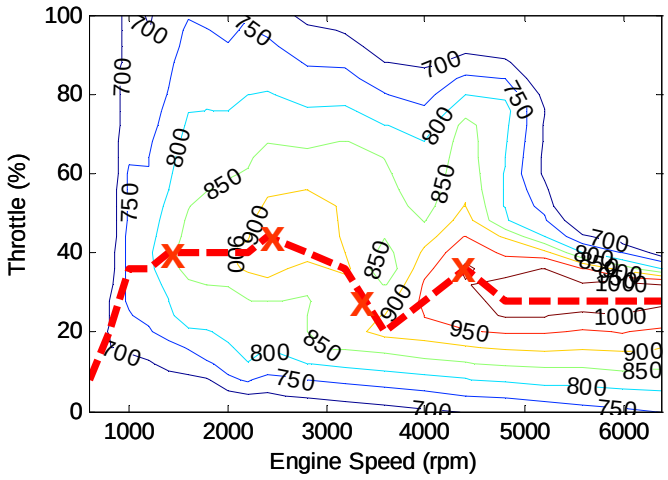

Figure 3.9: A sample contour plot of the value function f for T_{cool} = 350 K and δ = 8000

Off-line optimization algorithm

Since T_{inlet} and HC_{rate} are functions of φ and ω_e, the value function can be expressed as a function of φ, ω_e, and T_{cool}, i.e.

$$f(T_{inlet}, HC_{rate}, T_{cool}) \Rightarrow g(\varphi, \omega_e, T_{cool}) \tag{3.13}$$

The new value function g can then be used in the following off-line optimization algorithm.

a) For a given vehicle speed (V), an engine speed vector ($\boldsymbol{\omega_e}$) can be computed using the gear ratio vector (***Gr***).
b) For a given T_{cool} and $\boldsymbol{\omega_e}$ vector, the optimal throttle vector ($\boldsymbol{\varphi_{opt}}$) can be obtained from the pre-computed optimal throttle look-up table.
c) For given $\boldsymbol{\varphi_{opt}}$, $\boldsymbol{\omega_e}$, and T_{cool}, the value function $g(x)$ can be evaluated and compared with each other to find the optimal Gr and φ for given V and T_{cool}.
d) Repeat steps a) through c) for all V and T_{cool} to generate cold-start gear and throttle look-up tables, $Gr_{cold}(V, T_{cool})$, $\varphi_{cold}(V, T_{cool})$.

The overall structure of the algorithm described above is shown in Figure 3.10.

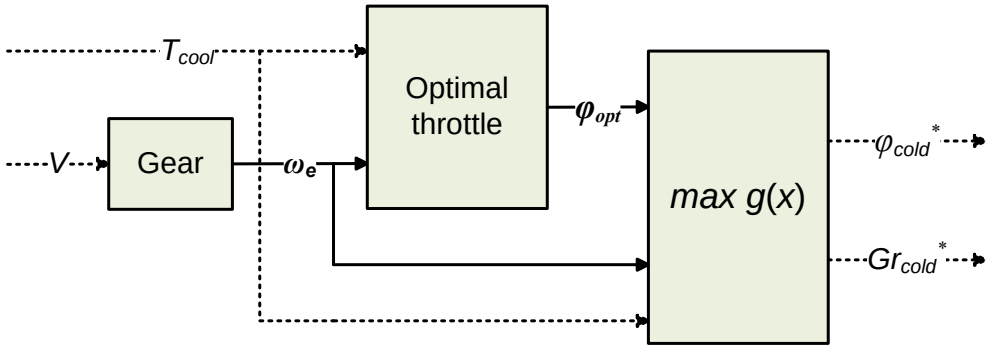

Figure 3.10: Block diagram of the instantaneous optimization algorithm for the Map-based SPC. (Solid line: vector, Dashed line: scalar)

3.4 Results and Discussion

3.4.1 Hot SPC algorithm – Fuel economy

First, the simulation results of the DP-based SPC are compared with the DP solution. Figure 3.11 shows that the control behavior of the DP-based Hot SPC is very similar to the original DP solution; i.e. the extraction was done successfully. One noticeable difference is that the gear-shift frequency of the DP-based SPC is significantly lower. This is a mainly achieved by adding hysteresis in the shift-map (Figure 3.5) at the expense of fuel economy.

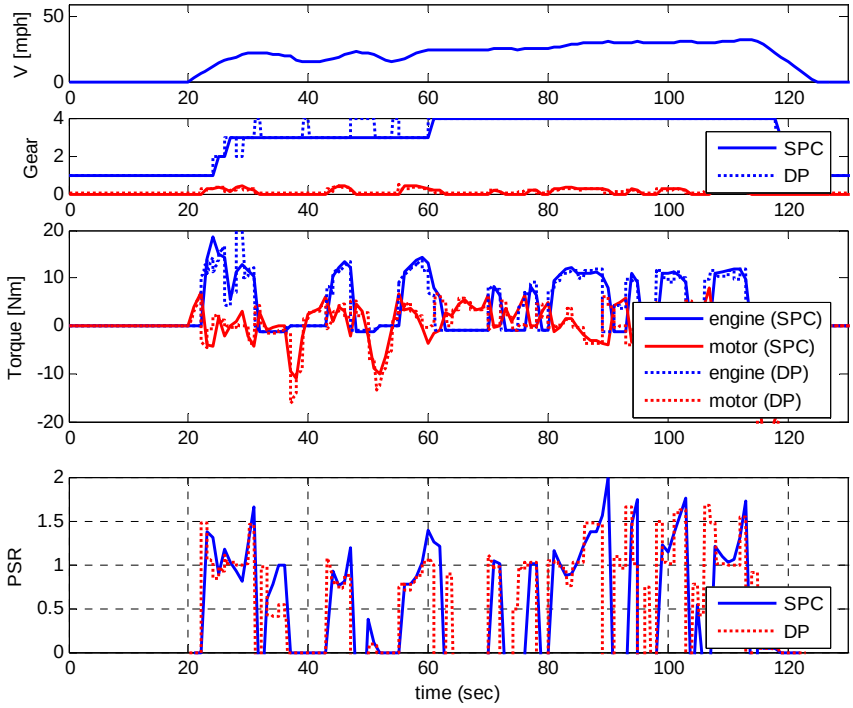

Figure 3.11: Simulation response comparison of DP vs. DP-based SPC for the hot-start FTP cycle

The simulation results of the DP, IOC, and DP-based Hot SPC are summarized in Table 3.3 for comparison. The results show that the IOC achieves near-optimal fuel economy, only 1.8% below the DP results, but the performance of the DP-based Hot SPC was not as good as the instantaneous approach. This indicates that the performance of the instantaneous approach is quite good for fuel economy. However, Table 3.3 indicates that the IOC experiences very frequent engine-on and gear-shifts, and these drivability issues must be resolved by better calibration or enhancement through a drivability algorithm. In fact, the instantaneous approach inherently suffers from the drivability issue, and it is difficult to resolve this issue without a loss of optimality because engine on/off, gear-shift, and power-split commands are coupled with each other. In contrast, the DP-based SPC is very easy to adjust the shift-map and the engine on/off threshold value without a significant loss of optimality because each control strategy is decoupled from one another.

Table 3.3: Comparison of DP, IOC, and DP-based Cold SPC simulation results on the FTP-72 cycle

Controller	DP (β =0)	IOC	DP-based Hot SPC
MPG [adjusted, hot-start]	40.32 (0%)	39.60 (-1.8%)	37.96 (-5.6%)
Fuel Consumption (g)	462.8 (0%)	471.8 (+1.9%)	489.8 (+5.8%)
Engine-on count	55	71	56
Shift count	159	222	116

3.4.2 Cold SPC algorithm – Fuel economy and emissions

Figure 3.12 shows that simulation responses of the DP-based SPC are very close to those of DP, and thus the cold-start DP control policy was successfully extracted.

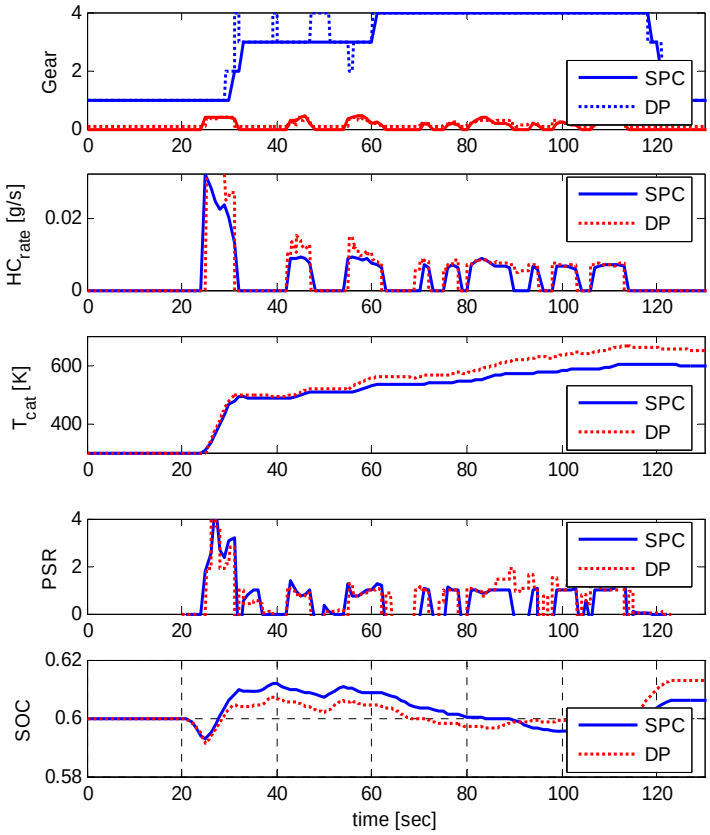

Figure 3.12: Simulation response comparison of DP vs. DP-based SPC for the cold-start FTP cycle

The DP-based Cold SPC is implemented and compared with DP and Map-based SPC. For a fair comparison, both DP-based and Map-based SPCs share the DP-based Hot SPC. Table 3.4 indicates that the DP-based Cold SPC achieves near-optimal performance and better performance than the Map-based SPC. In particular, *HC* performance is significantly affected by different cold-start control strategies. Compared to DP, tailpipe *HC* of the DP-based SPC increased by only 4.0%, while tailpipe *HC* of the Map-based SPC increased by 17.5%. One of the major factors for this substantial *HC* increase is the cold-start engine-on timing. The Map-based optimization problem is inherently unable to determine when the engine should be turned on/off, and its engine on/off algorithm remains unchanged from the DP-based Hot SPC.

Table 3.4: FC and HC combined performance comparison of DP, Map-based, and DP-based Cold SPC on the FTP-72 cycle

Controller	DP (β =200)	Map-based Cold SPC	DP-based Cold SPC
MPG [adjusted, cold-start]	39.66	37.44	37.56
Fuel Consumption (g)	470.5 (0%)	496.6 (+5.5%)	495.1 (+5.3%)
HC (mg/mile)	25.2 (0%)	29.6 (+17.5%)	26.2 (+4.0%)
Performance Measure $J=FC+200\ HC$ (g)	508.3 (0%)	541.0 (+6.4%)	534.4 (+5.2%)
Engine-on count	52	56	59
Shift count	150	116	116

CHAPTER 4
OPTIMAL CONTROL OF THE PLUG-IN HEV FOR FUEL ECONOMY AND EMISSIONS

Control of the Plug-in HEV (PHEV) poses a different challenge from that of the HEV due to the large battery capacity designed to be depleted throughout the drive cycle. In particular, when the trip distance exceeds the all electric range (AER), the optimal power management is non-trivial; i.e. an optimal control strategy for a particular trip distance may not be optimal for other trip distances. The AER is defined as the maximum distance a PHEV can travel from a single full discharge with minimum fuel consumption.

When emissions are considered, the optimal control of the PHEV becomes an even more complex problem because the PHEV is designed to dramatically reduce fuel consumption by frequent and extended engine shut-downs, which may lead to catalytic converter cool-down below the light-off temperature. In this chapter, we seek a systematic design method to synthesize a supervisory powertrain controller (SPC) that achieves near-optimal fuel economy and tail-pie emissions under known travel distances.

4.1 Design of the Target Plug-in HEV

The target PHEV of this study shares most of its powertrain components with the HEV's—except a larger battery and a more powerful motor are used. Main design variables of the PHEV are battery capacity and rated power of the battery and motor. Since high-capacity battery and high-powered power electronics are still very expensive, their sizes must be minimized. In this study, the battery capacity and propulsion power of the target PHEV are designed based on the following consideration.

a) 20 miles of AER is selected to keep the PHEV affordable while maintaining a reasonable electric range.

b) Based on Figure 4.1, 40kw battery and M/G is chosen to provide just enough electric propulsion power for electric vehicle (EV) operation on a light-loaded drive cycle, e.g. UDDS (FTP-72).

This choice of design makes this PHEV more suitable for city driving.

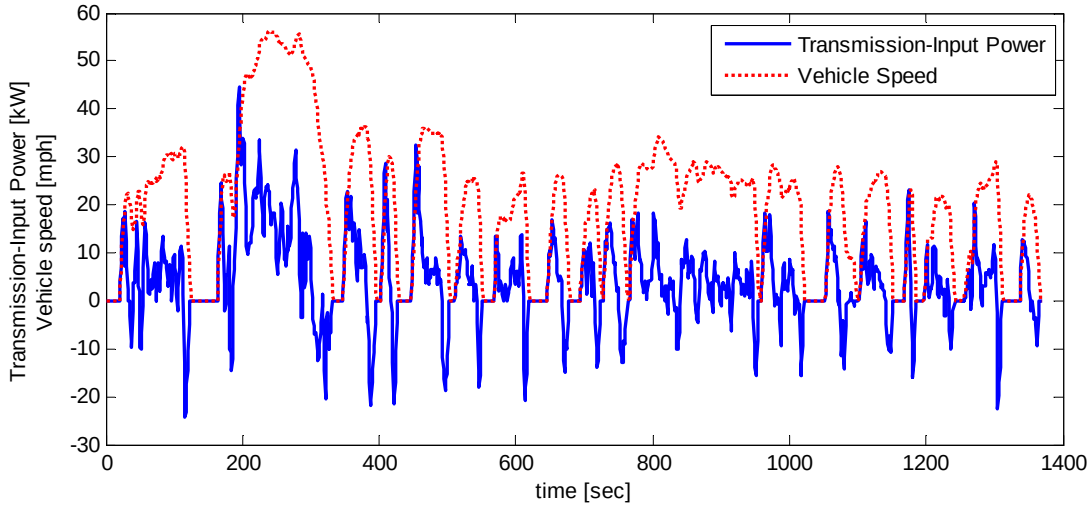

Figure 4.1: Transmission-input power profile of the target vehicle on the FTP-72 cycle.

4.2 Optimal Control via Dynamic Programming

As discussed in the Appendix, the near-optimality of the instantaneous optimization approach is guaranteed only if $\frac{\partial H}{\partial x}$ is negligibly small (see Appendix). When emissions are considered, $\frac{\partial HC}{\partial T_{cat}}$ has significant dynamics, and the near-optimality of the instantaneous optimization method no longer holds. Thus, a horizon optimal control method must be used to solve the combined fuel and emissions optimization problem of the PHEV, and a DP optimization problem is formulated and solved in this section.

4.2.1 DP problem formulation

The DP problem of the PHEV is slightly different from that of the HEV in Section 3.1, because PHEVs are designed to deplete the battery energy, whereas HEVs must maintain SOC. This implies that the PHEV only needs to maintain SOC above the minimum SOC while the HEV has the charge sustenance constraint, $SOC_{initial} = SOC_{final}$. Figure 4.2 illustrates these differences in the DP problem formulation by comparing sample SOC trajectories of the HEV and PHEV on a distance vs. SOC plane.

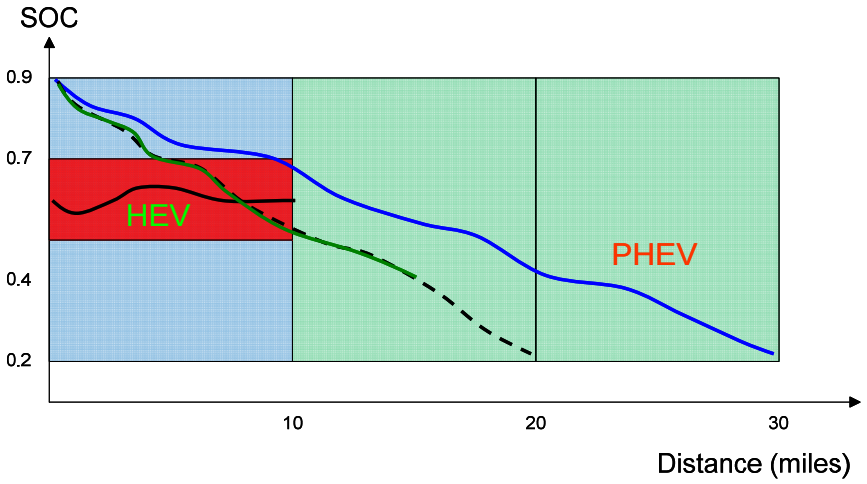

Figure 4.2: Sample SOC trajectories of an HEV and a PHEV on the Distance vs. SOC plane

The state-reduction technique used in Chapter 3 is applied to the PHEV model as well for computation reduction. Replacing the original coolant temperature dynamics (2.19) with (3.1) reduces the total number of dynamic states from three to two. Table 4.1 summarizes the variables and their grids in the DP problem, which consists of two control inputs and two dynamic states, whereas vehicle velocity (V) and power demand (P_{dem}) are specified by the driving cycle. LA-92 cycle, a high-power cycle, is selected to ensure that the engine turns on even for trip distances shorter than the AER, otherwise the optimal control solution is trivial (only use the battery). For extended travel distances, the LA-92 cycle, a 10 mile cycle, is repeated to generate 20 mile and 30 mile cycles, which allows for a significant reduction in computation time by reusing the transitional cost tables.

Table 4.1: Variables and grids of the PHEV DP problem for fuel and emission reduction

	Variables	Grid
Stage (k)	Time	[0:1:final time]
Control (u)	Gear (Gr)	[1 2 3 4]
	Engine torque (T_e)	[-1 0:5:200]
State (x)	SOC	[0.2:0.01:0.9]
	Catalyst temperature (T_{cat})	[300:40:700 900]

Note that the SOC range of the PHEV problem is much larger than that of the HEV problem due to the deep discharge capability. This makes the SOC variable to have many more grid points compared to the HEV case.

The optimal control problem is formulated as follows:

$$\text{Minimize } J = \sum_{k=0}^{N-1} \left(\alpha \max(SOC_{\min} - SOC_k, 0) + FC_k + \beta HC_k + \gamma \Delta Gr + \lambda \Delta E_{on/off} \right) \tag{4.1}$$

$$\text{Subject to } \begin{aligned} & SOC_k \geq SOC_{\min} \\ & \omega_{e,\min} \leq \omega_{e,k} \leq \omega_{e,\max} \\ & T_{e,\min} \leq T_{e,k} \leq T_{e,\max} \\ & T_{M/G,\min} \leq T_{M/G,k} \leq T_{M/G,\max} \\ & P_{batt,\min} \leq P_{batt} \leq P_{batt,\max} \end{aligned} \tag{4.2}$$

Due to numerical difficulties of implementing the minimum SOC constraint, the max(SOC_{min}–SOC_k,0) term is added in the cost function, and α must be adjusted to prevent SOC dropping below the minimum SOC while avoiding the large cost propagation (see section 3.1.1). One problem that may arise from this approach is that α may need to be adjusted when β is changed for FE vs. HC trade-off study. An α to β sensitivity study was conducted over a range of β values and showed very low sensitivity. In other words, α is quite robust to β, and no adjustment is necessary for the SOC constraint when β varied. Other numerical methods of DP, such as exact DP (no interpolation), were sought, but could not be applied due to the size of the state space. Penalties on engine on/off and gear-shift events are applied to improve drivability of the solution

and to promote separation of engine on/off modes and gear selections from one another for the extraction of these control strategies in section 4.4.

4.2.2 DP Results

The target PHEV is optimized for two trip distances (20 miles and 30 miles). For trip distances less than the AER (20 miles), the optimal solution is trivial, e.g. optimize electric drivetrain during EV mode and minimize fuel consumption when the power demand exceeds the battery power limit. Figure 4.5 shows DP simulation results of the 20-mile LA-92 cycle for $\beta = 0$ and $\beta = 500$. For the $\beta = 0$ solution, the engine is very lightly used only when the battery cannot supply the power demanded, which results in maximum charge depletion rate. The $\beta = 500$ solution reduces HC emissions by commanding higher engine-load for fast catalyst warm-up but with increased fuel consumption.

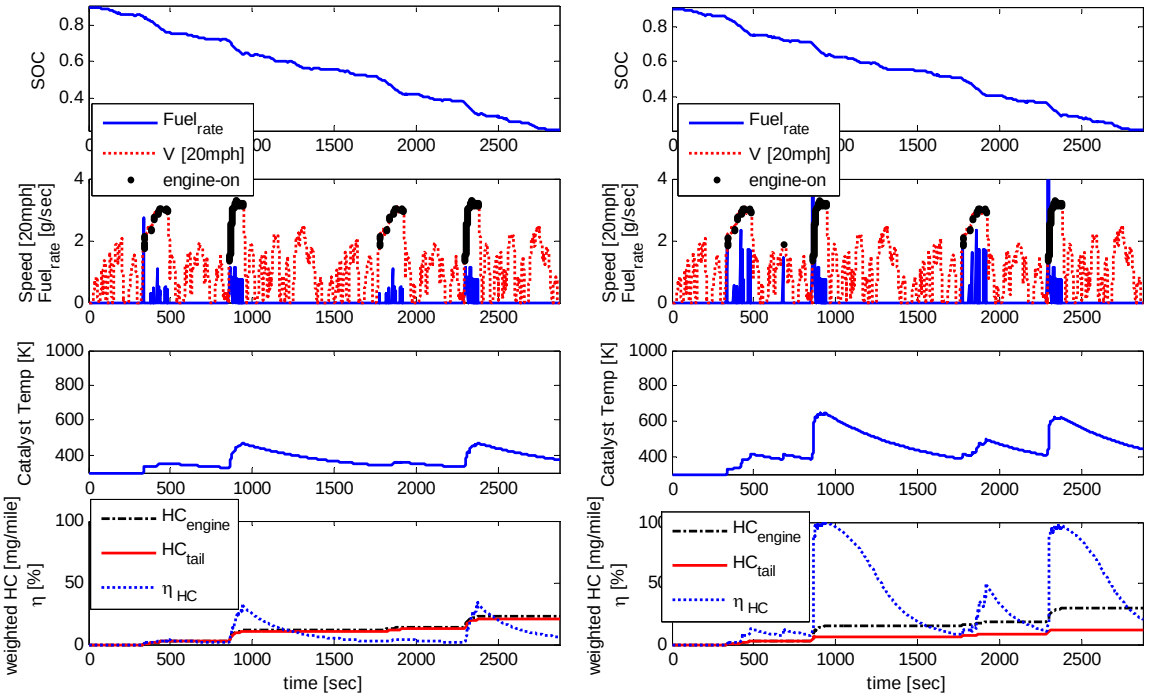

(a) $\beta = 0$ (b) $\beta = 500$

Figure 4.3: DP simulation results of the 20-mile LA-92 cycle at $\beta = 0$ and $\beta = 500$

For the 30 mile optimization, Figure 4.4 shows that the catalytic converter reaches the light-off temperature much faster than 20 mile cycle and maintains conversion efficiency high even for $\beta = 0$. The main reason is that significant engine operations are required due to the extended trip distance. The increased trip distance is another factor that keeps the weighted HC low. For the $\beta = 500$ solution, HC emissions are kept very low by fast catalyst warm-up and maintaining T_{cat} well above the light-off temperature to ensure full converter efficiency throughout the cycle. Note that all four optimal SOC trajectories slowly deplete in a controlled manner such that the final SOC barely touches the minimum SOC for both trip distances.

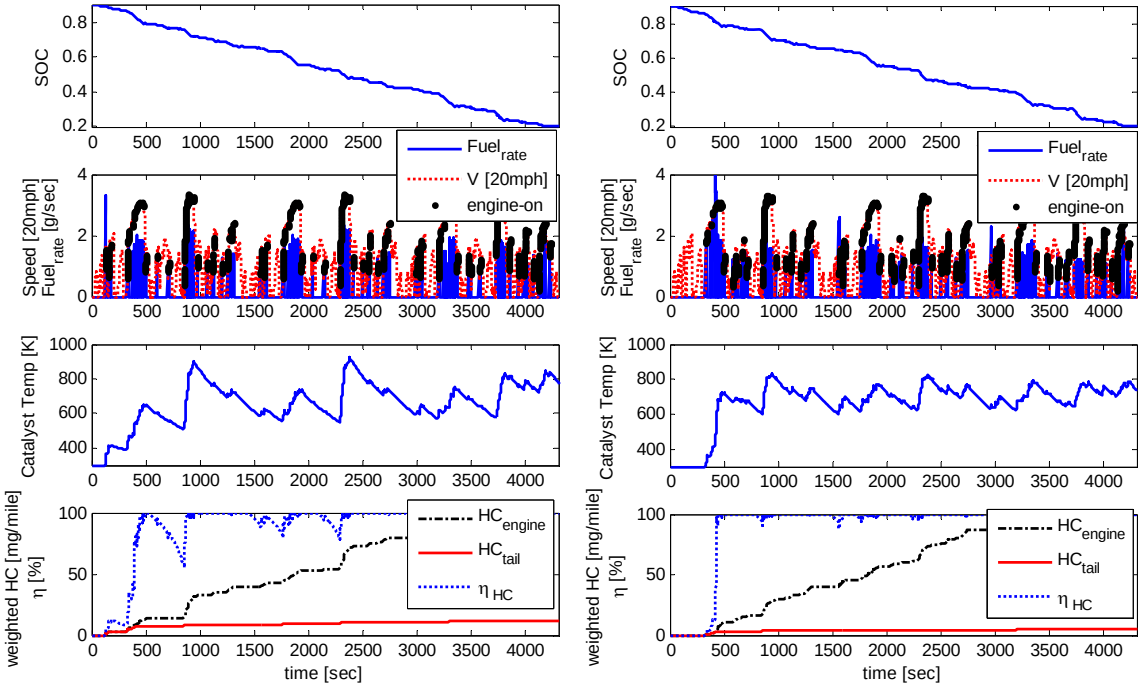

(a) $\beta = 0$ (b) $\beta = 500$

Figure 4.4: DP simulation results of the 30-mile LA-92 cycle at $\beta = 0$ and $\beta = 500$

For each trip distance, the trade-offs between fuel consumption (FC) and HC emissions are studied by varying coefficient β. Figure 4.5 shows two Pareto-curves that represent the FC vs. HC trade-offs for the 20 mile and 30 mile cycles. Detailed DP results are also provided in Table 4.2 and 4.3. DP results show that tailpipe HC can be significantly reduced at the expense of fuel economy loss. Note that the 20 mile cycle has a higher FC/HC sensitivity than the 30 mile cycle

and sacrifice more fuel to reduce HC. The main reason is that there is sufficient electric energy for the 20 mile cycle, and the increased engine-load and engine-on time for higher T_{cat} and conversion efficiency leads to increase in FC that was originally unnecessary when emissions are not considered. As of 2010, no special emission standards are available for the PHEV yet, and the SULEV standard of the conventional vehicle is shown as a reference.

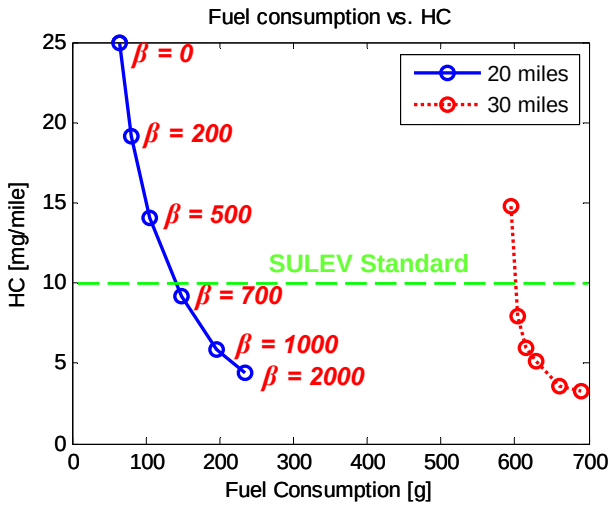

Figure 4.5: Trade-off between fuel consumption and HC for 20 mile and 30 mile cycles

Table 4.2: DP results showing trade-off between fuel economy and HC for the 20-mile LA-92 cycle

Penalty Coefficients	**$\beta = 0$** $\alpha = 0$ $\gamma = 0.02$ $\lambda = 0.05$	**$\beta = 200$** $\alpha = 0$ $\gamma = 0.02$ $\lambda = 0.05$	**$\beta = 500$** $\alpha = 0$ $\gamma = 0.02$ $\lambda = 0.05$	**$\beta = 700$** $\alpha = 0$ $\gamma = 0.02$ $\lambda = 0.05$	**$\beta = 1000$** $\alpha = 0$ $\gamma = 0.02$ $\lambda = 0.05$
MPG [unadjusted, coldstart]	842.2	676.9	515.4	365.3	277.1
Fuel Consumption (g)	64.8 (0%)	80.6 (+24.4%)	105.9 (+63.4%)	149.4 (+130.6%)	197.0 (+204.0%)
HC (mg/mile)	25.0 (0%)	19.2 (-23.2%)	14.1 (-43.6%)	9.2 (-63.2%)	5.9 (-76.4%)
Engine-on time (sec)	85	85	86	116	162

Table 4.3: DP results showing trade-off between fuel economy and HC for the 30-mile LA-92 cycle

Penalty Coefficients	**β = 0** α = 4e3 γ = 0.02 λ = 0.05	**β = 200** α = 4e3 γ = 0.02 λ = 0.05	**β = 500** α = 4e3 γ = 0.02 λ = 0.05	**β = 700** α = 4e3 γ = 0.02 λ = 0.05	**β = 1000** α = 4e3 γ = 0.02 λ = 0.05
MPG [unadjusted, coldstart]	137.8	135.6	133.2	130.2	123.8
Fuel Consumption (g)	594.1 (0%)	603.5 (+1.6%)	614.6 (+3.5%)	628.8 (+5.8%)	661.1 (+11.3%)
HC (mg/mile)	14.8 (0%)	7.0 (-52.7%)	5.9 (-60.1%)	5.2 (-64.9%)	3.6 (-75.7%)
Engine-on time (sec)	473	486	531	575	648

In order to understand how the optimal solutions change with respect to β for the 20 mile and 30 mile cycles, T_{cat} and engine efficiency distributions were analyzed. Figure 4.6 clearly shows that T_{cat} distribution shifts higher with increasing β for both 20 mile and 30 mile cycles. This shift is much more apparent for the 20 mile cycle than for the 30 mile cycle because the distribution of T_{cat} for 20 mile cycle with $\beta = 0$ is exceptionally low due to the limited engine operation, while insufficient electric energy for the 30 mile cycle requires more engine operation even for $\beta = 0$, which keeps the T_{cat} higher.

Figure 4.7 shows that with increasing β, the engine efficiency improves for the 20 mile cycle while drops for the 30 mile cycle. For the 20 mile cycle with $\beta = 0$, the engine turns on only when the battery cannot supply the demanded power, and the engine power is generally minimal to minimize fuel consumption, resulting in poor engine efficiency. When higher engine power is desired to maintain high T_{cat} and conversion efficiency, the engine operates at higher efficiency at the expense of increased fuel consumption. On the contrary, for the 30 mile cycle with $\beta = 0$, there are already sufficient engine power requirements to operate in the high efficiency region due to insufficient electric energy for the 30 mile cycle.

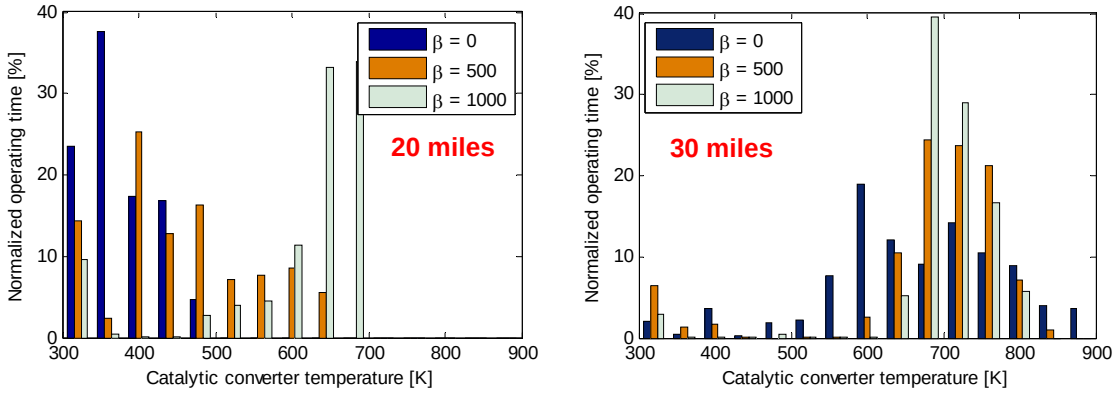

(a) Distance = 20 miles (b) Distance = 30 miles

Figure 4.6: T_{cat} distributions of DP solutions for 20 mile and 30 mile cycles

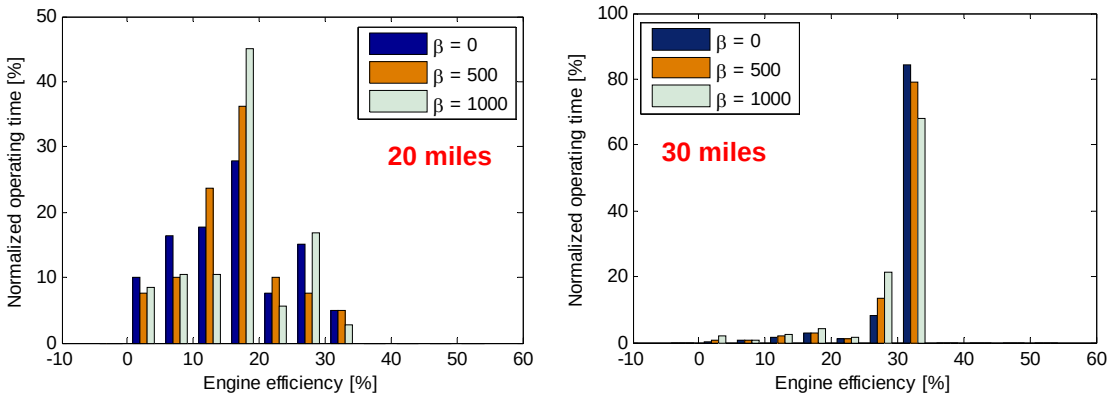

(a) Distance = 20 miles (b) Distance = 30 miles

Figure 4.7: Engine efficiency distributions of DP solutions for 20 mile and 30 mile cycles

Another important trend was observed from the optimal SOC trajectories. Figure 4.8 shows the optimal SOC trajectory of the 30 mile cycle with respect to distance. It can be seen that SOC depletes at a constant rate when plotted on a Distance vs. SOC plane, and this holds for all SOC and distance conditions. This is an important finding because if all optimal solutions behave in this manner this slope can be used to inform the controller how much electric energy is available and how fast the battery should be depleted for the optimal control. This is the key idea of the adaptive SPC to be illustrated in the rest of this chapter.

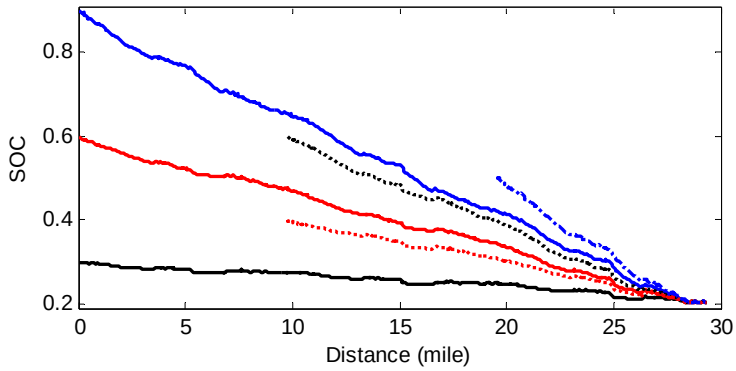

Figure 4.8: Optimal SOC trajectories on a Distance vs. SOC plane

One of the questions that may arise from the above observation is that whether the SOC slope will be constant when driving involves segments of very high power requirement and segments of low power requirement. In order to answer this question, another DP problem is solved for a cycle that consists of a FTP72 and a US06, which are the least and the most aggressive standard cycles respectively, as Figure 4.9 shows. The distance is 15.51 (7.5+8.01) miles, and this cycle is repeated twice to generate a 30 mile cycle.

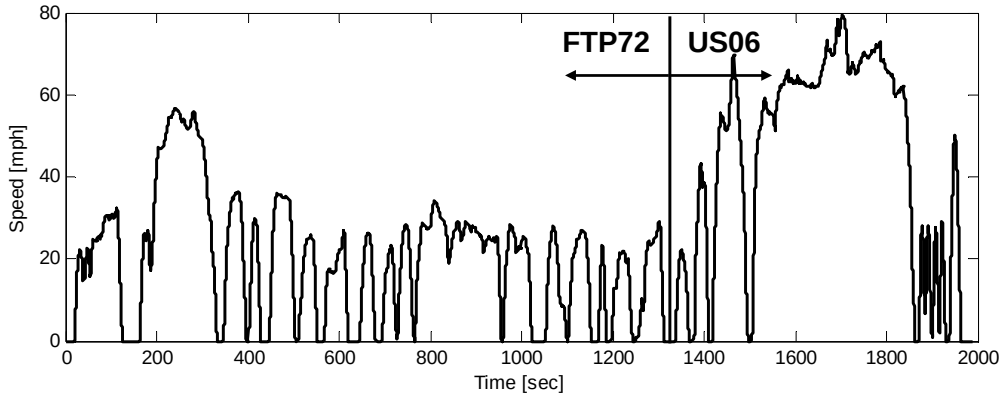

Figure 4.9: Vehicle speed profile of a cycle that consists of a FTP72 and a US06.

The optimal SOC trajectories for the above cycle are solved and plotted in Figure 4.10. DP results indicate that the slope is slightly affected by the cycle aggressiveness. Note that the battery is discharged at a faster rate during the light-loaded cycle (FTP) rather than the high-loaded one because the engine operations at high-speed high-load scenarios are efficient and using the

electric energy during the light-load cycle is more beneficial. Therefore, cycle aggressiveness should be considered as an uncertainty in finding the true EDR and the optimal control strategy.

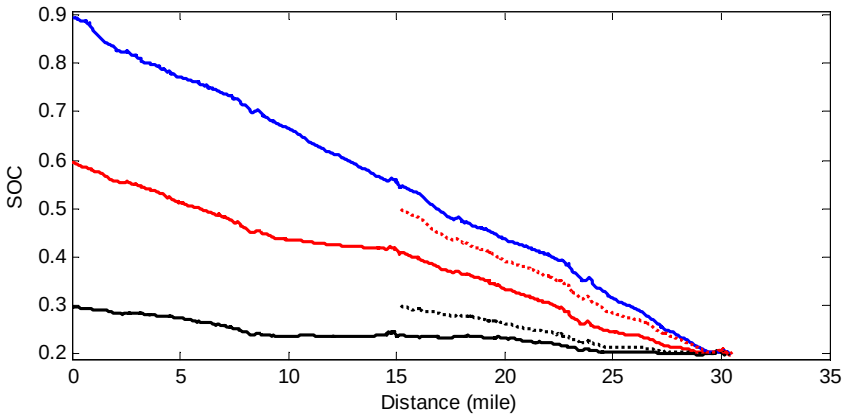

Figure 4.10: Optimal SOC trajectories for the FTP72+US06 cycle.

4.3 Introduction of Energy-to-Distance Ratio

Assuming that the cycle aggressiveness does not significantly changes throughout the cycle, a new variable, Energy to Distance Ratio (EDR), θ, is introduced to quantify this slope and to adaptively control the charge depletion rate. In particular, $\bar{\theta}$ is used as a key variable to construct an adaptive SPC from DP results. Assuming that the remaining trip distance (d_{rem}) is known, the EDR is defined as

$$\theta = \tan^{-1}\left(\frac{SOC - SOC_{\min}}{d_{rem}}\right) \approx \frac{SOC - SOC_{\min}}{d_{rem}} \tag{4.3}$$

where $\tan^{-1}$ can be removed under the small angle assumption, when the unit of distance is in miles, and SOC ranges 0 to 1. Note that

$$\theta \le \theta_{\max} \tag{4.4}$$

where $\theta_{\max} = \tan^{-1}\left(\frac{0.9-0.2}{20}\right) = 0.035$ (AER=20miles). Thus, we can normalize θ such that

$$\bar{\theta} \equiv \frac{\theta}{\theta_{\max}} \le 1 \tag{4.5}$$

Note that the AER value and θ_{max} may change with driving style or driving cycle, and θ would be a better choice to use for implementations in order to avoid the effect of cycle aggressiveness. Figure 4.11 illustrates the EDR, $\bar{\theta}$, on the SOC vs. distance plane and optimal SOC trajectories of a few samples of $\bar{\theta}$ values. $\bar{\theta}=1$ indicates sufficient electric energy available (or EV mode), and $\bar{\theta}=0$ indicates depleted battery (or charge-sustaining mode).

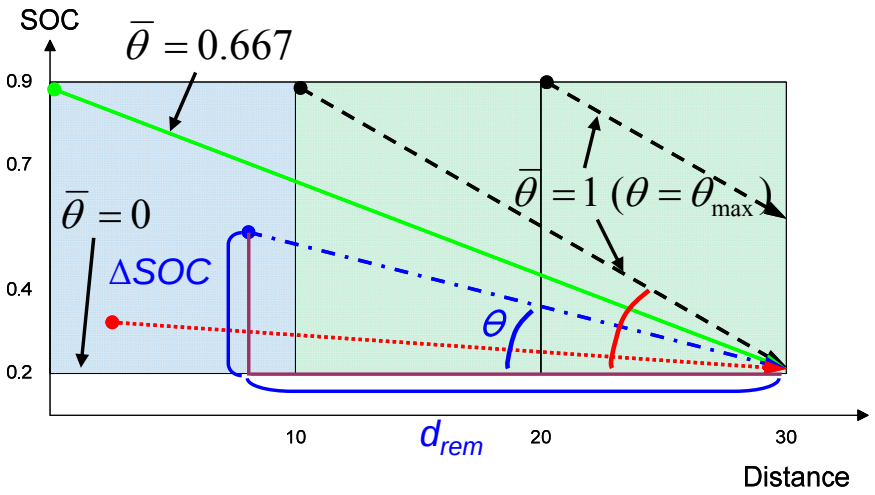

Figure 4.11: Geometrical definition of EDR (θ) on the Distance vs. SOC plane

4.4 Two-Dimensional Comprehensive Extraction Method

In section 3.2, a comprehensive extraction method that utilizes all of the optimal control information found from DP is proposed to learn and design the optimal cold-start strategy of HEVs. For PHEV control, this extraction method is expanded to a two-dimensional space (EDR and T_{cat}) because the control strategy of PHEVs must be properly adjusted depending on the EDR as well as the catalyst temperature for optimal fuel economy and emission performance. For example, the optimal cold-start control strategy for a high EDR condition (e.g. EV mode) would be different from that for a low EDR condition (e.g. charge sustaining strategy). In this section, two sets of optimal control strategies (hot and cold) are extracted to learn and design an optimal cold-start PHEV controller under various EDR conditions.

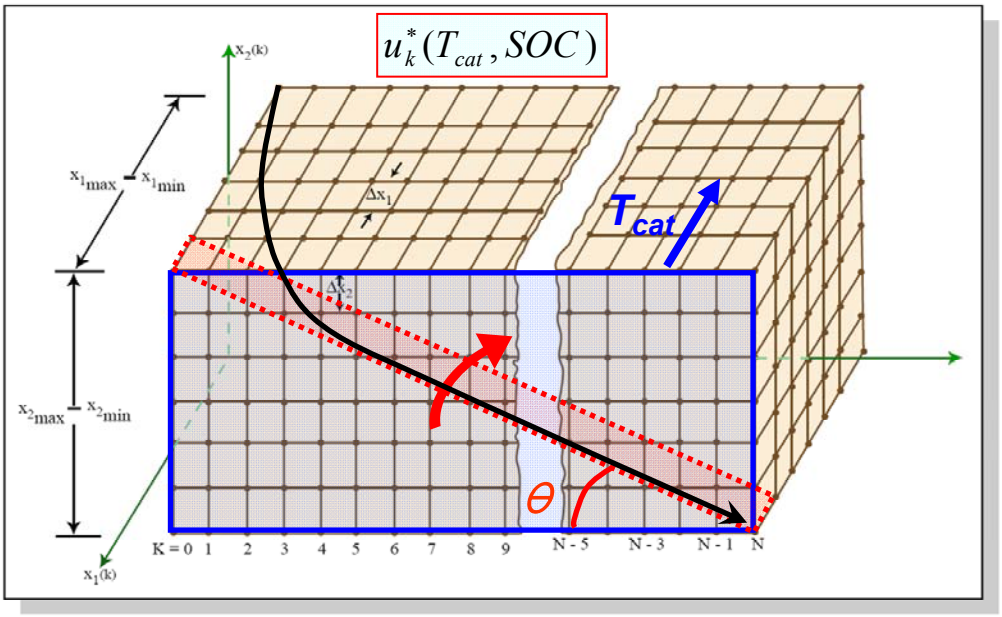

Figure 4.12: State space of the optimal control policy (u_k^*) showing the two-dimensional comprehensive extraction algorithm with $\bar{\theta}$ and T_{cat} sweeps.

4.4.1 Two-dimensional extraction algorithm

Suppose that DP stores the optimal control information in the form of $u_k^*(T_{cat}, SOC)$, where values of u_k^* are stored for all state grid points at each time step k. Then, all u_k^* elements can be grouped together by either $\bar{\theta}$ or T_{cat} as shown in Figure 4.12. The rectangular box represents the optimal control policy u_k^* in a state and time space, where x_1 is T_{cat} and x_2 is SOC, and k indicates the time step. Each node in the box contains the optimal control information for the given state (x_1,x_2) and time step k. The following algorithm converts u_k^* into three decoupled optimal control strategies, engine on/off ($u_{on/off}^*$), gear-shift (u_{Gear}^*), and Power Split Ratio (PSR) (u_{PSR}^*). Prior to the extraction algorithm, a designer must choose β that balances fuel economy and HC emissions and obtain u_k^* for the chosen β. In this study, β = 500 of the 30 mile cycle is selected but the optimal control policy of the 20 mile cycle could also be used because it also contains various EDR solutions.

The two-dimensional extraction algorithm is described as follows:

a) Choose T_{cat} = 300K.

b) Let time step k = 1 and obtain the corresponding optimal control policy u_k^*.

c) Obtain driving cycle information (P_{dem}, T_{wheel}, V, d_{rem}) at k = 1, where d_{rem} is the remaining distance.

d) If $T_{wheel} > 0$, then continue to e). Else, store engine-off and EV gear information into $u^*_{on/off}(V, T_{wheel}, \bar{\theta}, T_{cat})$, $u^*_{on/off}(\omega_i, T_{dem}, \bar{\theta}, T_{cat})$, and $u^*_{EVGear}(V, P_{dem}, \bar{\theta}, T_{cat})$ matrices, and skip e) through g).

e) For all SOC grid points at the chosen T_{cat}, compute $\bar{\theta}$ and convert u_k^* into two separate optimal control signals, gear selection (u_{gear}^*) and engine torque (T_{eng}^*). $u_{on/off}^*$ can be simply obtained by checking whether $T_{eng}^* = -1$ or not.

f) Find the optimal T_{dem}^* and ω_i^* using u_{gear}^*, and compute $u^*_{PSR} = \frac{T^*_{eng}}{T^*_{dem}}$

g) Store all $u_{on/off}^*$, u_{PSR}^*, and u_{Gear}^* values into matrices to obtain $u^*_{on/off}(V, T_{wheel}, \bar{\theta}, T_{cat})$, $u^*_{on/off}(\omega_i, T_{dem}, \bar{\theta}, T_{cat})$, $u^*_{Gear}(V, P_{dem}, \bar{\theta}, T_{cat})$, and $u^*_{PSR}(\omega_i, T_{dem}, \bar{\theta}, T_{cat})$.

h) Repeat steps b) through g) for all time step k.

i) Repeat steps a) through h) for all other T_{cat}.

This algorithm generates a set of five matrices that are functions of both EDR and T_{cat}.

$$u^*_{on/off}(V, T_{wheel}, \bar{\theta}, T_{cat}) \tag{4.6}$$

$$u^*_{on/off}(\omega_i, T_{dem}, \bar{\theta}, T_{cat}) \tag{4.7}$$

$$u^*_{Gear}(V, P_{dem}, \bar{\theta}, T_{cat}) \tag{4.8}$$

$$u^*_{EVGear}(V, P_{dem}, \bar{\theta}, T_{cat}) \tag{4.9}$$

$$u^*_{PSR}(\omega_i, T_{dem}, \bar{\theta}, T_{cat}) \tag{4.10}$$

4.4.2 Extracted results

4.4.2.1 Extraction of hot DP results (T_{cat} > 700K)

Four sets of the optimal control strategies under $\bar{\theta} = [0.02 \quad 0.35 \quad 0.6 \quad 0.97]$ at T_{cat} = 900K are selected and plotted in Figure 4.13, 15, and 16. These figures show that $\bar{\theta}$ has significant influences on the engine on/off and gear-shift strategies, while the power-split strategy is not affected by $\bar{\theta}$. Figure 4.13 shows that the optimal engine on/off decision can be made by P_{dem}

(power demand at the wheel), and this threshold value increases with $\bar{\theta}$, which agrees with the intuition that the PHEV should use more electric energy when the battery energy is abundant. The threshold P_{dem} values are plotted on a P_{dem} vs. $\bar{\theta}$ plane in Figure 4.14.

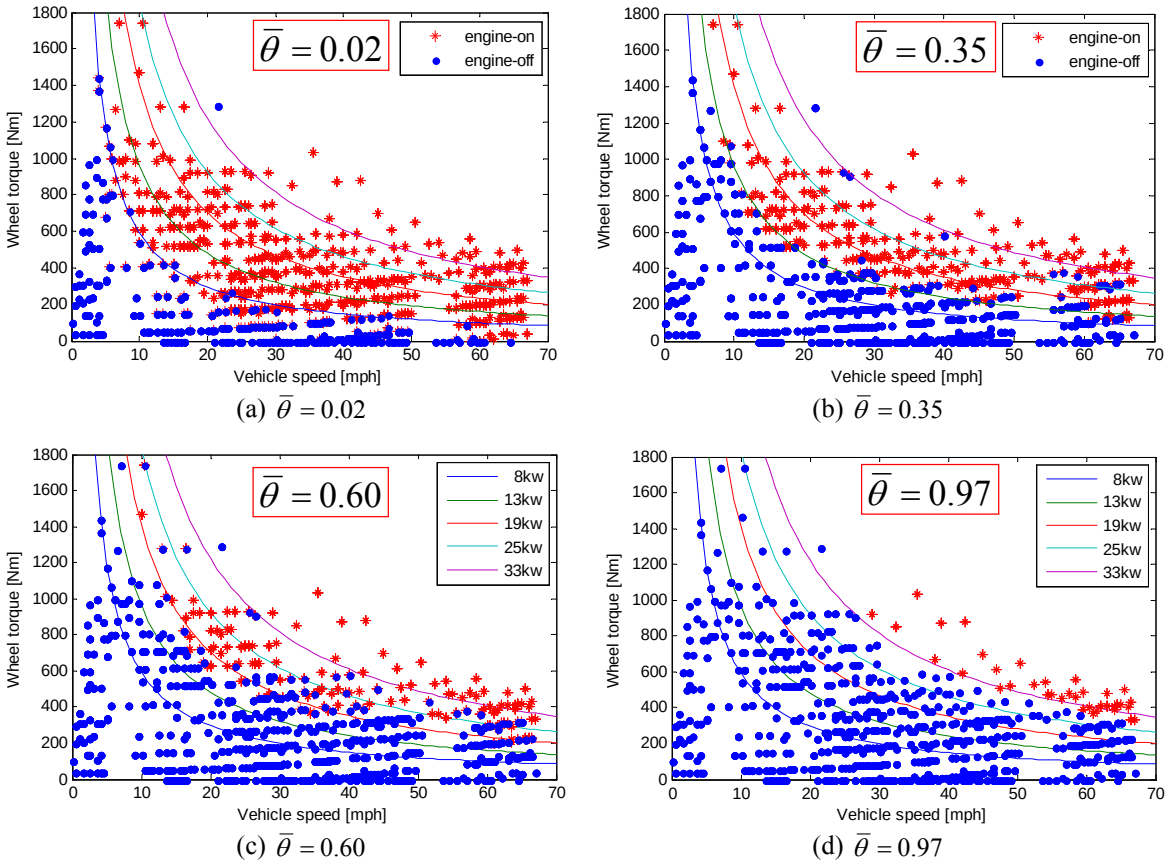

Figure 4.13: Extracted hot-catalyst engine on/off strategies at four sample $\bar{\theta}$ values

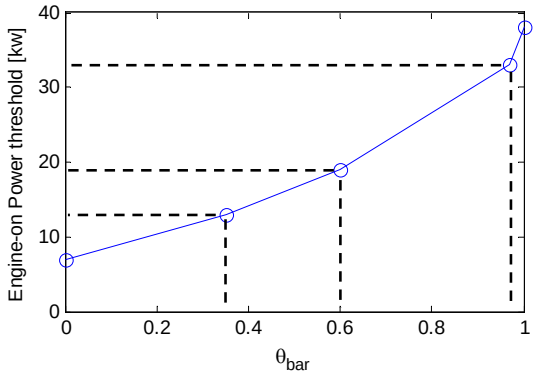

Figure 4.14: Extracted hot-catalyst engine on/off power threshold as a function of $\bar{\theta}$

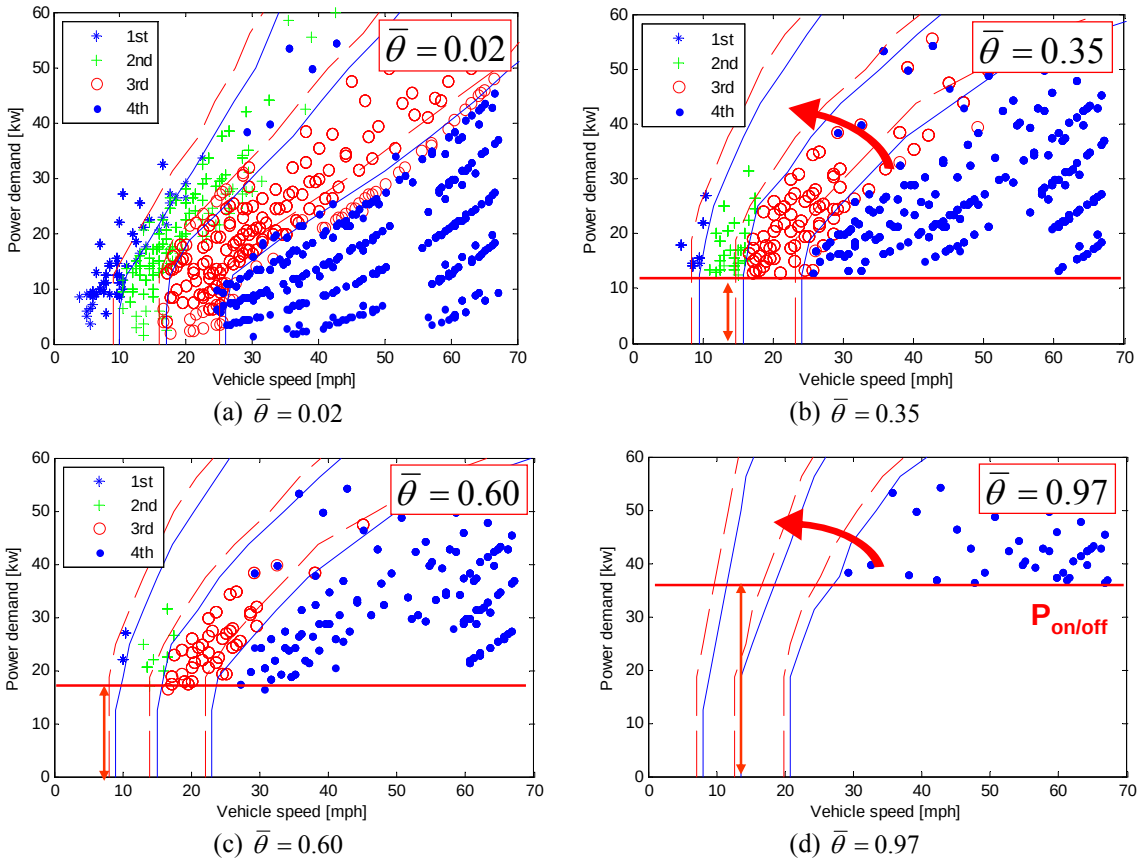

(a) $\bar{\theta} = 0.02$ (b) $\bar{\theta} = 0.35$

(c) $\bar{\theta} = 0.60$ (d) $\bar{\theta} = 0.97$

Figure 4.15: Extracted hot-catalyst shift strategies at four sample $\bar{\theta}$ values

Figure 4.15 shows that the optimal shift maps can be generated on a V vs. P_{dem} plane, and they gradually change with $\bar{\theta}$. With increasing $\bar{\theta}$, the shift lines become upright, which leads to early-shifts. This is an important finding because the importance of the shift strategy was often overlooked, and a fixed shift strategy was commonly used. The effect of the shift strategy will be further discussed with *PSR* strategy analysis. Note that the number of data points reduces as $\bar{\theta}$ increases because only engine-on data points are used for the extraction of the hybrid mode shift strategy, and an expected shift-map is created for $\bar{\theta} = 0.97$ based on the trend found from the extraction results. Also, the engine on/off threshold line is drawn as a reference, and this trend agrees with the previous engine on/off analysis.

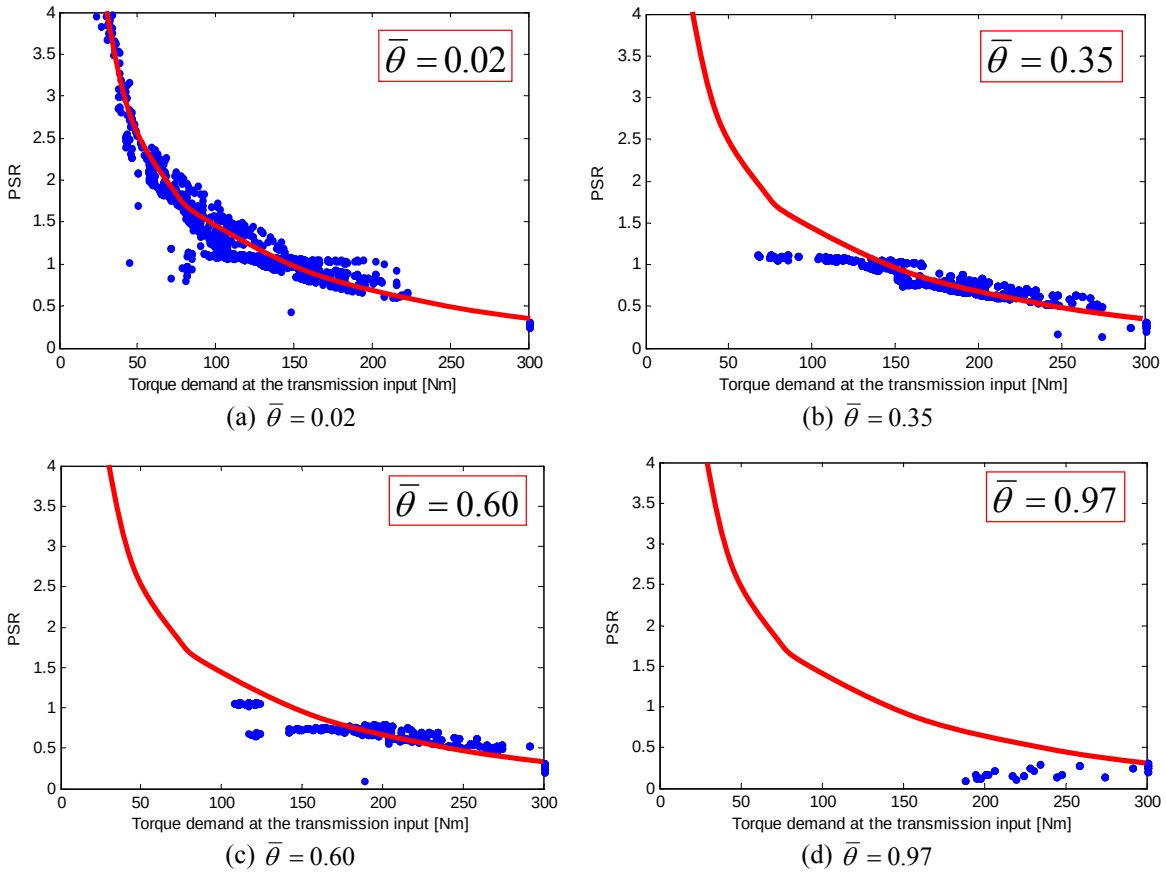

(a) $\bar{\theta} = 0.02$ (b) $\bar{\theta} = 0.35$

(c) $\bar{\theta} = 0.60$ (d) $\bar{\theta} = 0.97$

Figure 4.16: Extracted hot-catalyst power-split strategies at four sample $\bar{\theta}$ values

Figure 4.16 shows that the optimal *PSR* data points can be approximated by a curved line when plotted on a *PSR* vs. T_{dem} plane. It is interesting to see that the line itself does not need a significant change, but the optimal *PSR* data points shift toward high T_{dem} region when $\bar{\theta}$ increases. This observation coupled with the shift-map analysis depicts that the *PSR* line is determined to primarily maximize engine efficiency, and the shift-map is responsible for the optimal charge management. For instance, if fast charge depletion is desired to minimize fuel consumption, early-shift is necessary to command high T_{dem} and low *PSR*, which leads to power-assist mode. On the other hand, if there is not enough SOC to displace fuel consumption, high *PSR* is desired for recharge mode, which can be achieved by late-shifts. Note that different set of $\bar{\theta}$ was used to obtain four different power-split strategies.

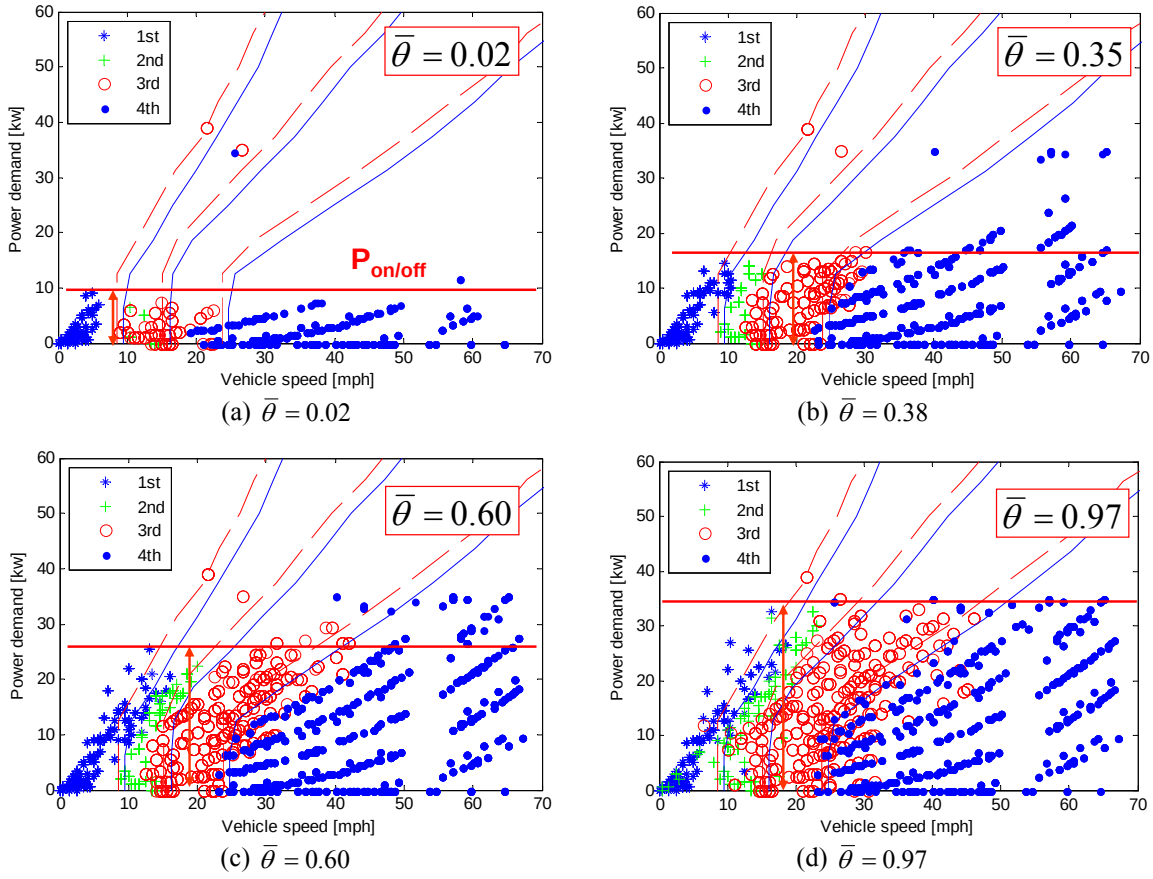

(a) $\bar{\theta} = 0.02$ (b) $\bar{\theta} = 0.38$

(c) $\bar{\theta} = 0.60$ (d) $\bar{\theta} = 0.97$

Figure 4.17: Extracted EV shift strategies at four sample $\bar{\theta}$ values

Shift and *PSR* control strategies discussed above dictate how to control transmission, engine, and motor when the engine is running (hybrid mode). When the engine is turned off, the sole control variable is the gear selection, and the static optimization method can be used to maximize M/G + transmission efficiency. However, the optimal EV control policy is already available from the DP results, and EV shift-map is obtained through the same extraction method and plotted in Figure 4.17. Note that limited data points are available for low $\bar{\theta}$ because only engine-off data are used. From the above results, it seems unnecessary to adjust the EV shift-map.

In summary, the extracted results show that the engine on/off and shift strategies should change with various $\bar{\theta}$. Therefore, both the engine on/off and gear-shift strategies should not be pre-determined, and all three control strategies, engine on/off, gear-shift, and power-split strategies, must be solved together in the optimal control problem.

4.4.2.2 Extraction of cold DP results ($T_{cat} \leq 700$K)

For the cold-start control strategy, T_{cat} = 420K is selected and plotted in Figure 4.18-4.20 using the same set of $\bar{\theta}$ values as the hot results. In general, the cold-start strategy of the PHEV is found to be similar to that of the HEV. In fact, low-EDR extracted results are almost identical to those of conventional HEVs (i.e. HEVs use a charge sustaining strategy), but the transition from hot to cold strategy is gradual and initiated at a higher temperature than the catalyst light-off temperature. However, as $\bar{\theta}$ increases, the optimal cold-start strategies become interesting.

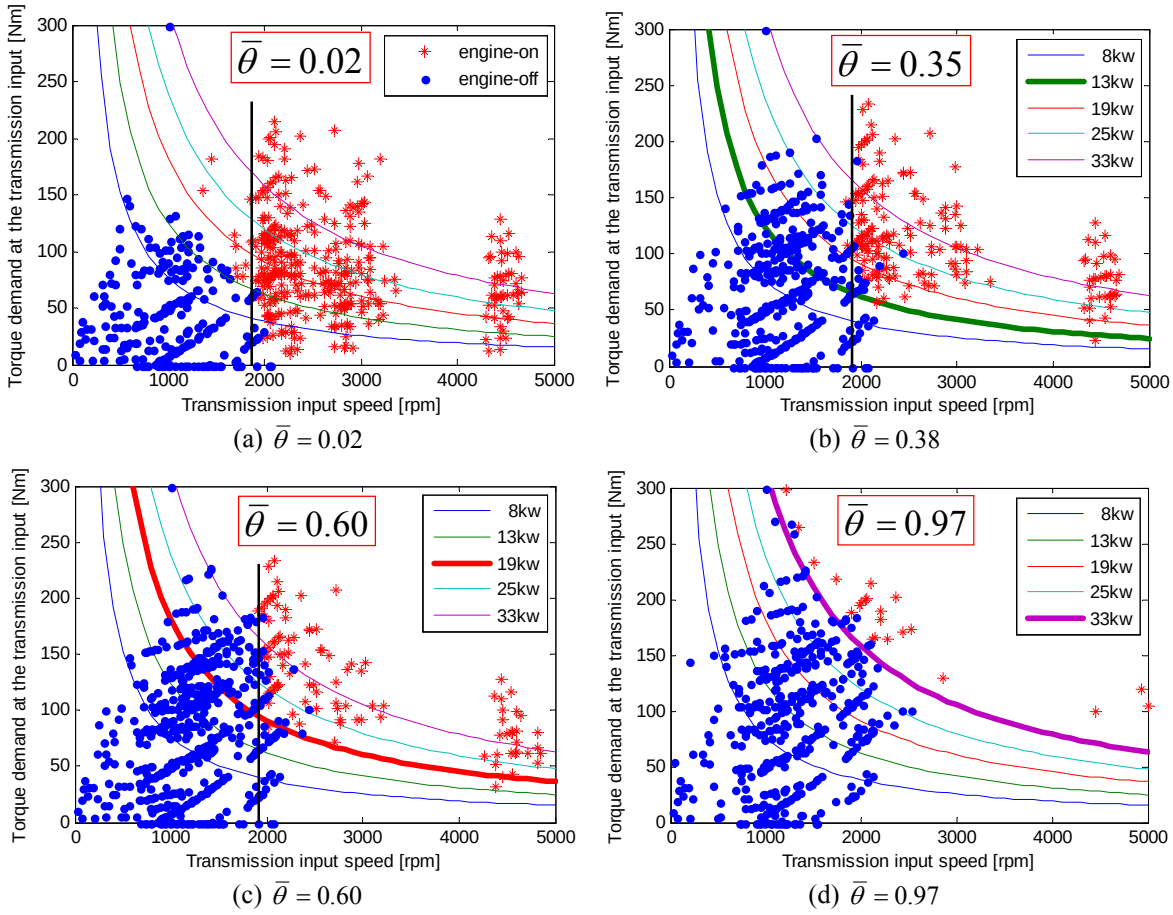

(a) $\bar{\theta} = 0.02$ (b) $\bar{\theta} = 0.38$

(c) $\bar{\theta} = 0.60$ (d) $\bar{\theta} = 0.97$

Figure 4.18: Extracted cold-start engine on/off strategies at four sample $\bar{\theta}$ values

Figure 4.18 shows that the engine on/off should be triggered by the transmission input speed as the conventional HEV case, but a major difference between the PHEV and the HEV results is that the power threshold also needs to be applied to limit the use of engine with increasing $\bar{\theta}$.

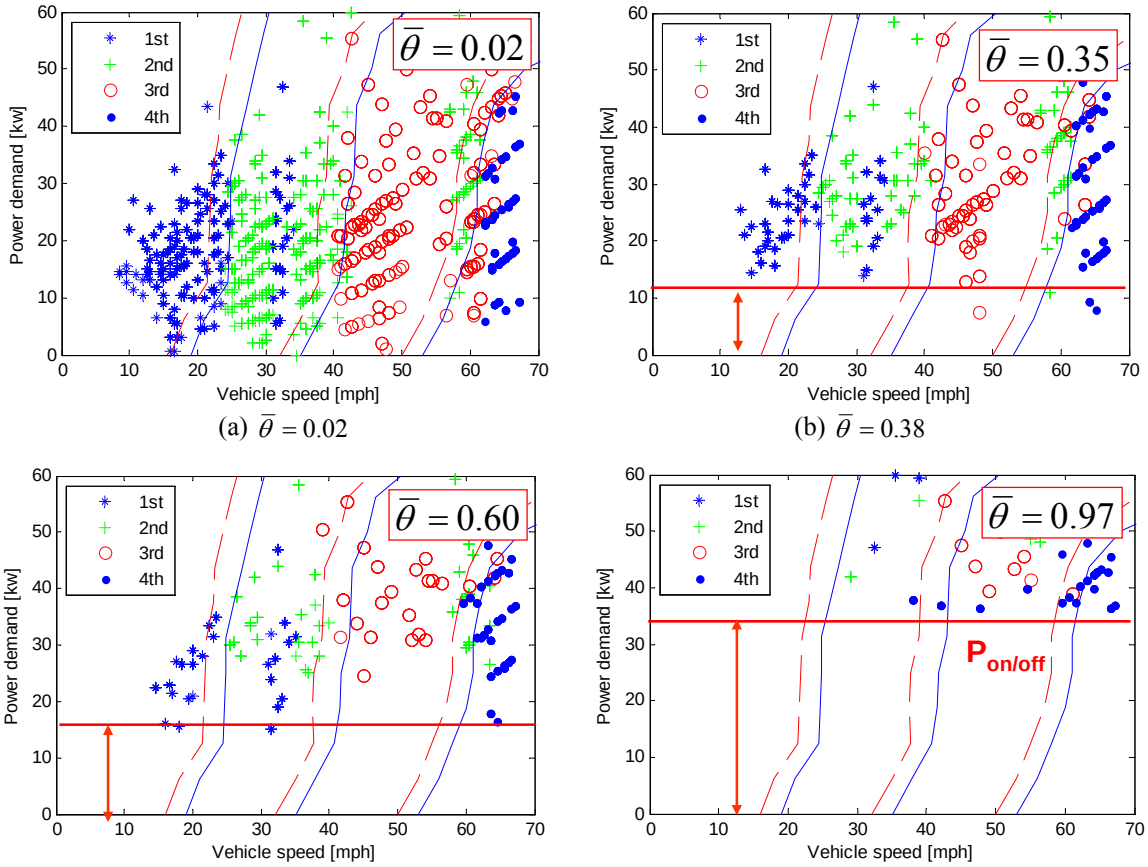

(a) $\bar{\theta} = 0.02$ (b) $\bar{\theta} = 0.38$

(c) $\bar{\theta} = 0.60$ (d) $\bar{\theta} = 0.97$

Figure 4.19: Extracted cold-start shift strategies at four sample $\bar{\theta}$ values

Figure 4.19 indicates that the late-shift is desired for the higher exhaust gas temperature. Again, the low $\bar{\theta}$ results are identical to those of HEVs, and this late-shift strategy does not significantly change with increasing $\bar{\theta}$ except for the increasing power threshold, as shown in Figure 4.18. For the cold-start power-split strategy, Figure 4.20 shows that a different *PSR* line should be used for increased engine-loads during cold-starts to promote higher exhaust gas temperature. This is very similar to the HEV results, but the powertrain needs to operate in the low PSR region for high $\bar{\theta}$ values.

In summary, the major difference in the cold-start strategy between conventional HEVs and PHEVs is that additional condition of the power threshold is needed for the engine on/off algorithm.

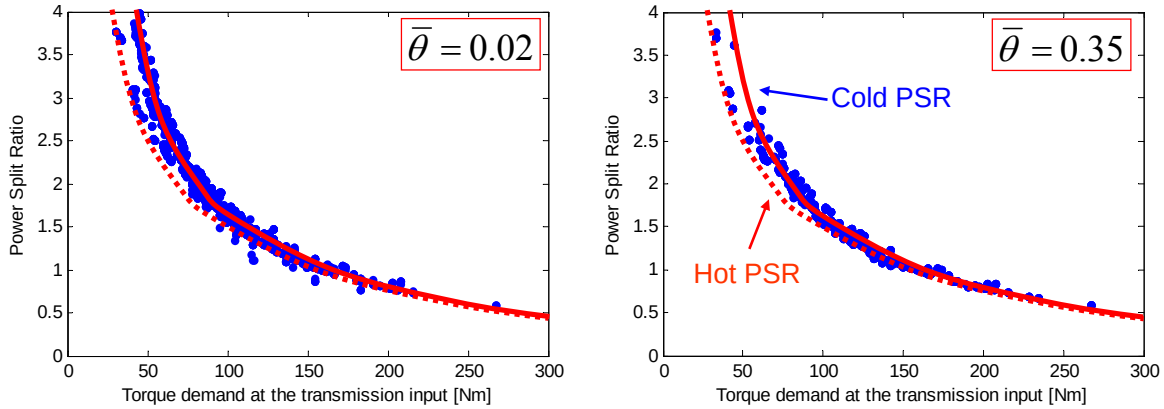

(a) $\bar{\theta} = 0.02$

(b) $\bar{\theta} = 0.38$

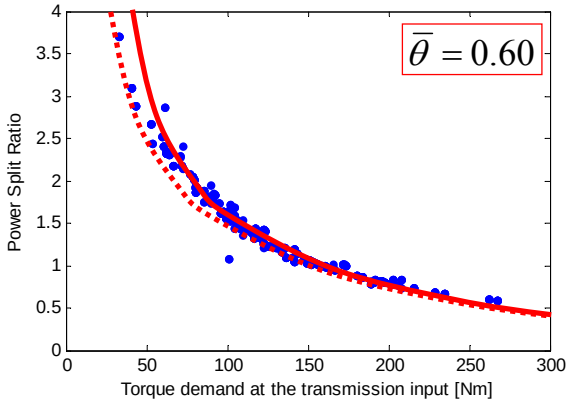

(c) $\bar{\theta} = 0.60$

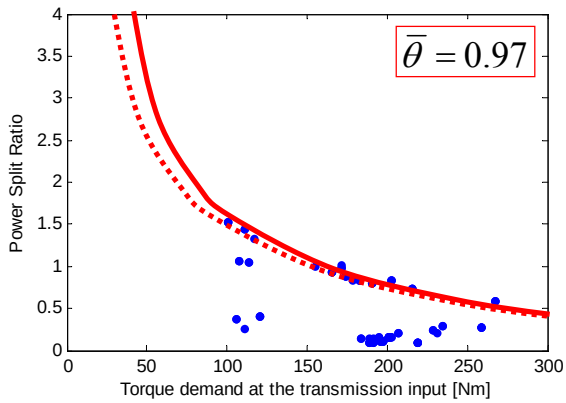

(d) $\bar{\theta} = 0.97$

Figure 4.20: Extracted cold-start power-split strategies at four sample $\bar{\theta}$ values

4.5 Design of Adaptive Cold-start Supervisory Powertrain Controller

Since all the extracted results for the PHEV were described in the same state space as those for the HEV, the basis structure and rules of the HEV SPC algorithm developed in Chapter 3 can be directly used here for control of the PHEV. The design and evaluation of the cold-start SPC for the PHEV are carried out as follows. For the hot SPC, two adaptive SPCs (instantaneous and DP-based) will be developed and compared with DP and the Electric Vehicle/Charge Sustaining (EV/CS) strategy under various $\bar{\theta}$ conditions. Then, two cold SPCs (Map-based and DP-based) are developed for proper catalyst temperature management and emission reduction. These cold SPCs are compared with DP results to benchmark their performance.

4.5.1 Hot SPC algorithm

4.5.1.1 Adaptive instantaneous optimal controller (IOC)

Using the EDR, $\bar{\theta}$, and the concept of adaptive control of the charge depletion rate, an adaptive instantaneous optimal control problem can be formulated as follows:

$$\text{Minimize } J = Fuel_{rate}(x,u,d) + p(\bar{\theta})I_{batt}(x,u,d) \tag{4.11}$$

where x is the state vector (V, SOC), u is the control input vector (Gr, T_{eng}), and d is the disturbance input (P_{wheel}). Note that the Lagrange multiplier, p, controls the charge depletion rate and should be adjusted depending on $\bar{\theta}$. The optimal control policy (u^*) and $p(\bar{\theta})$ were generated by the following process.

a) Compute two instantaneous cost matrices ($Fuel_{rate}(x,u,d)$ and $I_{batt}(x,u,d)$) for all x, u, and d space using the PHEV model.
b) Choose $\bar{\theta}$, and compute the corresponding SOC for the given travel distance.
c) Choose p, and compute the cost matrix $J(x,u,d)$.
d) Find the optimal control policy, $u^*(x,d)$, that minimizes J.
e) Simulate the PHEV model on a drive cycle (LA92) using u^* computed, and check for $SOC_{final} = SOC_{min}$. If not, adjust p, and repeat steps c) – e) the equality condition is met.
f) Repeat steps b) – e) as necessary for other $\bar{\theta}$ values.

Figure 4.21 shows the function $p(\bar{\theta})$ obtained from the above process for the target vehicle of this study.

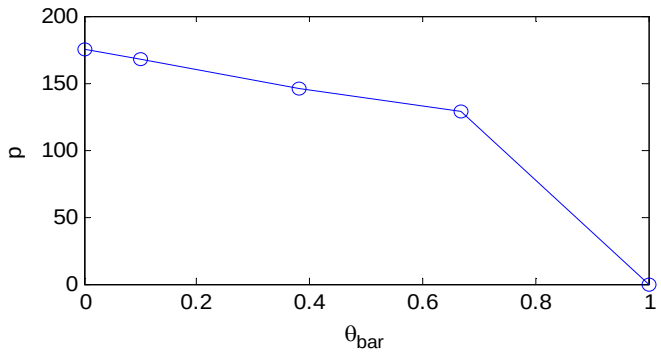

Figure 4.21: Lagrange multiplier p as a function of $\bar{\theta}$ for the LA-92 cycle

4.5.1.2 Adaptive DP-based Hot SPC

Based on the extracted hot results, the logic of the adaptive hot SPC algorithm is proposed as follows.

If $P_{dem}<P_{on/off}(\bar{\theta})$,
  Turn off the engine and select the gear using the Electric Vehicle (EV) shift-map
  $P_{m/g} = P_{dem}$
  If V<60mph, then disengage the clutch for engine disconnect
  Else, engage the clutch.
Else,
  Turn on the engine
  Select the gear using the engine-on mode shift-map $(\bar{\theta})$ *and find* T_{dem} *and* N_i
  Find PSR from T_{dem} *and* N_i *and compute* $P_{eng} = PSR \cdot P_{dem}$
  Compute M/G power: $P_{m/g} = P_{dem} - P_{eng}$
End

The flow chart of the adaptive DP-based SPC algorithm is illustrated in Figure 4.22 to help visualize the logic. Note that $P_{on/off}$ and shift-map are functions of $\bar{\theta}$, and they are obtained from the DP results, as shown in Figure 4.15 and 16. Other non-adaptive design parameters, *PSR* map and EV shift-map, are obtained from Figure 4.17 and 18 respectively.

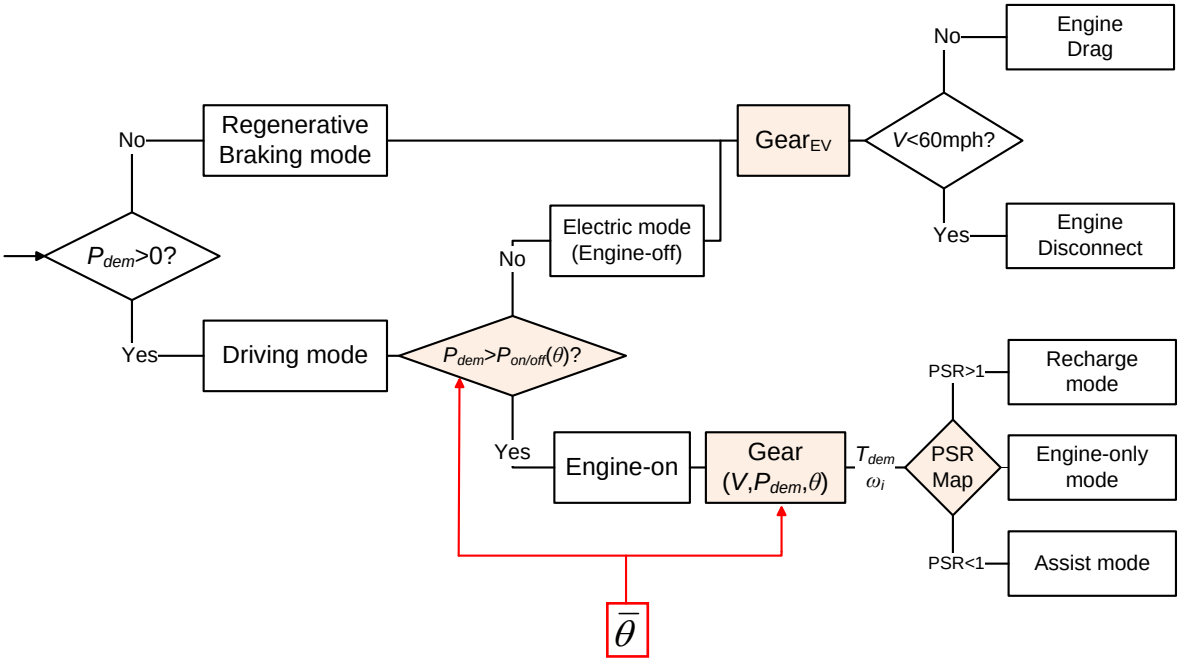

Figure 4.22: Flowchart of the adaptive DP-based Hot SPC

In this algorithm, the engine on/off power, gear shifting map, and *PSR* commands are sequentially determined because the *PSR* decision requires T_{dem} and ω_i, which can only be determined after gear selection is made, and the shift-map selection depends on the engine on/off decision. Embedding DP information in this rule-based control structure provides decoupled control logics of three sub-control modules: engine on/off, shift, and *PSR*, and is expected to perform near optimally.

4.5.2 Cold SPC algorithm

As discussed in section 4.4.2.2, the cold DP results of PHEVs are analogous to those of HEVs except for the engine on/off algorithm. Thus, both DP-based and Map-based Cold SPCs developed in Chapter 3 are directly applied to the PHEV using the PHEV extraction results: engine on/off, gear-shift, and *PSR* strategies (shown in Figure 4.13-4.20). For the cold-start engine on/off algorithm, a power threshold condition is added to the input speed condition.

4.6 Results and Discussion

In this section, hot-start and cold-start performances of the DP-based SPC are compared with those of DP and instantaneous approaches as shown below.

Table 4.4: Controller performance comparison chart

	Controllers			
Hot-start	DP	Adaptive IOC	DP-based SPC	EV/CS
Cold-start	DP	Map-based SPC	DP-based SPC	--------

4.6.1 Hot SPC algorithm – Fuel economy

The adaptive DP-based SPC is implemented and simulated to evaluate its hot-start fuel economy performance. Its results are compared with DP, adaptive instantaneous optimal controller (IOC), and EV/CS. Figure 4.23 shows that the adaptive DP-based Hot SPC is

successfully extracted from DP results, and its control signals (engine on/off, gear, and *PSR*) closely follow those of DP under various EDR conditions.

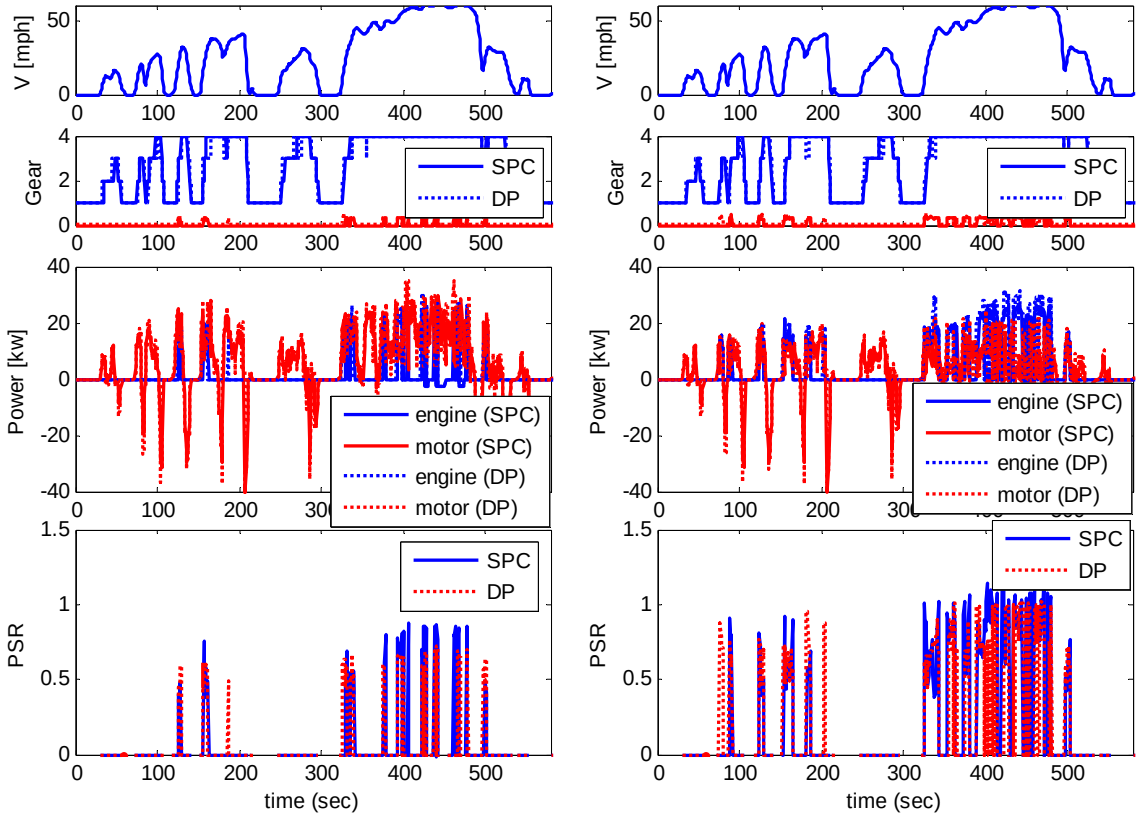

(a) $\bar{\theta} = 0.667$ (b) $\bar{\theta} = 0.381$

Figure 4.23: Simulation response comparison of DP vs. DP-based SPC for $\bar{\theta} = 0.667$ and $\bar{\theta} = 0.381$ on the hot-start LA92 cycle.

The fuel economy results of DP, IOC, DP-based Hot SPC, and EV/CS are summarized and compared with one another in Figure 4.24. The plot indicates that the adaptive DP-based SPC achieves near-optimal fuel economy for all $\bar{\theta}$ conditions owing to the adaptive control structure, and it performs much better than EV/CS strategy. The fuel economy improvement over the EV/CS increases with higher $\bar{\theta}$ and is expected to increase as $\bar{\theta}$ approaches 1. However, the DP-based SPC did not perform as good as the IOC. In fact, the IOC even outperforms DP, but at the expense of very large number of shift events. This is mainly due to the impact of engine on/off and shift event penalties on the fuel consumption of DP. When $\bar{\theta}$ is high, the vehicle mainly

operates in EV mode, and performance of EV mode primarily depends on engine on/off and gear-shift strategies. Table 4.5 shows that the engine-on and gear-shift counts of the IOC are extremely high, and an additional algorithm and/or calibration will be required to resolve these drivability issues at the expense of fuel economy.

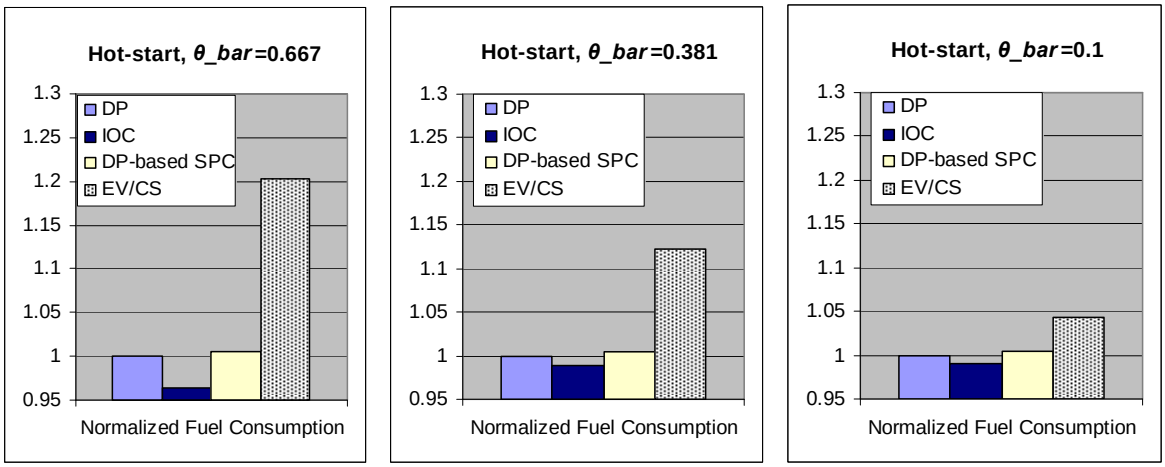

Figure 4.24: Fuel consumption comparison of DP, IOC, DP-based SPC, and EV/CS for various $\bar{\theta}$ on the hot-start LA92 cycle.

On the contrary, three control decisions (engine on/off, gear-shift, and power-split) of the DP-based SPC are sequentially determined, and individual control module can be separately modified without a significant loss of optimality for practical issues (e.g. drivability). For instance, if a late shift is desired for improved drivability, a calibrator can modify only the shift-map without any modification of the optimal *PSR* line or engine on/off strategy. However, this is difficult for the IOC to achieve because these control decisions are coupled with each other. Thus, the strengths of the DP-based SPC over the IOC include are 1) simple and intuitive control logic, 2) modular controller design, and 3) adjustability of individual control module.

Table 4.5: Comparison of DP, IOC, DP-based SPC, and EV/CS simulation results for $\bar{\theta} = 0.667$ and $\bar{\theta} = 0.381$ on the hot-start LA92 cycle.

	$\bar{\theta} = 0.667$				$\bar{\theta} = 0.381$			
Controller	DP	IOC	DP-based SPC	EV/CS	DP	IOC	DP-based SPC	EV/CS
MPG [unadjusted hotstart]	146.92	146.9	141.1	117.6	67.17	67.86	66.90	59.65
Fuel Cons. (g)	556.7 (0%)	557.1 (-4.5%)	580.8 (+4.3%)	694.6 (+24.8%)	1196 (0%)	1206 (-1.1%)	1225 (+2.4%)	1369 (+14.5%)
Engine-on count	135	175	116	68	162	232	142	110
Shift count	394	1043	352	376	384	939	348	382

4.6.2 Cold SPC algorithm – Fuel economy and emissions

For a fair comparison of the DP-based vs. Map-based Cold SPC, both controllers share the adaptive DP-based Hot SPC so that the control strategy is different only during the cold transient. First, the DP-based Cold SPC is implemented, and its simulation responses are compared with DP solution. Figure 4.25 shows that for $\bar{\theta} = 0.381$ the control signals and vehicle states of the DP-based SPC are very similar to those of DP, but for $\bar{\theta} = 0.667$ the first engine-on timing of DP-based Cold SPC occurs earlier than DP, resulting increased tail-pipe HC.

Despite some discrepancy in the engine on/off control strategies between DP-based SPC and DP simulation results, Figure 4.26 indicates that the DP-based SPC achieves near-optimal performance and outperforms the Map-based SPC under all $\bar{\theta}$ conditions. The cost function of the DP problem is used to evaluate combined fuel economy and emissions performance. Table 4.6 shows that a loss of the optimal emission performance is more apparent than that of the optimal fuel economy. In addition, the loss of optimality increases with higher $\bar{\theta}$ mainly due to increased EV operation. Table 4.6 shows that another factor for the reduced performance of the DP-based SPC is the drivability. Two rule-based SPCs result in much reduced number of engine on/off and gear-shift events, which trades off with the fuel economy and emissions.

In summary, the cold-start DP-based SPC consistently outperforms the Map-based SPC and achieves near-optimal fuel economy and emission performance despite some loss of optimality during the cold-start transient.

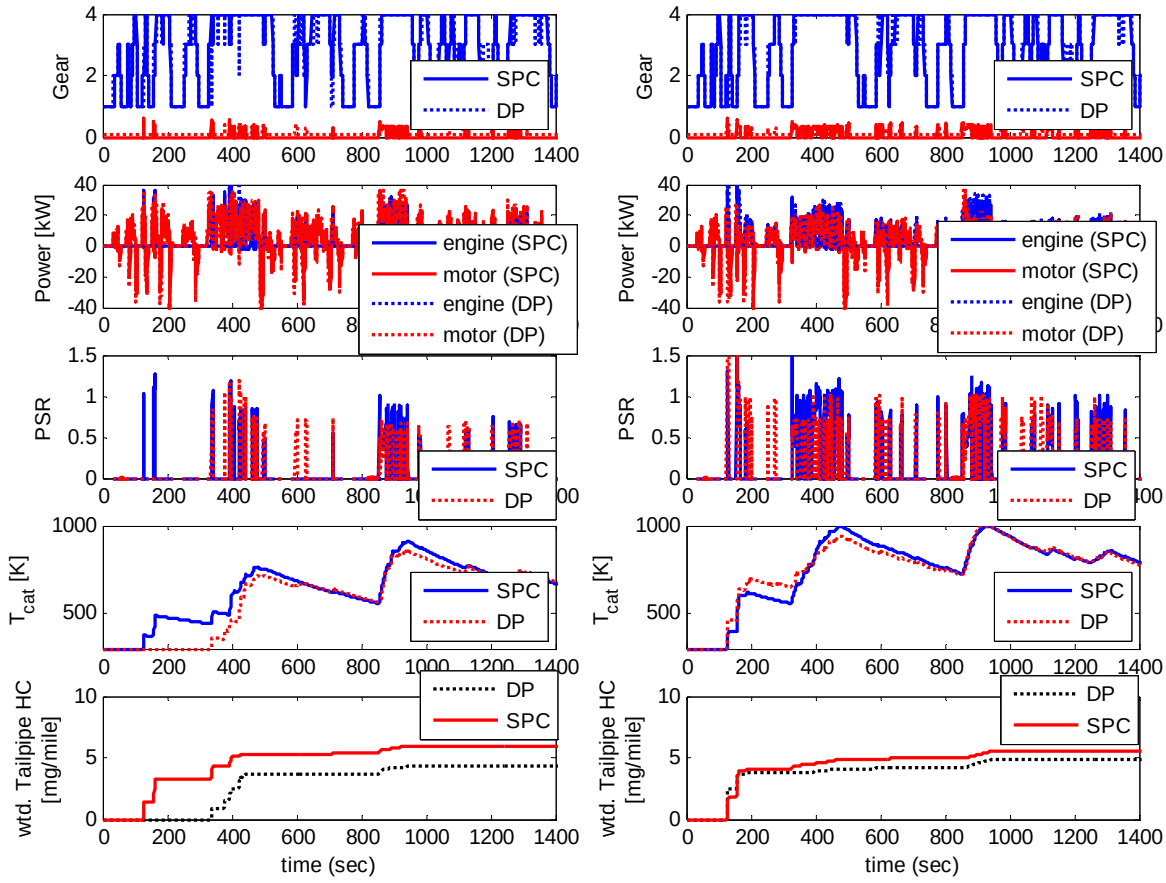

(a) $\bar{\theta} = 0.667$ (b) $\bar{\theta} = 0.381$

Figure 4.25: Simulation response comparison of DP and DP-based Cold SPC for $\bar{\theta} = 0.667$ and $\bar{\theta} = 0.381$ on the cold-start LA92 cycle.

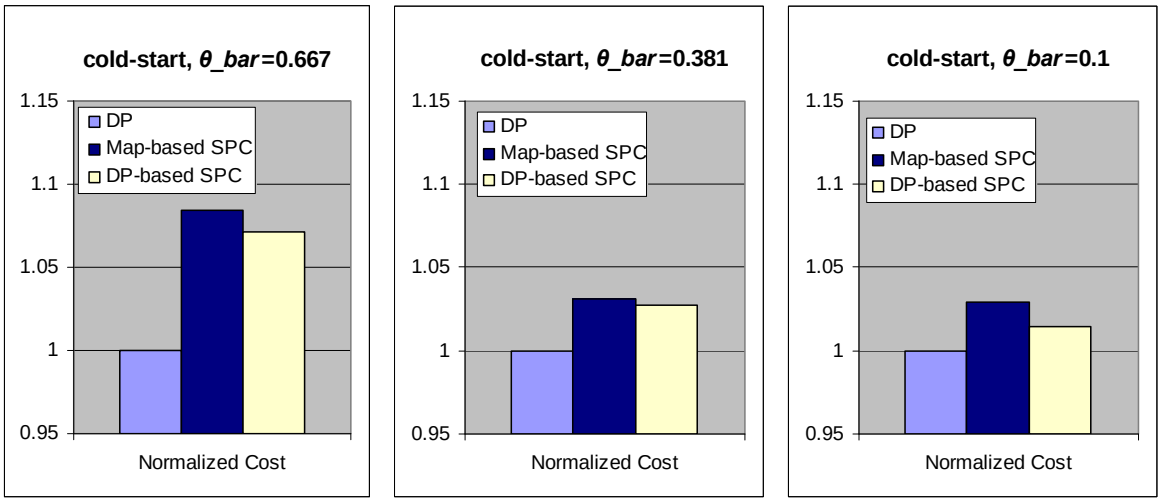

Figure 4.26: FC and HC combined performance comparison of DP, Map-based SPC, and DP-based for various $\bar{\theta}$ on the cold-start LA92 cycle.
Cost function: $J = \mathrm{FC}(g) + 500\mathrm{HC}(g)$

Table 4.6: Comparison of DP, DP-based, and Map-based Cold SPC simulation results for $\bar{\theta} = 0.667$ and $\bar{\theta} = 0.381$ on the cold-start LA92 cycle

	$\bar{\theta} = 0.667$			$\bar{\theta} = 0.381$		
Controller	DP	DP-based SPC	Map-based SPC	DP	DP-based SPC	Map-based SPC
MPG [unadjusted, cold-start]	142.0	138.6	137.6	67.38	66.45	66.40
Fuel Cons. (g)	576.1 (0%)	591.0 (+2.6%)	595.4 (+3.4%)	1215 (0%)	1233 (+1.5%)	1234 (+1.6%)
HC (mg/mile)	7.09 (0%)	9.33 (+31.6%)	9.62 (+35.7%)	8.22 (0%)	9.48 (+15.3%)	9.72 (+18.2%)
Performance Measure (g) *J=FC*+500 *HC*	682.5 (0%)	731.0 (+7.1%)	739.7 (+8.4%)	1338 (0%)	1375 (+2.8%)	1380 (+3.1%)
Engine-on count	137	118	115	202	142	141
Shift count	454	358	376	446	350	350

CHAPTER 5
OPTIMAL CONTROL OF ENGINE-START FOR DRIVABILITY

As of 2010, power-split hybrids have dominated the hybrid vehicle market, mainly because of their superior performance. The pre-transmission parallel hybrid electric vehicle (HEV) with a single motor is a cost-effective design, closer to the traditional powertrain, and thus can be implemented with fewer and less significant design changes. This configuration, however, has a challenging drivability issue during engine-starts because the motor must simultaneously provide the driving torque and start the engine using an engine-disconnect clutch. In this chapter, we first develop a control-oriented HEV powertrain model to accurately predict the engine, clutch, and vehicle dynamics during the engine-start process. Then, assuming that the clutch torque can be accurately estimated and perfectly cancelled, the optimal engine-start control problem is formulated and solved by analytical and numerical methods to minimize engine-start time while accurately supplying the driver torque demand.

5.1 Powertrain Model for Engine-start Control

The target vehicle is a pre-transmission parallel HEV with an engine-disconnect clutch (Figure 5.1). This configuration offers a cost-effective design while providing a full electric vehicle (EV) mode for a significant fuel economy improvement. Vehicle parameters of the target HEV are listed in Table 2.1 except for the motor and battery sizes are increased from 20kw to 30kw to provide substantial electric propulsion power. This arrangement, however, introduces the clutch-controlled engine-start problem, and a control-oriented powertrain model is developed in this section in order to accurately evaluate drivability performance.

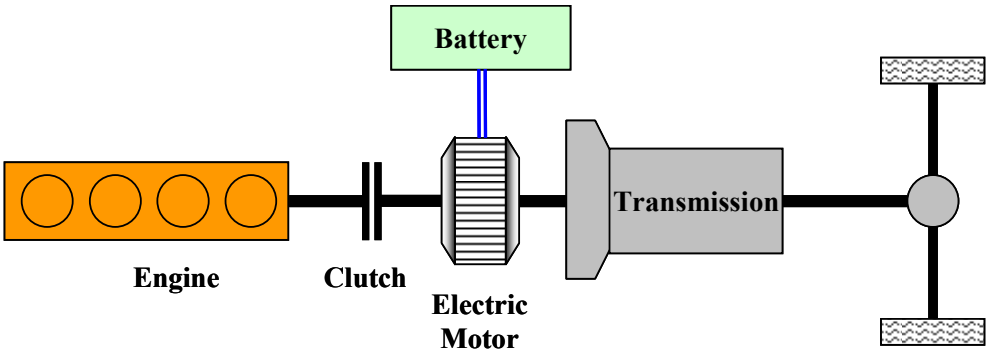

Figure 5.1: Schematic of a pre-transmission parallel HEV powertrain

5.1.1 Overview of the model

Figure 5.2 illustrates a simplified free-body diagram of the HEV powertrain. In this diagram, we assume that the gear is fixed and the clutch is slipping. Note that the dynamics of the engine and vehicle inertias are controlled by the clutch torque (T_{clutch}) and motor torque ($T_{M/G}$). The motor torque can be controlled relatively fast and accurately, but the clutch torque is determined by the clutch pressure, which has a significant delay due to the hydraulic actuator dynamics. T_{eng} is the compression (or firing) engine torque applied at the crank shaft, and T_{loss} is the total torque losses due to road load and driveline losses. The control objective is to quickly accelerate the engine speed (ω_e) to match the transmission input speed (ω_i) using a coordinated control of T_{clutch} and $T_{M/G}$ while avoiding any torque disturbance transferred through the clutch to the vehicle body.

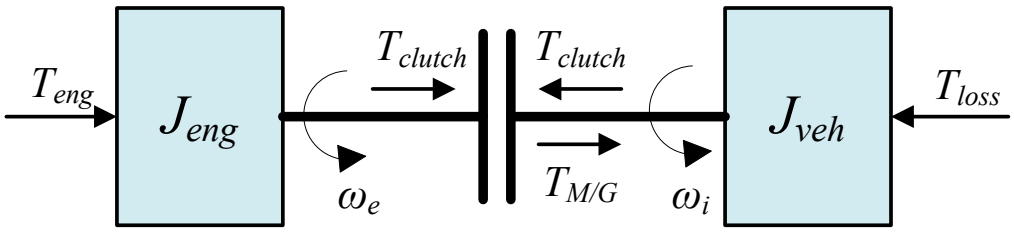

Figure 5.2: Simplified free-body diagram of the HEV powertrain.

A Simulink HEV model is developed based on the above free-body diagram. Figure 5.3 illustrates a block diagram of the vehicle model. The model consists of three sub-models, vehicle dynamics, engine dynamics, and clutch model. The clutch model takes the slip speed ($\Delta\omega=\omega_i-\omega_e$)

and clutch pressure as inputs and computes the clutch torque. Then, the engine and vehicle dynamics are determined by the clutch torque and motor torque.

In the state space representation, the vehicle model is described as follows.

$$\dot{x} = f(x,u) \tag{5.1}$$

where x is the state vector with four state variables ω_i, ω_e, θ_{crank}, and intake manifold pressure (MAP). u is the control input vector with four variable, clutch pressure (P_{clutch}), motor torque ($T_{M/G}$), and firing command ($firing$). T_{loss} is not an input because it is internally computed. We assume that the second gear is selected and fixed during the engine-start process.

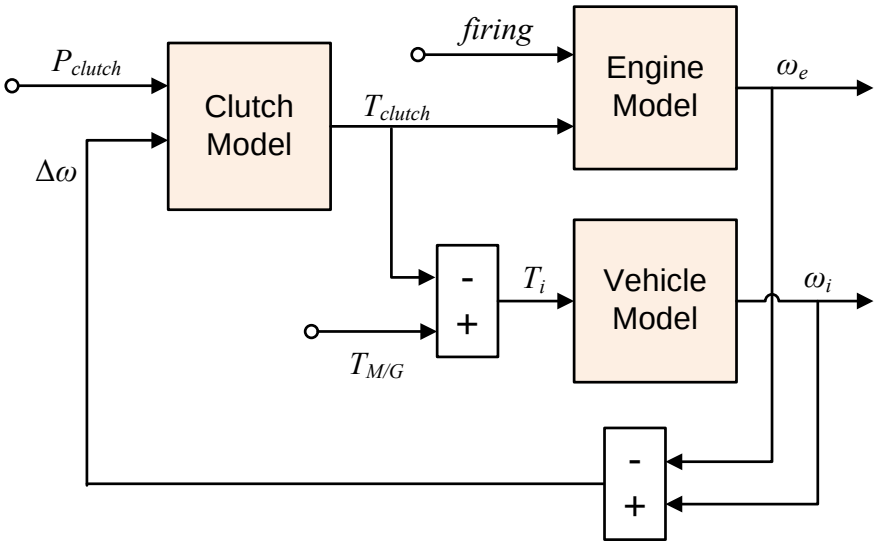

Figure 5.3: Block diagram of the vehicle model for engine-start control.

5.1.2 Clutch model

The clutch is a difficult component to model due to its discontinuous nature. An accurate and reliable clutch model can be found from the Simulink library Simscape/SimDriveline. This model was developed based on the Coulomb friction model, which uses both static and dynamic friction coefficients depending on the slip speed ($\Delta\omega$). Let us define the friction coefficient (μ) as:

$$\mu = \frac{T_{clutch}}{N\, r_e F_{app}} \tag{5.2}$$

where F_{app} is the applied normal force, r_e is the equivalent radius, and N is the number of clutch plates. Under the assumption that the effects of temperature and F_{app} on μ are small, the slip speed ($\Delta\omega$) dominates μ function in normal operations, and T_{clutch} can be computed as

$$\begin{aligned} T_{clutch} &= N r_e \mu(\Delta\omega) F_{app} \\ &= N r_e \mu(\Delta\omega) A_{eff} P_{clutch} \\ &= K_c \mu(\Delta\omega) P_{clutch} \end{aligned} \tag{5.3}$$

where A_{eff} is the effective area of the clutch, and P_{clutch} is the applied clutch pressure. Now, the challenge in modeling the clutch is to know how to model $\mu(\Delta\omega)$. One of the simpler and widely used friction models is shown in Figure 5.4. This function switches between two states; 'slip' and 'stick'.

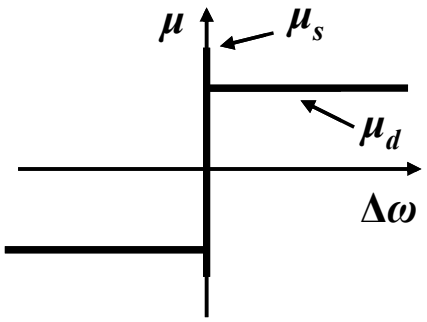

Figure 5.4: Friction coefficient (μ) as a function of the slip speed ($\Delta\omega$).

When the slip speed is non-zero, the clutch model is in the slip state, and the clutch torque is determined by the dynamic friction coefficient (μ_d) and clutch pressure. When the slip speed is zero, the clutch model is in stick state, and the clutch capacity (T_{cap}) is limited by

$$T_{cap} = K_c \mu_s P_{clutch} \tag{5.4}$$

where μ_s is the static friction coefficient. Note that the actual clutch torque can be equal to or lower than the clutch capacity during the stick state. The governing equations of the simplified free-body diagram using this model are as follows.

$$\text{when slipping } \begin{cases} J_{eng}\dot{\omega}_e = T_{eng} + T_{clutch} \\ J_{veh}\dot{\omega}_i = T_{M/G} - T_{clutch} - T_{loss} \end{cases} \tag{5.5}$$

$$\text{when sticking } \begin{cases} (J_{eng} + J_{veh})\dot{\omega}_e = T_{M/G} + T_{eng} - T_{loss} \\ \omega_e = \omega_i \end{cases} \tag{5.6}$$

Although the above Simulink model offers reliable simulation results using a sophisticated state transition algorithm, it can not handle vector or matrix signals, which allow multiple simulations in a single model-call for significant computation time reduction. Thus, the hyper-tangent function of μ in Figure 5.5 will be used for DP computations. Note that the function is now continuous and crosses zero for reliable simulations without complexity of a state transition algorithm. For the optimal control problem, we assume fast actuator servo-loop dynamics and focus on identifying the optimal clutch pressure, $P_{clutch}^{*}(t)$. The actuator delay, however, will be considered for implementation of the optimal solutions.

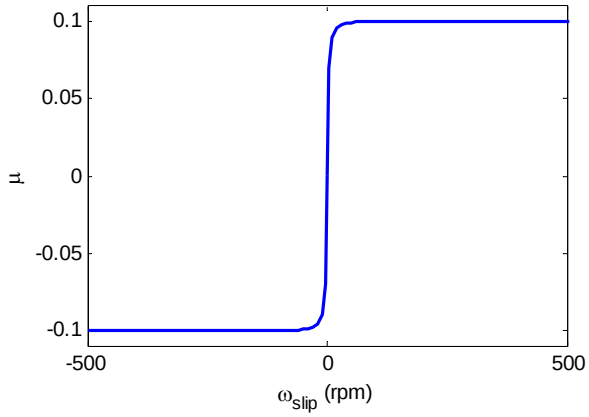

Figure 5.5: Approximated friction coefficient (μ) as a function of the slip speed ($\Delta\omega$).

5.1.3 Engine model

The engine model for the engine-start control study needs to be very accurate because the compression and firing torque of the engine are the main sources of torque disturbance. A detailed engine model developed by General Motors in C^{++} is used in this study. This model was converted into a Simulink model because handling the matrix initial conditions is convenient in the Matlab/Simulink environment for DP computations. Due to confidentiality, the engine model is not discussed in detail. The scope and basic ideas of this model, however, are described below.

The engine model consists of three parts, intake manifold dynamics, compression/firing torque, and inertial dynamics. This entails three dynamic states; crank angle (θ_{crank}), engine speed (ω_e), and intake manifold pressure (MAP). Figure 5.6 shows a block diagram describing the intake manifold dynamics and compression/firing torque model.

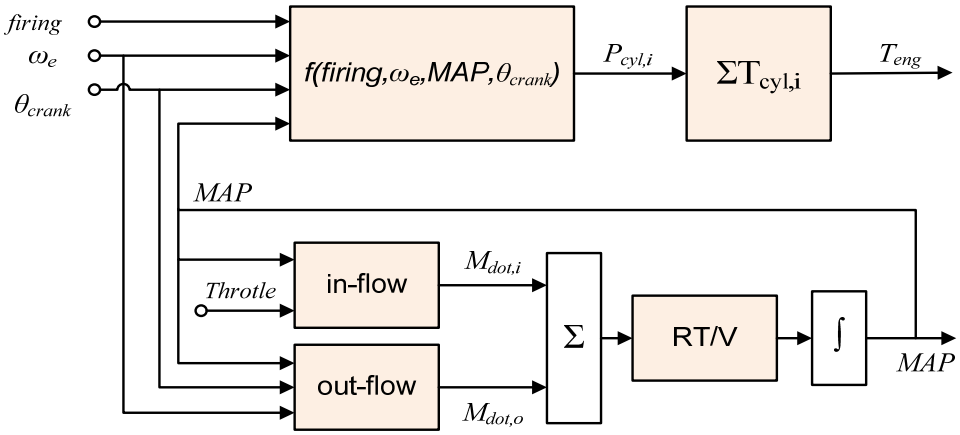

Figure 5.6: Overview of the engine model.

5.1.3.1 Intake manifold dynamics

The intake manifold pressure dynamics are described by the mass conservation law and the ideal gas law. Figure 5.6 shows that the inlet and outlet air-flow rates are computed to find the MAP rate. The inlet air-flow rate is computed as

$$\dot{M}_i = \begin{cases} A_{throt}\dfrac{P_{atm}}{(RT)^{0.5}}\left(\dfrac{MAP}{P_{atm}}\right)^{0.714}\left(7\left(1-\left(\dfrac{MAP}{P_{atm}}\right)^{0.286}\right)\right)^{0.5} & \text{, for } MAP \le P_{atm} \\ -A_{throt}\dfrac{P_{atm}}{(RT)^{0.5}}\left(\dfrac{MAP}{P_{atm}}\right)^{-0.714}\left(7\left(1-\left(\dfrac{MAP}{P_{atm}}\right)^{-0.286}\right)\right)^{0.5} & \text{, for } MAP > P_{atm} \end{cases} \tag{5.7}$$

where A_{throt} is the throttle area, and the throttle is assumed to be fixed at idle during the engine-start process. The outlet air-flow rate is the summation of air-flow rates into cylinders with open intake valves. That is,

$$\dot{M}_o = \sum_i \dot{m}_{cyl,i} \text{ where } \dot{m}_{cyl,i} = \begin{cases} \dfrac{\omega_e r_{eff,i} A_{pist} MAP}{RT} & \text{, during intake phase} \\ 0 & \text{, otherwise} \end{cases} \tag{5.8}$$

where $r_{eff,i}$ is the effective crank radius of cylinder i, A_{pist} is the piston top area, R is the gas constant, and T is the ambient temperature.

5.1.3.2 Compression/firing torque

When the engine is warm, the compression/firing torque can be accurately computed by the crank-angle domain cylinder pressure map, which is a function of crank angle (θ_{crank}), engine speed (ω_e), *MAP*, and firing command (*firing*). Figure 5.7 shows two sample pressure maps of the compression mode at 200rpm and firing mode at 1000rpm. However, this map-based pressure model is inappropriate for the very first cycle because initially all cylinder pressures start at the atmospheric pressure regardless of the crank angle. This introduces significant complexity to the compression torque model, and each cylinder undergoes different pressure trajectories depending on individual initial crank angle.

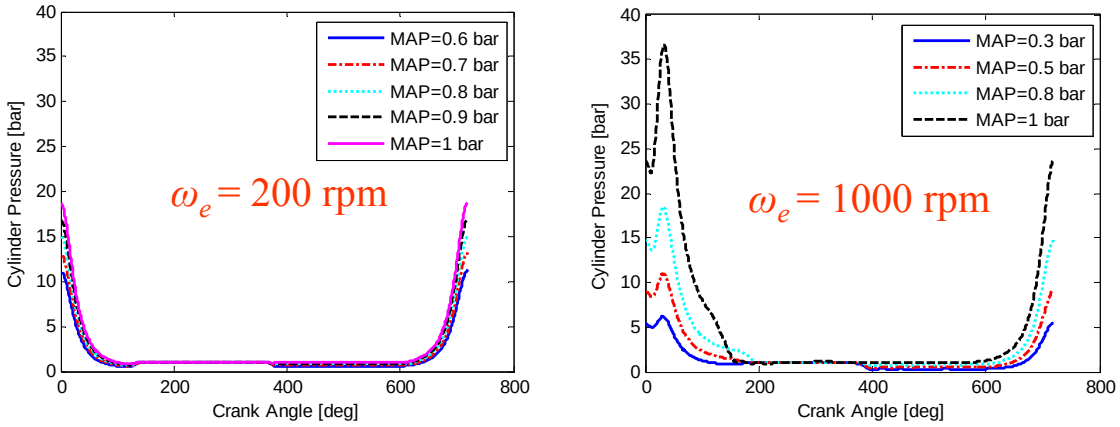

Figure 5.7: Sample pressure maps of compression mode (200rpm) and firing mode (1000rpm).

In addition, we need to pay special attention to the transition from compression to firing mode because this transition cannot occur during the combustion and expansion phases. In other words, the transition can only occur after the exhaust phase starts and before the compression phase ends, otherwise, the pressure response will be discontinuous. Note that this transition model requires an extra state, a memory of the last state, and is thus neglected for DP computations.

5.1.3.3 Compression/firing torque

The rotational dynamics of the engine inertia is described as follows.

$$\dot{\omega}_e = \frac{T_{eng} - T_{clutch} - T_{loss} + T_{eq,piston}}{J_{eng} + J_{eq,piston}} \tag{5.9}$$

where T_{eng} is the compression/firing torque, T_{clutch} is the clutch torque, T_{loss} is the engine friction loss, J_{eng} is the rotational engine inertia, and $T_{eq,piston}$ and $J_{eq,piston}$ are piston equivalent torque and rotational inertia, respectively. Note that $T_{eq,piston}$ and $J_{eq,piston}$ are necessary to reflect the torque and rotational inertia induced by the piston, which are not negligibly small and functions of the engine rotational angle.

5.1.4 Vehicle model

Since we do not consider high frequency NVH in this study, the quasi-static driveline and point mass vehicle inertial models developed in section 2.2.2.4 and 2.2.2.5 are used and summarized below.

$$T_{wheel} = \eta_{GR}\eta_{FD} GR \cdot FD \cdot T_i - C_{TM}\omega_i \tag{5.10}$$

$$\omega_i = GR \cdot FD \cdot \omega_{wheel} \tag{5.11}$$

$$\dot{V} = \frac{T_{wheel} R_{tire} - F_{brake} - F_{road}}{M_r} \tag{5.12}$$

$$F_{road} = f_0 + f_1 V + f_2 V^2 \tag{5.13}$$

5.1.5 Parameter estimation and model validation

Due to the lack of experimental data, engine parameters are obtained from the GM model, clutch parameters are estimated based on the literature, and other vehicle parameters are shared with the supervisory control vehicle model. Thus, the model validation focuses on the engine model, and the Simulink model developed in the previous section is validated by comparing it with the C++ based GM model. Figure 5.8 shows two simulation examples under two different control commands; both examples use final *MAP* = 0.3 bar, a clutch torque cancelling motor

controller (this will be discussed in the following section), and constant clutch pressure commands; one at 250kPa with initial fire at 0.3 sec and the other at 300kPa with initial fire at 0.25 sec. Both examples show that both engine torque (T_{eng}) and engine speed (ω_e) responses of the Simulink model are almost identical to those of GM model. After many more simulations, comparisons, and analyses under various inputs, it is concluded that the engine-start model accurately predicts the engine, clutch, and vehicle dynamics.

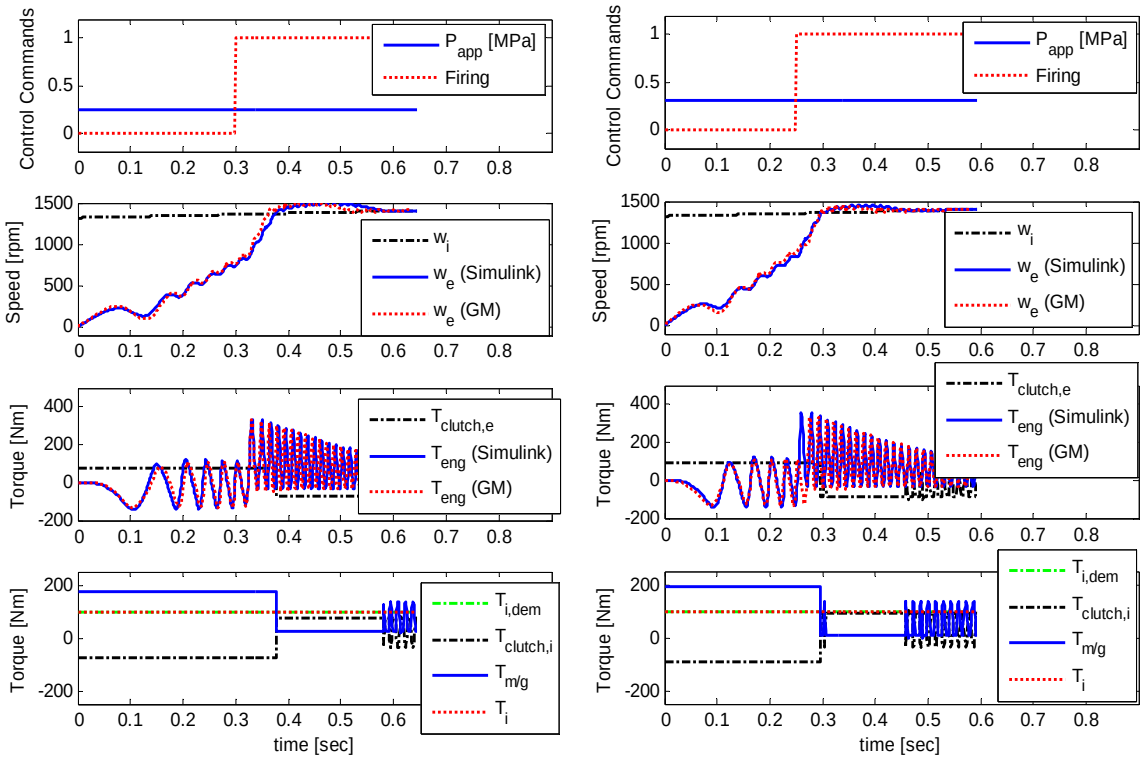

(a) P_{clutch} = 250 kPa (b) P_{clutch} = 300 kPa

Figure 5.8: Comparison of Simulink model and GM model under two different control commands (P_{clutch} = 250 kPa and 300 kPa).

5.2 Optimal Control of the Engine-start

The optimal control of the HEV engine-start is a constrained nonlinear optimization problem with free terminal time and partly free terminal state. In this section, two optimal control problems are formulated and solved using various optimization methods.

Let us first define the engine-start optimal control problem as follows. If we assume that the clutch torque can be accurately estimated and the motor torque dynamics are very fast, we can eliminate one of the control variables, $T_{M/G}$, by using a clutch torque cancellation motor controller,

$$T_{M/G,dem} = T_{i,dem} + T_{clutch} \tag{5.14}$$

where $T_{i,dem}$ is the demanded torque at the transmission input, and $T_{M/G,dem}$ is the demanded motor torque. Then, the torque disturbance transmitted through the clutch can be perfectly cancelled as long as the motor torque capacity permits. That is,

$$T_i = T_{M/G,dem} - T_{clutch} = T_{i,dem} \text{ if } T_{M/G,dem} \le T_{M/G,\max} \tag{5.15}$$

In addition, we can eliminate ω_i by assuming that the change in ω_i is small during the engine-start process (i.e. large vehicle inertia). The resulting simplified engine-start system is described as

$$\dot{x} = F(x,u) \tag{5.16}$$

where $x = \begin{bmatrix} \omega_e \\ \theta_{crank} \\ MAP \end{bmatrix}$, $u = \begin{bmatrix} P_{clutch} \\ firing \end{bmatrix}$, and $F(x,u) = \begin{bmatrix} f_1(x,u) \\ f_2(x,u) \\ f_3(x,u) \end{bmatrix}$. f_1, f_2, and f_3 are individual nonlinear system dynamics. Disturbance parameters are initial crank angle ($\theta_{crank,0}$) and driver demand ($T_{i,dem}$).

Now, the objective of the optimal control problem is to find $P_{clutch}(t)$ and $firing(t)$ that minimize the engine-start time while also minimizing the torque disturbance to the vehicle body. Since the final time is free and depends on the final state, we need to clearly define what the conditions are for terminating the control problem. Otherwise, we may end up with an undesirable final state; i.e. a final state with very high *MAP* is not ready for a clutch lock-up because the high engine torque ripples cannot be cancelled out by the motor torque. We define the final time (t_f) as the first time when the clutch is ready for lock-up. That is when two conditions, $|\omega_i(t_f) - \omega_e(t_f)| < 50$rpm (i.e. small slip is allowed before a clutch lock-up) and $MAP < MAP_{target}$ (target *MAP* ready for a clutch lock-up), are met for the first time. In a mathematical form, the cost function and the boundary conditions are described as follows.

Optimal Control Problem 1

$$\text{Minimize } J = t_f + \int_{t_0}^{t_f} \alpha (T_{i,dem} - T_i)^2 \, dt \tag{5.17}$$

$$\text{Subject to } \begin{aligned} &\omega_e(t_0) = 0, \qquad \left|\omega_e(t_f) - \omega_i(t_f)\right| \le 50 rpm \\ &\theta_{crank}(t_0) = 0, \qquad \text{free } \theta_{crank}(t_f) \\ &MAP(t_0) = 1 \,\text{bar}, \; MAP(t_f) \le MAP_{target} \\ &firing = 0 \text{ for } \omega_e \le \omega_{firing} \end{aligned} \tag{5.18}$$

The cost function consists of a final time and torque error penalty. In the constraints, the initial crank angle and *MAP* are assumed to be 0 deg and 1 bar respectively, the final speed condition allows some slipping, and the *MAP* condition ensures that the engine torque can be handled by the motor after the clutch lock-up.

On the other hand, a different optimal control problem can be formulated if the driver demand is treated as a constraint rather than a cost. Furthermore, some torque reserve may be desirable in order to meet a possible increase in driver torque demand during the engine-start process. As a result, the second optimal control problem is formulated as follows.

Optimal Control Problem 2

$$\text{Minimize } J = t_f \tag{5.19}$$

$$\text{Subject to } \begin{aligned} &T_i - T_{i,dem} = 0, \text{for all } t \\ &T_{M/G} \le T_{M/G,\max} - T_{reserve}, \text{for all } t \\ &\omega_e(t_0) = 0, \qquad \left|\omega_e(t_f) - \omega_i(t_f)\right| \le 50 rpm \\ &\theta_{crank}(t_0) = 0, \qquad \text{free } \theta_{crank}(t_f) \\ &MAP(t_0) = 1 \,\text{bar}, \; MAP(t_f) \le MAP_{target} \\ &firing = 0 \text{ for } \omega_e \le \omega_{firing} \end{aligned} \tag{5.20}$$

where the first constraint guarantees that the driver demand is always met, and the second constraint maintains a specified level of torque reserve.

Figure 5.9 shows a conceptual sketch of all optimal solutions that can be obtained by the above two optimal control problems. These optimal solutions are classified into four categories. The first category contains a unique solution that achieves the absolute minimum engine-start

time at the expense of significant propulsion torque loss. The second category is the trade-off (or disturbed) solution, which balances the engine-start time and torque disturbance. The third solution is another unique solution that achieves minimum time without any compromise in torque demand ($T_i = T_{i,dem}$) by using all available M/G torque. The last one is the torque reserve solution, which is the slowest solution and compromises the engine-start time in order to reserve a desired level of motor torque. Note that first two categories of solutions are obtained by solving the Optimal Control Problem 1, and the third and fourth by Optimal Control Problem 2.

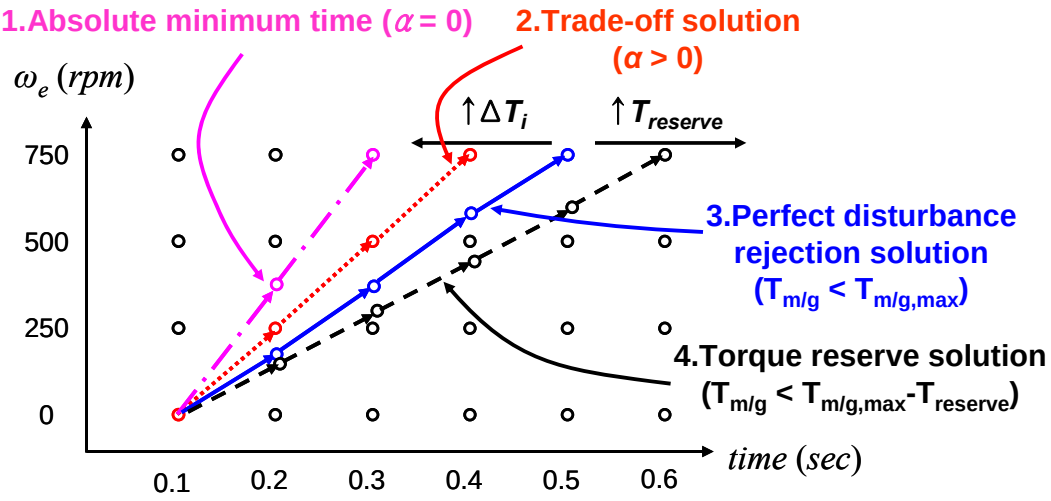

Figure 5.9: Conceptual sketch of various optimal solutions.

5.2.1 Variational approach

The optimal control theory based on the variational approach is applied to solve Optimal Control Problem 1 (5.13-14). First, we can define the Hamiltonian function as

$$H(x,u,P) = 1 + \alpha\left(T_{i,dem} - T_i(x,u)\right)^2 + P^T \cdot F(x,u) \tag{5.21}$$

where $P = \begin{bmatrix} p_1 \\ p_2 \\ p_3 \end{bmatrix}$ is the costate, also known as the Lagrange multiplier.

Then, the necessary conditions that minimize the augmented cost function $J_a = \int_{t_0}^{t_f} H(x,u,P)\,dt$ are as follows.

$$\dot{x}^* = \frac{\partial H}{\partial P} = F(x,u) \tag{5.22}$$

$$\dot{P} = -\left(\frac{\partial H}{\partial x}\right)^T = -\alpha\left(\frac{\partial\left(T_{i,dem} - T_i(x,u)\right)^2}{\partial x}\right)^T - \left(\frac{\partial F(x,u)}{\partial x}\right)^T P(t) \tag{5.23}$$

$$\frac{\partial H}{\partial u} = 0 \Rightarrow \alpha\frac{\partial\left(T_{i,dem} - T_i(x,u)\right)^2}{\partial u} + p_1(t)\frac{\partial f_1(x,u)}{\partial u} + p_2(t)\frac{\partial f_2(x,u)}{\partial u} + p_3(t)\frac{\partial f_3(x,u)}{\partial u} = 0 \tag{5.24}$$

Since the control input u is bounded and constrained, Pontryagin's Minimum Principle (PMP) can be used to replace (5.24) with

$$u^*(t) = \arg\min_{u(t)\in U} H(x,u,P) \tag{5.25}$$

The corresponding boundary conditions are the original initial and final state constraints plus the Hamiltonian condition at the final time, $H(t_f) = -1$, which is introduced by the free final time and its appearance in the cost function. Now, the optimal control problem is converted into a two-point boundary value problem with six ordinary differential equations and six boundary conditions including $H(t_f) = -1$. Unfortunately, the algebraic constraint (5.24) on the control input cannot be solved for useful insights or the analytical control law.

Despite its elegant mathematical formulation, variational approach does not guarantee the globally optimal solution because it is developed based on the first order calculus of variations. In addition, the above necessary conditions must be solved by iterative numerical methods to find a solution. Thus, we will use other approaches to find the optimal solutions and obtain useful insights.

5.2.2 Analytical approach via 'divide and conquer'

The objective of the analytical approach is to find the optimal solution in a closed form by reformulating (or reducing) the optimal control problem using engineering insights. Let us divide the optimal control problem into two smaller problems, engine-driven ($\Delta\omega>0$) and engine-driving ($\Delta\omega<0$) phase, because the direction of clutch torque changes with the sign of the slip speed.

5.2.2.1 Engine-driven ($\Delta\omega>0$) phase

During the engine-driven phase, we can simply solve for a solution that reaches $\Delta\omega=0$ as soon as possible because the cost function is a monotonic function of the clutch pressure; faster speed-up always leads to faster *MAP* drop as well as faster speed convergence.

Solution categories 1, 3, and 4 defined in Figure 5.9 can be obtained by the analytical approach. First of all, the absolute minimum time solution is trivial; apply maximum clutch pressure ($P_{clutch,max}$) and use available motor torque ($T_{M/G,max} - T_{i,dem}$) to reduce torque error as much as possible, which is defined as torque demand minus actual torque at the transmission input ($\Delta T_i = T_{i,dem} - T_i$).

For the perfect disturbance rejection and torque reserve solutions, the input torque is now fixed by the drivability constraint ($T_i = T_{i,dem}$), and the torque reserve constraint will always be active because the minimum time is achieved if and only if all of the available M/G torque is used to accelerate the engine ($T_{M/G,max}=T_{i,dem}$). Now, the optimal control problem is simply how to choose $P_{clutch}(t)$ that utilizes all of the available M/G torque ($T_{M/G,avail}$) without exceeding the limit.

The perfect disturbance rejection and torque reserve solutions are derived as follows. Let the clutch torque be equal to the available torque to minimize the engine-start time. That is,

$$T_{clutch}(t) \equiv T_{M/G,avail} = T_{M/G,\max}(t) - T_{i,dem}(t) - T_{reserve}(t) \tag{5.26}$$

By the clutch model, T_{clutch} is computed as

$$T_{clutch}(t) = C\mu\big(\Delta\omega(t)\big)P_{clutch}(t) \tag{5.27}$$

Combining (5.22) and (5.23) to find the optimal pressure command,

$$P_{clutch}{}^{*}(t) = \frac{T_{clutch}(t)}{C\mu\big(\omega_i(t) - \omega_e(t)\big)} \tag{5.28}$$

where $\omega_e(t)$ is described by the engine dynamics,

$$\frac{d\omega_e(t)}{dt} = f_1(\omega_e, \theta_e, MAP, T_{clutch}) \tag{5.29}$$

The required information to solve $P_{clutch}^{*}(t)$ are $T_{M/G,max}(t)$, $T_{i,dem}(t)$, $T_{reserve}(t)$, and initial ω_i (which can be calculated from vehicle speed and gear). A useful special case is that if we assume that $T_{M/G,max}(t)$, $T_{i,dem}(t)$, and $T_{reserve}(t)$ are constant during the engine-start, then $P_{clutch}^{*}(t)$ is only a function of $\Delta\omega(t)$. Furthermore, if we assume that $\mu(\Delta\omega)$ is constant almost everywhere, as Figure 5.4 and 5.5 show, the optimal pressure command $P_{clutch}^{*}(t)$ is constant almost everywhere (except when $\Delta\omega \approx 0$) regardless of the firing command. This is an important result because the constant pressure command is very easy to implement, and the resulting clutch torque is constant, which is also easy to cancel out.

$$T_{clutch}(t) \equiv T_{M/G,avail} = T_{M/G,\max}(t) - T_{i,dem}(t) - T_{reserve}(t) \tag{5.30}$$

The main decision of the firing command is the initial firing time. In theory, the initial firing should occur as soon as the engine speed reaches the minimum firing speed (ω_{firing}) because firing significantly helps faster engine speed-up and reduction of *MAP*.

5.2.2.2 Engine-driving ($\Delta\omega<0$) phase

The engine-driving phase problem is not as simple as the driven phase because the cost function is no longer a monotonic function of the clutch pressure. Two objectives, faster engine speed convergence and faster *MAP* reduction may conflict with each other. The engine speed overshoot is desirable for two reasons; 1) a slipping clutch allows for a smooth controllable clutch torque whereas the clutch lock-up leads to large firing torque ripples transmitted through the clutch, and 2) the overshoot leads to a faster *MAP* drop, but the engine speed eventually has to come back down before the clutch lock-up. Therefore, the optimal solution in a closed form can not be solved for the engine driving phase, but simple pressure commands, such as with constant or linear functions are good candidates for practically implementable optimal solution.

As an example, if we limit the clutch pressure command to a linear function, one can find an initial value and a slope of that linear function that meets two final state constraints on ω_e and *MAP* at a minimum engine-start time. Figure 5.10 shows two examples for a comparison; one

with a constant pressure and the other with a linearly increasing function starting at a lower pressure. Both examples share the optimal constant pressure command (perfect disturbance rejection with $T_{reserve}$ = 0Nm) for the engine-driven phase. Note that the first example with a simple constant clutch pressure command leads to small slipping condition during the engine-driving phase. On the other hand, the second example shows that the lower clutch pressure promotes overshoot initially, and then the increasing pressure brings the speed back down to the input speed before the target *MAP* (0.6 bar) is reached. This increased engine speed results in increased air-flow rate from the intake manifold, which leads to a slightly faster engine-start time.

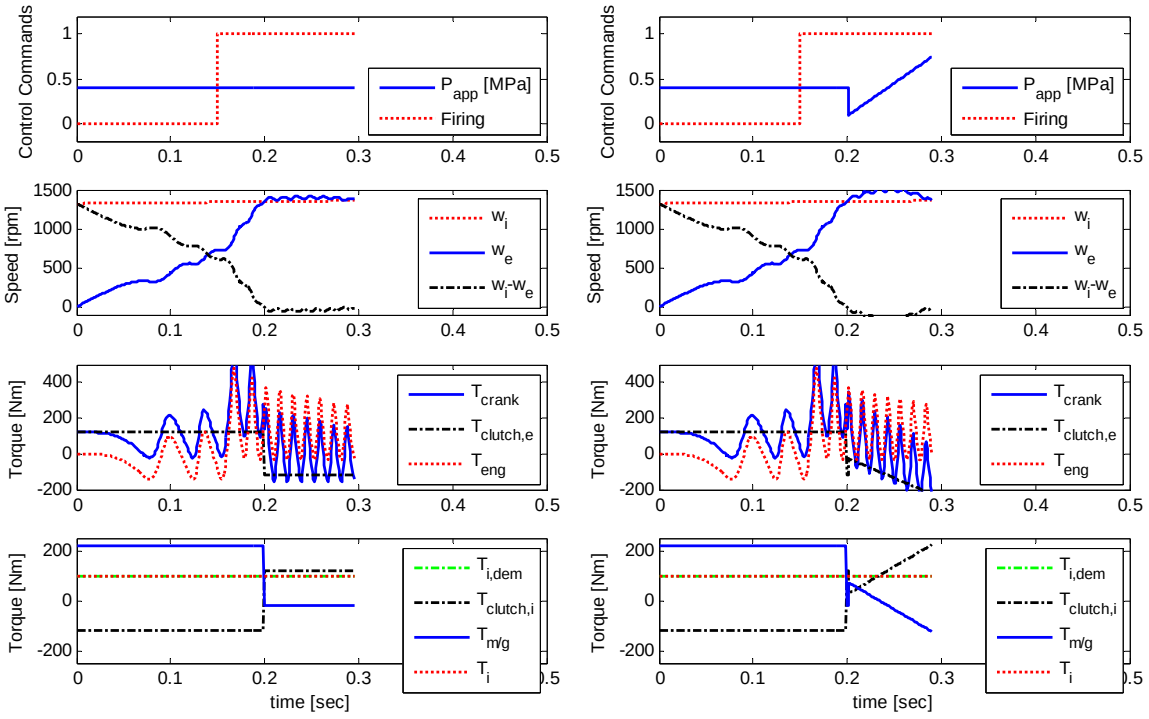

Figure 5.10: Simulation results of two sample analytical optimal solutions ($T_{reserve}$ = 0Nm).

5.2.3 Numerical approach via Dynamic Programming

DP is a very powerful optimization tool for solving a wide range of optimal control problems including nonlinear non-convex constrained problems. For numerical implementation of DP in the Matlab/Simulink environment, the two original optimal control problems are discretized and modified as follows.

Optimal Control Problem 1

$$\text{Minimize } J=\sum_{k=0}^{N}\begin{pmatrix}1(x\neq x_{final})+\alpha\left(T_{i,dem}-T_{i,k}\right)^2\\+\beta {T_{M/G,k}}^2+\gamma\left(P_k-P_{k+1}\right)^2\end{pmatrix} \tag{5.31}$$

$$\text{Subject to } \begin{aligned}&\omega_{e,0}=0, && \left|\omega_{e,N}-\omega_{i,N}-50\right|\le 25rpm\\&\theta_{crank,0}=0, && \text{free } \theta_{crank,N}\\&MAP_0=1\,\text{bar}, && MAP_N\le MAP_{target}\\&firing=0 \text{ for } \omega_e\le\omega_{firing}\end{aligned} \tag{5.32}$$

Optimal Control Problem 2

$$\text{Minimize } J=\sum_{k=0}^{N}1(x\neq x_{final})+\beta {T_{M/G,k}}^2+\gamma\left(P_k-P_{k+1}\right)^2 \tag{5.33}$$

$$\text{Subject to } \begin{aligned}&T_i-T_{i,dem}=0, \text{for all } t\\&T_{M/G}\le T_{M/G,\max}-T_{reserve}, \text{for all } t\\&\omega_{e,0}=0, && \left|\omega_{e,N}-\omega_{i,N}-50\right|\le 25rpm\\&\theta_{crank,0}=0, && \text{free } \theta_{crank,N}\\&MAP_0=1\,\text{bar}, && MAP_N\le MAP_{target}\\&firing=0 \text{ for } \omega_e\le\omega_{firing}\end{aligned} \tag{5.34}$$

The design variables are α, β, γ, and $T_{reserve}$, where β and γ are the motor torque and clutch pressure change penalty coefficients, respectively. The motor torque penalty tries to keep its magnitude down, and pressure change penalty reduces changes in clutch pressure commands. These penalties are necessary, and their coefficients must be adjusted to obtain practical solutions. The main challenge in implementing the DP algorithm for these optimal control problems is that this is a minimum time problem. Time penalties of (5.17) and (5.19) are implemented by penalizing the cost matrix by 1 at each time step, except for states that meet the final state criteria. Note that the final engine speed condition is modified to promote small negative slip, which reduces numerical issues that arise when $\Delta\omega\approx 0$ due to the hyper-tangent clutch model (Figure 5.5) used for DP purposes.

Table 5.1 summarizes the variables and grids of the DP problem, which consists of two control inputs and three dynamic states. Recall that one of the control variables, $T_{M/G}$, is

eliminated by the perfect T_{clutch} cancellation assumption using the perfect $T_{M/G}$ controller in (5.14). This allows for perfect disturbance rejection as long as the magnitude of T_{clutch} is smaller than the available $T_{M/G}$.

Table 5.1: Variables and grids of the engine-start control DP problem

	Variables	Grid
Stage (k)	Time	[0:0.001:0.5] sec
Control (u)	Clutch Pressure (P_{clutch})	[0:25:1000] kPa
	Firing Command (*Firing*)	[0, 1]
State (x)	Engine Speed (ω_e)	[0:25:1500] rpm
	Crank Angle (θ_{crank})	[0:5:715] deg
	Manifold Pressure (*MAP*)	[0.5:0.1:1] bar

There are three important parameters that must be determined before solving the optimization problem. These are input speed (ω_i), driver demand at the transmission input ($T_{i,dem}$), and initial crank angle ($\theta_{crank,0}$). These parameters may have a significant impact on the optimal solution because 1) the input speed is the target engine speed, 2) the maximum M/G torque depends on the input speed, and 3) $T_{i,dem}$ together with $T_{M/G,max}$ determines the available M/G torque. Although $\theta_{crank,0}$ may seem to have an influence on the optimal solution, we have analytically shown that the optimal solution is not a function of $\theta_{crank,0}$. In this study, we chose a set of these parameters (ω_i =1300rpm, $T_{i,dem}$=100Nm, $\theta_{crank,0}$=0deg) as an example to illustrate the design method. In addition, MAP_{target} = 0.6 bar and ω_{firing} = 700rpm are used in this study, but different values may be used for more conservative solutions, depending on the vehicle design and application.

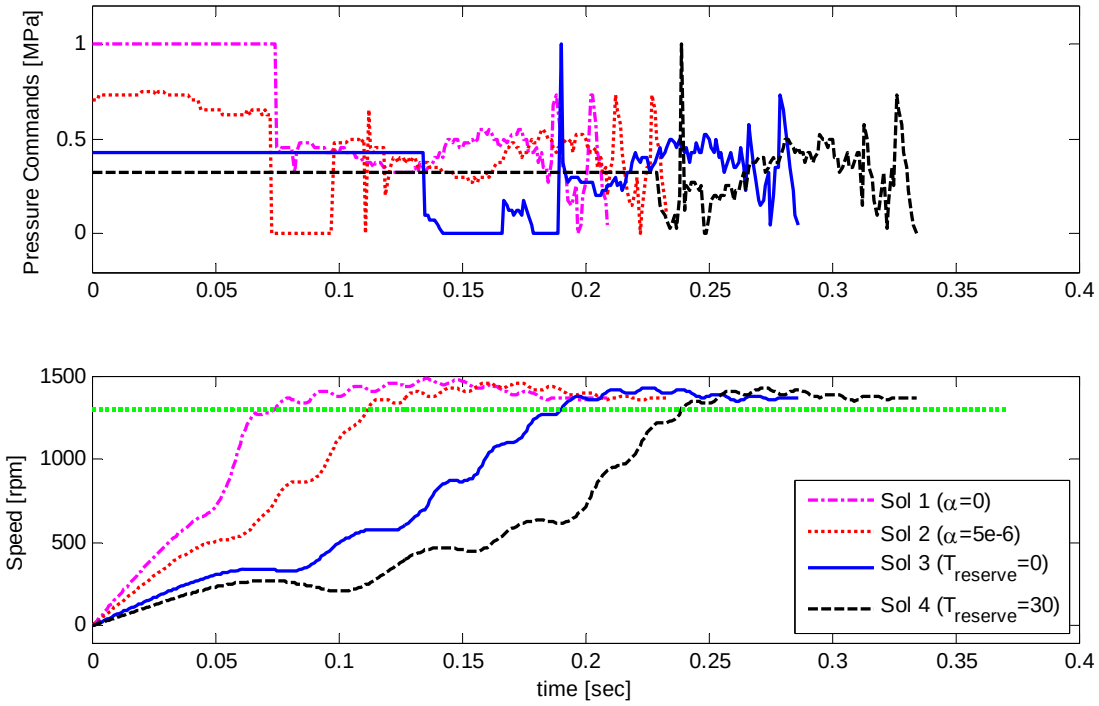

Figure 5.11: Optimal pressure commands and engine speed profiles of various DP solutions. (β = 1e-6, γ = 1e-6 for all solutions)

5.2.4 DP Results

Figure 5.11 summarizes several solutions of both Optimal Control Problems 1 and 2. Note that the optimal solutions are comparable to the conceptual sketch shown in Figure 5.9. Also, recall that the actuator dynamics and the compression-to-firing transition model are neglected for DP simulations, and the engine-start times will increase when these realistic models are included. Figure 5.11 illustrates that the absolute minimum time solution (Sol. 1) can start the engine very quickly with high clutch pressure. However, the torque error for this solution is very large because all of the motor torque is used to start the engine. In fact, some of the vehicle inertial energy is reversely transferred to the engine. With increasing penalty on torque error, the torque error decreases at the cost of the engine-start time. Note that the overshoot also decreases with increasing time because there is a sufficient time to reduce *MAP* for slower solutions. Sol. 3 and 4 show that the time also trades off with torque reserve as expected. In particular, Figure 5.12

shows that the engine-start time directly trades off with the initial clutch pressure, which is held constant during the engine-driven phase, as the analytical approach showed.

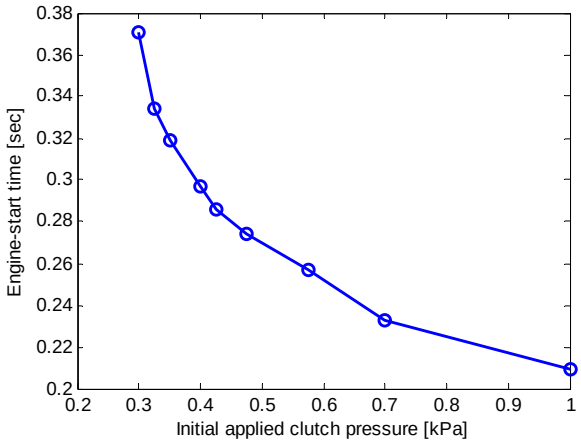

Figure 5.12: Trade-off between initial clutch pressure and engine-start time.

Although Optimal Control Problem 1 is solved to illustrate possible trade-offs, the solutions are less likely to be used on production vehicles because the interruption of power supply will not be acceptable. Instead, torque reserve solutions are more likely used to prepare for possible increases in driver demand during on engine-start. This leads to trade-offs as shown in Figure 5.13, and a designer must choose the proper balance between fast start-up and torque reserve depending on the various operating conditions including driver demand, vehicle speed, gear, and supervisory controller command.

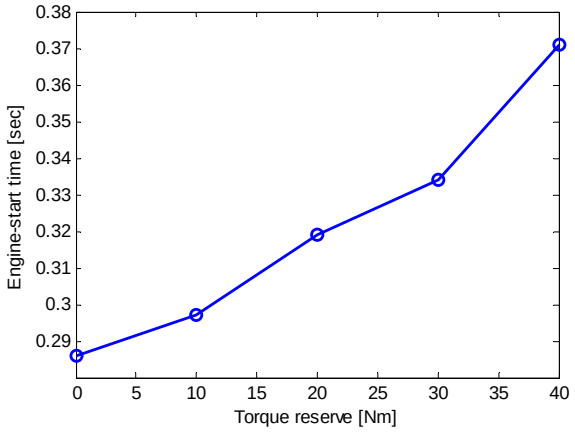

Figure 5.13: Trade-off between torque reserve and engine-start time.

Figure 5.14 shows detailed simulation responses of a sample DP solution for 20Nm of torque reserve. Similar to the analytical solution, the DP solution also suggests that we start with a constant clutch pressure that utilizes all of the available motor torque, and starts firing as soon as the minimum firing speed constraint is met for fast start-up. Then, when the engine speed exceeds the input speed, the clutch pressure is reduced to allow for overshoot, and then the pressure is increased to bring the speed back down to the desired slip speed as *MAP* approaches the target *MAP*. Note that the clutch pressure is somewhat noisy during the engine-driving phase and has a large spike at 0.24sec as $\Delta\omega$ approaches 0. This spike is again due to the hyper-tangent clutch model with μ crossing 0 at $\Delta\omega$=0 (see Figure 5.6). Given the slow response of the hydraulic actuator, these are difficult to implement, and we will discuss how to implement DP solutions in the following section.

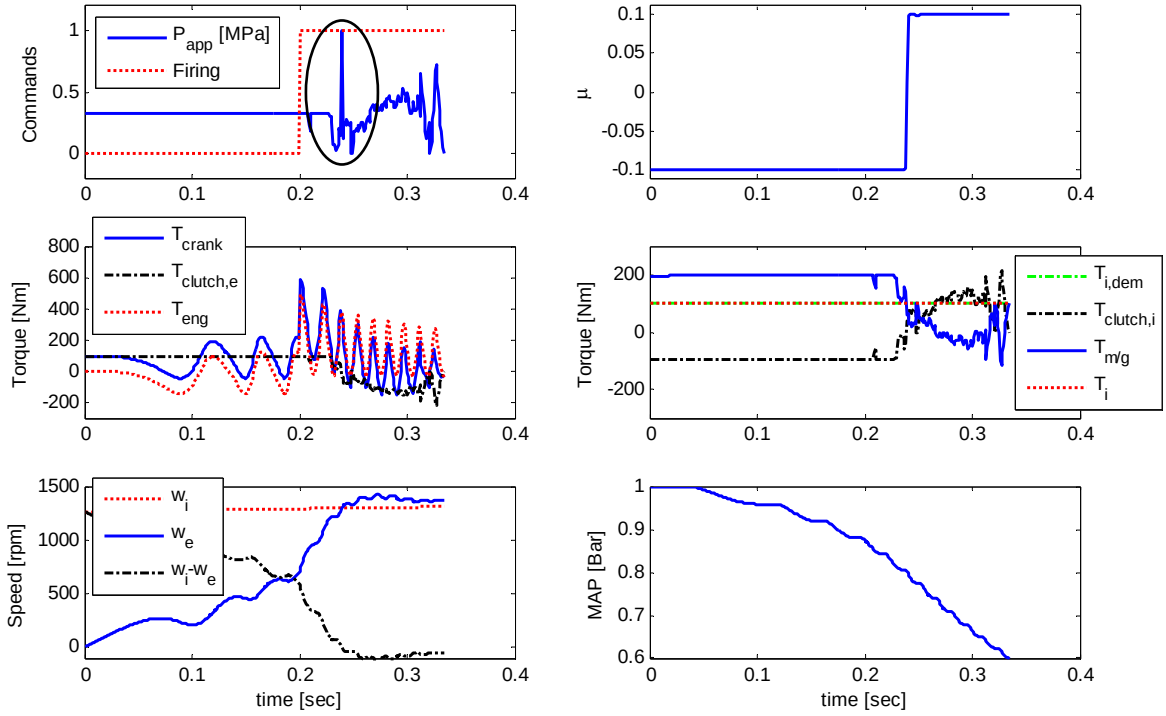

Figure 5.14: Simulation results of a torque reserve DP solution [Sol. 4].
($T_{reserve}$ = 30Nm, β = 1e-6, γ = 1e-6)

5.3 Real-time Control Implementation

5.3.1 Direct implementation of the DP control policy

For the supervisory control of HEVs and PHEVs investigated in Chapters 3 and 4, DP results could not be directly implemented because the output of the DP algorithm is a time-varying control policy, and an extraction process was needed for the implementation of DP results. The time dependence of this control policy was strong because the vehicle speed and driver power demand were constrained at every time step k by the driving cycles. This, however, is not the case for the engine-start DP problem. Neither state variable nor disturbance input is constrained at time step k, and the DP control policy is in the form of a time-varying (time-dependent) full state feedback look-up table. That is $u_k^*(\omega_e,\theta_{crank},MAP,k)$ where k is the time step. Furthermore, Figure 5.15 shows that the time-dependence of the DP control policy u_k^* is negligible.

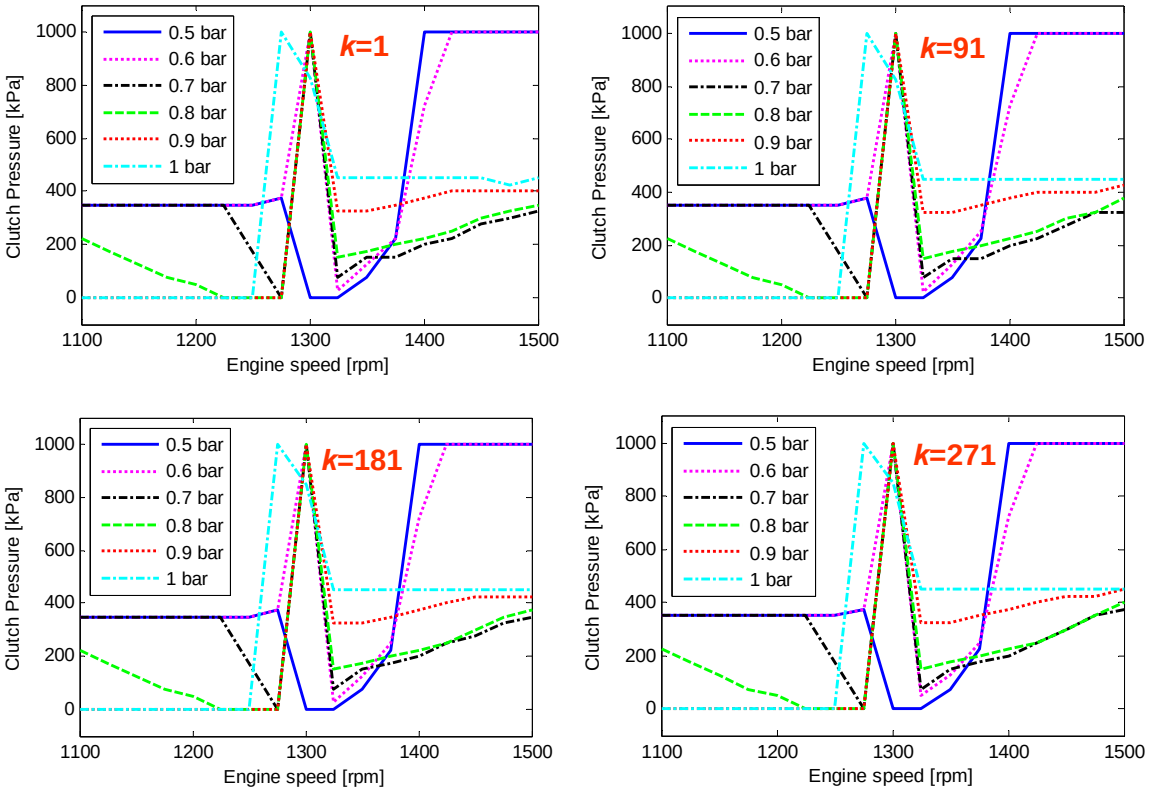

Figure 5.15: DP control policy (u_k^*) at various time steps k (θ_{crank}=0 and $T_{reserve}$=30Nm).

Note that only clutch pressure commands at high engine-speed are shown here, because DP suggests initial-fire at the minimum firing speed and pressure command at low speed are constant. From Figure 5.15, we can conclude that the DP control policy u_k^* is independent of time k. Thus,

$$u^*(x,k) \approx u^*(x) \tag{5.35}$$

and u_k^* can be directly implemented in the form of a full state feedback controller without any extraction/learning process.

Although the direct implementation is easy in theory, it is not so trivial in reality because fast changes in clutch pressure cannot be realized by the hydraulic actuator, and thus filtrations and calibrations of u^* would be necessary for real-world implementations. For instance, we must smooth out u^* by eliminating spikes around 1300rpm shown in Figure 5.15. These spikes are the results of the clutch model approximation near zero slip speed (we used a hyper-tangent function for DP purposes and a transmission input speed of 1300rpm).

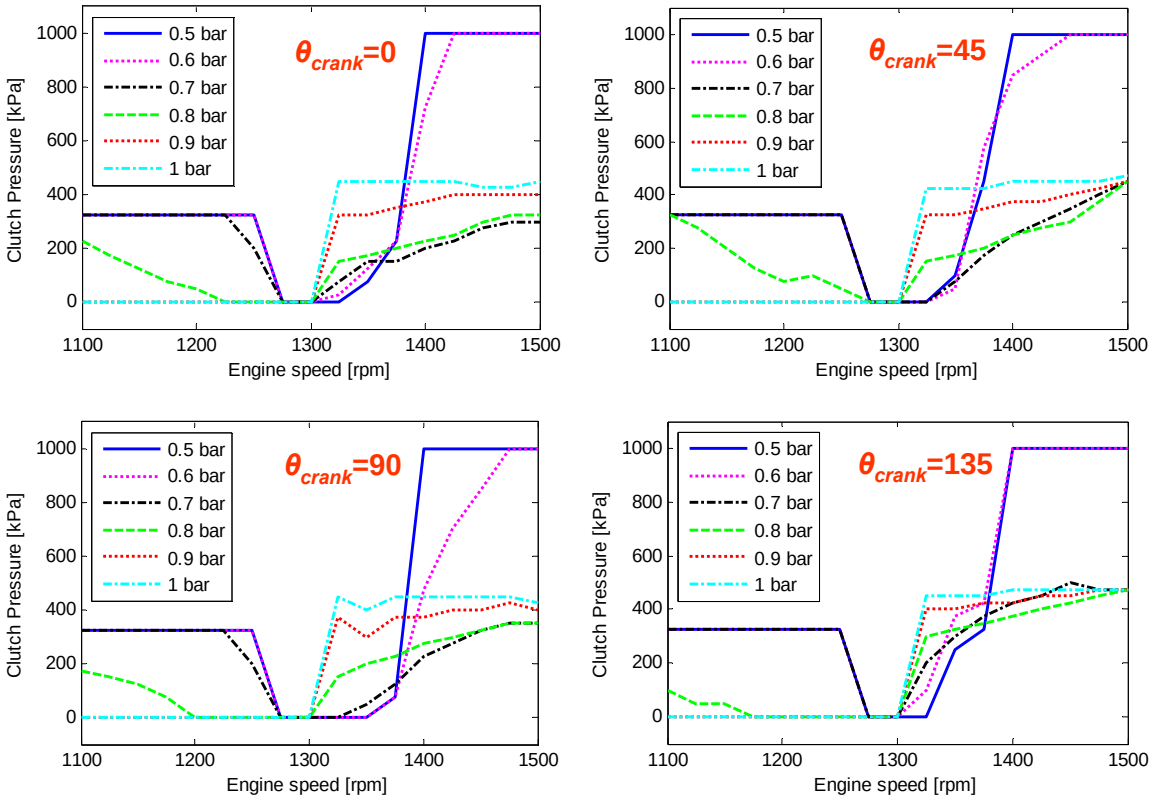

Figure 5.16: Filtered DP control policy at various crank angles (k=1 for $T_{reserve}$=30Nm).

Further filtration and calibration of the pressure commands around 1300rpm would be necessary to reduce NVH due to sharp changes in clutch torque (i.e. the direction of clutch torque changes when the direction of the slip speed changes).

In addition to the time-independence, further reduction of the control policy is sought by testing the dependency of the control policy on the crank angle. Figure 5.16 shows the filtered DP control policy at various crank angles and indicates that the DP control policy slightly changes with respect to the crank angle due to the firing torque ripples. Thus, u^* depends on all three states, and the full state feedback policy cannot be further reduced.

The filtered DP policy (Figure 5.16) is directly implemented, and Figure 5.17 shows the simulation results of the direct implementation of the filtered DP control policy. These results show nearly identical simulation responses to the original DP responses (Figure 5.14) without the pressure spikes.

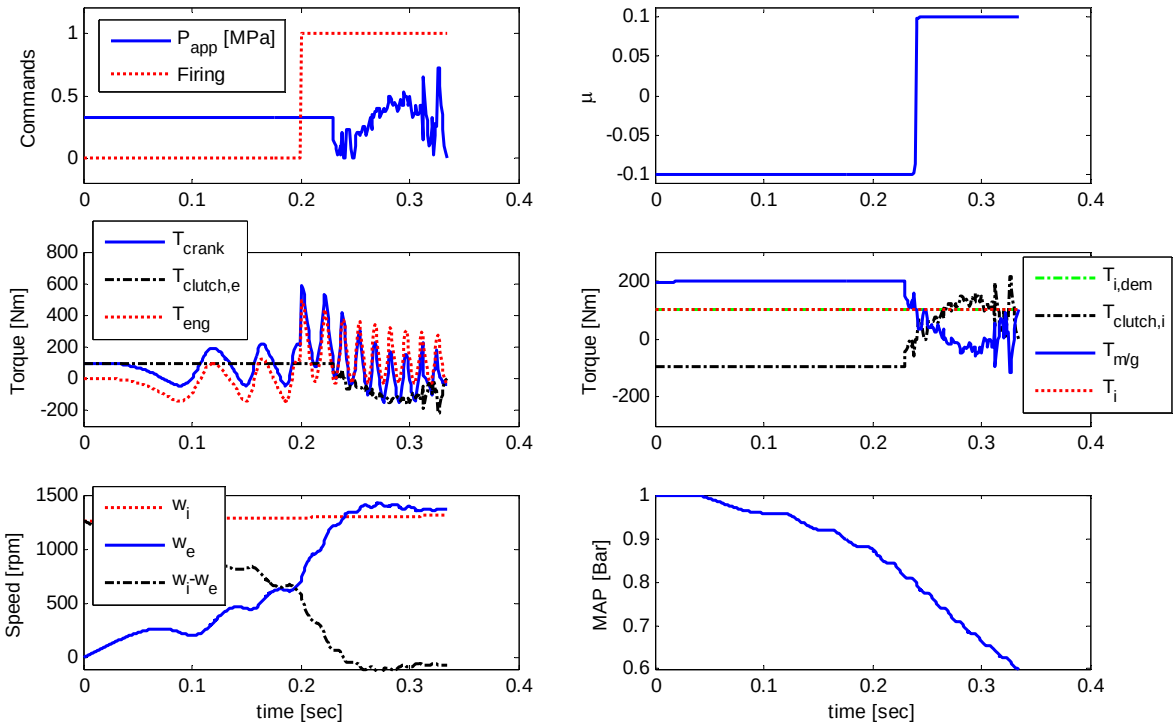

Figure 5.17: Simulation results of the directly implemented DP control policy.
($T_{reserve}$ = 30Nm, β = 1e-6, γ = 1e-6)

5.3.2 Controller algorithm

Figure 5.18 illustrates the proposed controller architecture in a block diagram. $G_p(s)$ is the engine-start model that was used for optimization, and $G_a(s)$ is the clutch actuator dynamics we neglected for optimization purposes. In this control architecture, the objective is to design $C_i(s)$, $C_o(s)$, and $C_m(s)$; inner-loop controller, outer-loop controller, and motor controller respectively. First of all, design of $C_i(s)$ is a nonlinear control problem, but it has been extensively studied to achieve fast reference (P_r) tracking performance. Thus, we assume that the actuator loop is a first order transfer function. Design of $C_o(s)$ is what this study has investigated, and the DP control policy can be directly applied here after minor calibrations. The roles of $C_o(s)$ include selecting a proper torque reserve based on the driver demand ($T_{i,dem}$) and available motor torque ($T_{M/G,max}$). Lastly, design of $C_m(s)$ is trivial under the perfect clutch torque cancellation assumption, assuming T_{clutch} can be accurately estimated. However, accurate estimation of the clutch torque is a challenging problem. In fact, estimation error coupled with fast but non-negligible motor dynamics may be the main source of the NVH, and the design of $C_m(s)$ will require both estimation and feedback control algorithms to reduce NVH.

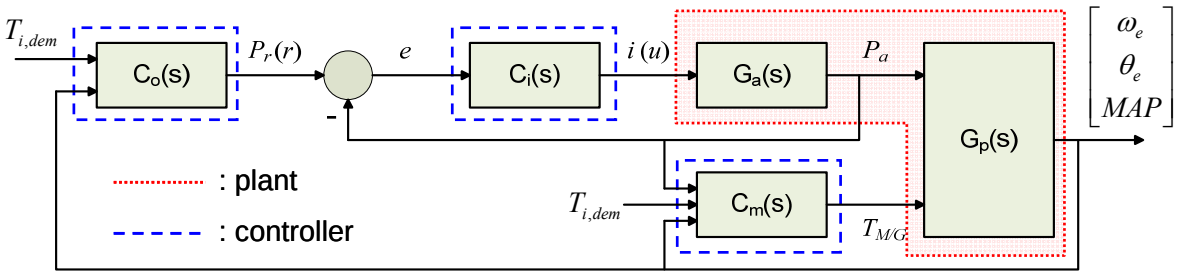

Figure 5.18: Block diagram of the engine-start control architecture.

5.3.3 Control sequence

The engine-start control is an open-loop control problem; the engine-start process is initiated when the supervisory controller requests hybrid mode, and ends when the engine reaches the target speed and *MAP*. Thus, the sequence of the open-loop control algorithm is proposed along with the control architecture developed above.

1. Determine $P_r(t)$ based on $T_{m/g,max}$, $T_{i,dem}$, and $T_{reserve}$.
2. Command $P_r(t)$ while estimating T_{clutch} for perfect disturbance rejection using the M/G.
3. When $\omega_e = \omega_i$, check if $MAP < MAP_{target}$ to find out whether ω_e is ready for the clutch lock-up.
4. If ω_e and MAP are ready for the clutch lock-up, lock up the clutch.
5. Else, adjust $P_r(t)$ using a DP-based feedback controller until $MAP < MAP_{target}$, while continuing to cancel out the clutch torque.

The main design variable in this algorithm is to select a proper level of torque reserve that balances the engine-start time and torque responsiveness based on the driver demand and vehicle states. In addition, it can be beneficial to choose $T_{reserve}$ such that $MAP=MAP_{target}$ when $\omega_e = \omega_i$ for the first time. This choice would avoid overshoot as well as aggressive clutch engagement.

We have demonstrated how the direct implementation of DP control policy can be realized in a real-time control algorithm and a control sequence. In the engine-start control algorithm, the DP-based control policy developed in this chapter provides reference clutch pressure commands that optimize the design criteria, but other controllers (e.g. hydraulic actuator and motor controllers) must be adequately designed and coordinated with the DP control policy to achieve the designed performance.

CHAPTER 6
CONCLUSION AND FUTURE WORK

6.1 Conclusions

In this dissertation, models and design methods that optimize fuel economy, emissions, and drivability are developed for control of Hybrid Electric Vehicles (HEVs) and Plug-in HEVs (PHEVs).

Studies in the literature showed that the instantaneous optimization method is a good approach for the fuel economy optimization problem. However, the instantaneous optimization control approach may suffer from frequent engine on/off and gear-shift events due to its inherent inability to handle horizon-based performance objectives such as emissions and drivability, and these drivability issues must be properly resolved. When horizon-based performance objectives are considered, dynamic optimization methods are proper tools to solve an optimal control problem and find an optimal strategy. For instance, Dynamic Programming (DP) results indicated that a late-shift strategy with higher engine load is important during cold-starts for fast catalyst warm-up, and an early-shift strategy with higher engine on/off threshold power is crucial for the optimal charge depleting strategy of a PHEV. Moreover, an adaptive supervisory control algorithm that consists of three modular control strategies (engine on/off, gear-shift, and power-split strategies) is proposed based on the extracted DP results. Each individual control strategy is properly adjusted to minimize fuel consumption and tail-pipe emissions under various Energy-to-Distance Ratio (EDR) and catalyst temperature conditions, assuming that the remaining trip distance is known for the optimal control of PHEVs. This DP-based control algorithm is easy to adjust and generic enough to be used for both HEVs and PHEVs. Thus, the main advantages of

the DP-based SPC over the instantaneous optimal controller are 1) simple and intuitive control logic, 2) modular controller design, and 3) adjustability to optimize horizon performance objectives.

On the contrary, the extraction process is not necessary when DP method is applied to the engine-start control problem. The DP control policy is found to be nearly time-invariant because neither state variable nor disturbance input is constrained at time step k, and thus it can be directly implemented in the form of a full state feedback controller after proper calibrations. Moreover, the analyses of the DP results and control policy illustrated that a constant clutch pressure command is a good practical control strategy, and the engine-start time trades off with the motor torque reserve. Thus, the main design variable of engine-start control is to choose a proper clutch pressure that balances the engine-start time and torque reserve based on the driver demand and vehicle states.

In conclusion, this doctoral thesis studied merits and limitations of the instantaneous and horizon-based optimization approaches in applications to control of HEVs and PHEVs for multiple objectives. The instantaneous approach can be an effective tool for problems with instantaneous performance objectives, but the horizon optimization approach is the proper choice when horizon-based performance objectives are considered.

6.2 Future Work

- **Application of the comprehensive extraction method for other configurations**

In this study, a design method for the cold-start SPC has been developed using the comprehensive extraction method for the pre-transmission parallel hybrid configuration. Although this method may not be directly applicable to other hybrid configurations, such as series and power-split, the overall approach and comprehensive extraction method may be applicable to extract useful optimal control strategies and design control algorithms for other configurations.

- **Estimation of true Energy-to-Distance Ratio (EDR) under various uncertainties**

In Chapter 4, an adaptive supervisory powertrain controller (SPC) was developed to optimize fuel economy and emissions under known trip distances. However, when this is applied to real-world vehicles, the optimality of the proposed controller becomes questionable due to many uncertainties that arise from real-world driving conditions such as vehicle mass, driving style, and elevation profile. Thus, EDR must be properly adjusted to reflect the true EDR for current and future driving conditions. Finding true EDR is, however, difficult because it needs to be estimated based on multiple uncertainties that change in real-time, and future information is generally not available.

- **Modeling and control of the engine-start for NVH reduction**

In Chapter 5, assuming that perfect clutch torque estimation and cancellation are feasible, drivability has been the focus of the engine-start control, and a corresponding optimal control problem has been formulated and solved by various methods. However, perfect estimation and cancellation are challenging problems and likely infeasible. If the perfect clutch torque estimation assumption fails, NVH problems arise, and a feedback controller that attenuates NVH would be necessary as a part of the motor controller because the motor torque can be much more quickly and accurately controlled than the clutch torque.

Since NVH control problems tend to reside in the high frequency region, the engine-start control for NVH poses a different control problem from the one that has been studied in this dissertation. A much more detailed model, including shaft dynamics, will be necessary, and classical control theories, such as loop shaping, will be more useful than the optimal control theories.

APPENDIX A
MATHEMATICAL BACKGROUND

Classical Optimal Control Theory: Variational Approach

The variational approach is widely used in various applications including HEV control problems due to its elegant mathematical formulation and results. The main feature of the variational approach is that it converts the optimal control problem into a two-point boundary value problem. However, this two-point boundary value problem often must be solved iteratively to find the solution, which guarantees neither convergence nor global optimality. Despite these disadvantages, it is a very useful tool to solve the optimal control problem. In the following, the general form (free time and partly free final state) of the variational approach is summarized.

The optimal control problem is to find $t_1^* > t_0$, $x^*(t)$, and $u^*(t)$ for $t_0 \le t \le t_1^*$ that

$$\text{Minimize } J = K\left(x(t_1), t_1\right) + \int_{t_0}^{t_1} L(x,u,t)\,dt \tag{A.1}$$

$$\text{Subject to } \dot{x} = f(x,u,t) \tag{A.2}$$

$$x_0(t_1) = x_0 \tag{A.3}$$

$$\psi_i\left(x(t_1), t\right) = 0 \tag{A.4}$$

where $K(x,t)$ is terminal cost function, $L(x,u,t)$ is instantaneous cost function, $f(x,u,t)$ is system dynamics, $\psi_i(x,t)$ is final state constraints, t_0 is initial time, and x_0 is initial state, and these functions and initial conditions are all given. Then, the Hamiltonian function is defined as

$$H = L(x,u,t) + p(t) f(x,u,t)\,, \tag{A.5}$$

and the necessary conditions for the solution of the above optimal control problem are as follows [5,10,41]:

If a solution t_1^*, $x(t)$, $u(t)$ for $t_0 \le t \le t_1^*$ is a local minimizer, then there is $p(t)$ such that

$$\dot{x}^* = \frac{\partial H}{\partial p}(x^*, p, u^*, t) \tag{A.6}$$

$$\dot{p} = -\frac{\partial H}{\partial x}(x^*, p, u^*, t) \tag{A.7}$$

$$\frac{\partial H}{\partial u}\left(x^*, p, u^*, t\right) = 0 \tag{A.8}$$

$$x^*(t_0) = x_0 \tag{A.9}$$

$$\psi_i\left(x^*(t_1), t\right) = 0 \tag{A.10}$$

$$p(t_1^*) - \frac{\partial K}{\partial x}(x^*(t_1^*), t_1^*) = \sum_{i=1}^{p} \rho_i \frac{\partial \psi_i}{\partial x}(x^*(t_1^*), t_1^*) \tag{A.11}$$

$$-H\left(x^*(t_1^*), p(t_1^*), u(t_1^*), t_1^*\right) - \frac{\partial K}{\partial t_1}(x^*(t_1^*), t_1^*) = \sum_{i=1}^{p} \rho_i \frac{\partial \psi_i}{\partial t_1}(x^*(t_1^*), t_1^*) \tag{A.12}$$

This two-point boundary value problem can be numerically solved by iterative search algorithms such as Sequential Quadratic Programming (SQP).

Special case (instantaneous optimization): HEV control for fuel economy

Equivalent Consumption Minimum Strategy (ECMS) is a well-known instantaneous optimization method, which minimizes the sum of fuel and battery energy consumption at every instant, where the weighting factor of the battery energy consumption must be properly selected to achieve charge sustenance [68,69,79,80]. ECMS was first developed based on engineering intuition, and then its near-optimal performance was supported by the analogy between the variational approach and ECMS as follows [80].

Find the optimal control trajectory $u(t)$ that

$$\text{Minimize } J = \int_{t_0}^{t_1} \dot{m}_{fuel}(u)dt \tag{A.13}$$

$$\text{Subject to } \dot{SOC} = f(SOC, u) \tag{A.14}$$

$$SOC(t_0) = SOC(t_1) \tag{A.15}$$

Then, define the Hamiltonian function as

$$H(x,u,p) \equiv \dot{m}_{fuel}(u) + p \cdot f(SOC,u), \tag{A.16}$$

and the necessary conditions are

$$\dot{SOC}^* = f(SOC^*,u^*) \tag{A.17}$$

$$\dot{p} = -\frac{\partial f(SOC^*,u^*)}{\partial SOC} \tag{A.18}$$

$$\frac{\partial \dot{m}_{fuel}(u^*)}{\partial u} + p\frac{\partial f(SOC^*,u^*)}{\partial u} = 0 \tag{A.19}$$

If we assume that the open circuit voltage and internal resistance maps are not functions of the battery SOC, that is

$$\dot{SOC} = f(SOC,u) \approx \widetilde{f}(u) \tag{A.20}$$

Then, the Hamiltonian function becomes

$$\widetilde{H}(u,p) \equiv \dot{m}_{fuel}(u) + p \cdot \widetilde{f}(u) \tag{A.21}$$

and the necessary conditions are

$$\dot{SOC}^* = \widetilde{f}(u^*) \tag{A.22}$$

$$\dot{p} = -\frac{\partial \widetilde{f}(u^*)}{\partial SOC} = 0 \tag{A.23}$$

$$\frac{\partial \dot{m}_{fuel}(u^*)}{\partial u} + p\frac{\partial \widetilde{f}(u^*)}{\partial u} = 0 \tag{A.24}$$

Under this assumption, $\dot{p}(t) = 0$ and the costate $p(t)$ is now constant. In addition, since u is constrained due to the limited engine power, equation (1.10) is replaced with

$$u^*(t) = \arg\min_u \left\{\widetilde{H}(u,p)\right\} \tag{A.25}$$

using the Pontryagin's Minimium Principle (PMP). These necessary conditions with a single constant costate becomes an instantaneous optimization problem and can be easily solved; one can compute $u^*(p)$ and find p that meets the charge sustenance constraint for a given driving cycle.

Although the variational approach-based static optimization method offers near-optimal performance with relatively simple algorithm for the fuel economy problem, the near-optimality and simplicity no longer hold when horizon-based performance objectives (e.g. emissions and drivability) are considered for simultaneous optimization. For instance, tail-pipe emissions heavily depend on a dynamic state, catalyst temperature, and leads to dynamic costate, $\dot{p}(t) \neq 0$. Therefore, the necessary conditions cannot be simplified and should be numerically solved by the iterative search algorithm. One of the main weaknesses of the variational approach is that the global optimality is not guaranteed because the theory is developed based on the first order calculus of variations, but its solution is globally optimal if 1) the optimization problem is convex or 2) the global minimum exists and there is a unique solution that satisfies the necessary conditions.

Dynamic Programming

Another widely used optimization algorithm is Dynamic Programming (DP). The main advantage of DP over the variational approach is that the global optimality is guaranteed even for non-convex constrained nonlinear optimal control problems. A main drawback is that its computational efforts exponentially increase with the number of state and control variables, also known as curse of dimensionality. Thus, for nonlinear optimal control problems with reasonable size, DP can be a very powerful tool to find the globally optimal solution. In this section, the principle of optimality and the DP algorithm are summarized as follows.

For a discrete-time deterministic dynamic systems,

$$x_{k+1} = f(x_k, u_k, w_k), \qquad k = 0,1,\ldots N\text{-}1 \tag{A.26}$$

if $\pi^* = \{\mu_0^*, \mu_1^*, \mu_2^*, ..., \mu_{N-1}^*\}$, where μ_k maps states x_k into control action $u_k = \mu_k(x_k)$, is the optimal policy that minimizes the following dynamic optimization problem:

Minimize the cost function

$$J = K(x_N) + \sum_{k=0}^{N-1} L_k(x_k, u_k, w_k) \tag{A.27}$$

Subject to

$$g_i(x_i) \le 0, \qquad i = 1,2,...p \tag{A.28}$$

$$h_j(u_j) = 0, \qquad j = 1,2,...q \tag{A.29}$$

$$x_k \in X \subset \mathbf{R}^n, \qquad u_k \in U(x_k, k) \subset \mathbf{R}^m \tag{A.30}$$

where x_k is the state vector at stage k in the space of X, u_k is the control vector, w_k is a predetermined disturbance, L_k is the instantaneous transition cost, K is the terminal cost at the final stage N, and g and h are inequality and equality constraint functions respectively.

Then, the principle of optimality dictates that the truncated policy $\pi_i^* = \{\mu_i^*, \mu_{i+1}^*, \mu_{i+2}^*, ..., \mu_{N-1}^*\}$ is an optimal solution to the following sub-problem.

$$J_i = K(x_N) + \sum_{k=i}^{N-1} L_k(x_k, u_k, w_k) \tag{A.31}$$

where J_i indicates the "cost-to-go" function from stage i to N. Note that constraints are imposed in this dynamic optimization problem. One of the advantages of DP is that it can handle constraints on state and control variables [6,41].

We can extend the idea of the principle of optimality to arrive at the DP algorithm, which allows us to solve the entire dynamic optimization problem by solving a sub-problem for each stage repeatedly backwards in time. In other words, we can solve a much smaller single stage sub-problem for the last stage ($i = N - 1$) resulting in a truncated optimal policy $\pi_{N-1}^* = \{\mu_{N-1}^*\}$, and then solve another single stage sub-problem for the second to last stage ($i = N - 2$) with $\pi_{N-1}^* = \{\mu_{N-1}^*\}$ and cost-to-go J_{N-1}^* information given from the previous sub-problem, and for the

third to last stage, and so on, until the initial stage ($i = 0$), which completes the entire optimization problem with the optimal policy $\pi^* = \{\mu_0^*, \mu_1^*, \mu_2^*, ..., \mu_{N-1}^*\}$ and total optimal cost J^*. Thus, the entire optimization problem is decomposed into a sequence of single stage minimization problems as follows.

Step $N-1$

$$J_{N-1}^* = \min_{u_{N-1}}[K(x_N) + L(x_{N-1}, u_{N-1}, w_{N-1})] \tag{A.32}$$

Step k, $0 \le k < N-1$

$$J_k^* = \min_{u_k}[J_{k+1}^* + L(x_k, u_k, w_k)] \tag{A.33}$$

where optimal policy $\pi_i^* = \{\mu_i^*, \mu_{i+1}^*, \mu_{i+2}^*, ..., \mu_{N-1}^*\}$ gives the optimal cost-to-go J_i^*, which represents the optimal cost from stage i to final stage N. Instead of enumerating all possible control sequences, solving the optimal control problem via the presented DP algorithm promises reduced computation burden and globally optimal solution.

BIBLIOGRAPHY

[1] F. An and M. Barth, "Critical Issues in Quantifying hybrid electric vehicle emissions and fuel consumption," *SAE*, paper 981902, 1998.

[2] D. Assanis, G. Delagrammatikas, R. Fellini, Z. Filipi, J. Liedtke, N. Michelena, P. Papalambros, D. Reyes, D. Rosenbaum, A. Sales, and M. Sasena, "An optimization approach to hybrid electric propulsion system design," *Mechanics of Structures and Machines*, vol. 27, no. 4, pp. 393-421, 1999.

[3] B. Baumann, G. Washington, B. Glenn, and G. Rizzoni, "Mechatronic design and control of hybrid electric vehicles," *IEEE/ASME Trans. on Mechatronics*, vol. 5, no. 1, pp. 58-72, 2000.

[4] R. Bellman, *Dynamic Programming*. New Jersey: Princeton University Press, 1957.

[5] D. S. Bernstein and P. Tsiotras, *A course in classical optimal control*. Unpublished notes, Version: June 15, 2009.

[6] D. P. Bertsekas, *Dynamic Programming and Optimal Control*. 3rd ed., NH: Athena Scientific, 2005.

[7] T. Bradley and A. Frank, "Design, demonstrations and sustainability impact assessments for plug-in hybrid electric vehicles," *Renewable & Sustainable Energy Reviews*, vol. 13, pp. 115-128, 2009.

[8] A. Brahma, Y. Guezennec, and G. Rizzoni, "Dynamic optimization of mechanical/ electrical power flow in parallel hybrid electric vehicles," *Proc. of 5th Int. Symposium in Advanced Vehicle Control*, Ann Arbor, MI, 2000.

[9] E. P. Brandt, Y. Wang, and J. W. Grizzle, "Dynamic modeling of a three-way catalyst for SI engine exhaust emission control," *IEEE Transactions on Control Systems Technology*, vol. 8, no. 5, pp. 767-776, 2000.

[10] A. Bryson and Y. Ho, *Applied Optimal Control*. New York: Taylor & Francis, 1975

[11] CalCars, "All about plug-in hybrids," [online], Available at http://www.calcars.org/ vehicles.html

[12] California's Air Resources Board, [online] Available at http://www.arb.ca.gov/ homepage.htm

[13] M. Canova, Y. Guezennec, and S. Yurkovich, "On the control of engine start/stop dynamics in a hybrid electric vehicle," *ASME Trans. on Dynamic Systems, Measurement, and Control*, vol. 131, 2009.

[14] R. Carlson, M. Duoba, T. Bohn, and A. Vyas, "Testing and analysis of three plug-in hybrid electric vehicles," *SAE*, paper 2007-01-0283, 2007.

[15] R. Carlson, H. Lohse-Busch, M. Duoba, and N. Shidore, "Drive cycle fuel consumption variability of plug-in hybrid electric vehicles due to aggressive driving," *SAE*, paper 2009-01-1335, 2009.

[16] S. H. Chan and D. L. Hoang, "Modeling of catalytic conversion of CO/HC in gasoline exhaust at engine cold-start," *SAE*, paper 1999-01-0452, 1999.

[17] S. H. Chan, D. L. Hoang, and P. L. Zhou, "Heat transfer and chemical kinetics in the exhaust system of a cold-start engine fitted with a three-way catalytic converter," *Proceedings of the Institution of Mechanical Engineers*, vol. 214, Part D, pp. 765-777, 2000.

[18] D. Colvin and B. Masterson, "Challenges of engine starts and drivability in a parallel hybrid-electric system," *SAE*, paper 2004-01-0063, 2004.

[19] J. David and N. Natarajan, "Plant identification and design of optimal clutch engagement controller," *SAE*, paper 2006-01-3539, 2006.

[20] R. I. Davis and R. D. Lorenz, "Engine torque ripple cancellation with an integrated starter alternator in a hybrid electric vehicle: implementation and control," *IEEE Trans. on Industry Applications*, vol. 39, no. 6, pp. 1765-1774, 2003.

[21] S. Delprat, T. M. Guerra, G. Paganelli, J. Lauber, and M. Delhom, "Control strategy optimization for a hybrid parallel powertrain," *Proc. of the American Control Conference*, Arlington, VA, June 2001.

[22] S. Delprat, J. Lauber, T. M. Guerra, and J. Rimaux, "Control of a parallel hybrid powertrain: optimal control," *IEEE Transactions on Vehicular Technology*, vol. 53, no. 3, pp. 872-881 ,2004.

[23] Dieselnet, "Emission Standards – United States," [online], Available at http://www.dieselnet.com/standards/us/

[24] L. Eriksson, "Mean value models for exhaust system temperatures," *SAE*, paper 2002-01-0374, 2002.

[25] A. Elgowainy, A. Burnham, M. Wang, J. Molburg, and A. Rousseau, "Well-to-wheels energy use and greenhouse gas emissions of plug-in hybrid electric vehicles," *SAE*, paper 2009-01-1309, 2009.

[26] M. Fellah, G. Singh, A. Rousseau, S. Pagerit, E. Nam, and G. Hoffman, "Impact of real-world drive cycles on PHEV battery requirements," *SAE*, paper 2009-01-1383, 2009.

[27] Z. Fillipi, L. Louca, B. Daran, C. Lin, U. Yildir, B. Wu, M. Kokkolaras, D. Assanis, H. Peng, P. Papalambros, J. Stein, D. Szkubiel, and R. Chapp, "Combined optimization of design and power management of the hydraulic hybrid propulsion system for the 6x6 medium truck," *Int. Journal of Heavy Vehicle Systems*, vol. 11, no. 3/4, 2004.

[28] V. Freyermuth, E. Fallas, and A. Rousseau, "Comparison of powertrain configuration for plug-in HEVs from a fuel economy perspective," *SAE*, paper 2008-01-0461, 2008.

[29] Gale, Cengage Learning, "Understanding Emissions regulations," [online], Available at http://findarticles.com/p/articles/mi_m3012/is_9_183/ai_108098150

[30] J. Gonder and T. Markel, "Energy management strategies for plug-in hybrid electric vehicles," *SAE*, paper 2007-01-0290, 2007.

[31] L. Guzzella, and A. Sciarretta, *Vehicle Propulsion Systems*. *Introduction to Modeling and Optimization*. Berlin: Spinger-Verlag, 2005.

[32] N. A. Henein and M. K. Tagomori, "Cold-start hydrocarbon emissions in port-injected gasoline engines," *Progress in Energy and Combustion Science*, vol. 25, no. 6, pp. 563-593, 1999.

[33] J. B. Heywood, *Internal Combustion Engine Fundamentals*. New York: McGraw-Hill, 1988.

[34] Impala Platinum Limited, "Emission standards," [online], Available at http://www.implats.co.za /m/ emissions.asp

[35] Y. Ito, S. Tomura, and S. Sasaki, "Development of vibration reduction motor control for hybrid vehicles," *The 33rd annual conference of the IEEE industrial electronics society*, pp. 516-521, Taipei, Taiwan, 2007.

[36] V. Ivanović, Z. Herold, J. Deur, M. Hancock, and F. Assadian, "Experimental characterization of wet clutch friction behaviors including thermal dynamics," *SAE*, paper 2009-01-1360, 2009.

[37] V. Johnson, K. Wipke, and D. Rausen, "HEV control strategy for real-time optimization of fuel economy and emissions," *SAE*, paper 2000-01-1543, 2000.

[38] J. Kallenbach, P. Florchinger, and A. Heibel, "Modeling of automotive aftertreatment catalysts," *SAE*, paper 1999-01-3043, 1999.

[39] D. Karbowski, S. Pagerit, J. Kwon, A. Rousseau, and K. Pechmann, "Fair comparison of powertrain configuration for plug-in hybrid operation using global optimization," *SAE*, paper 2009-01-1334, 2009.

[40] J. Kavanagh, "Untangling U.S. Vehicle Emissions Regulations," [online], Available at http://www.edmunds.com/ownership/techcenter/articles/123901/article.html

[41] D. Kirk, *Optimal Control Theory*: *An Introduction*. New Jersey: Prentice-Hall, 1970.

[42] I. Kolmanovsky, M. Nieuwstadt, and J. Sun, "Optimization of complex powertrain systems for fuel economy and emissions," *IEEE Int. Conference on Control Applications*, Hawaii, 1999.

[43] G. C. Koltsakis, P.A. Konstantinidis, and A.M. Stamatelos, "Development and application range of mathematical models for 3-way catalytic converters," *Applied Catalysis B*: *Environmental*, vol. 12, pp.161-191, 1997.

[44] M. Komatsu, T. Takaoka, T. Ishikawa, Y. Gotouda, N. Suzuki, and T. Ozawa, "Study on the potential benefits of plug-in hybrid systems," *SAE*, paper 2008-01-0456, 2008.

[45] M. Kromer, and J. Heywood, "A comparative assessment of electric propulsion systems in the 2030 US light-duty vehicle fleet," *SAE*, paper 2008-01-0459, 2008.

[46] M. Kuang, "An investigation of engine start-stop NVH in a power split powertrain hybrid electric vehicle," *SAE*, paper 2006-01-1500, 2006.

[47] D. Kum, H. Peng, and N. K. Bucknor, "Supervisory control of parallel hybrid electric vehicles for fuel and emissions reduction," *ASME Transactions on Dynamic Systems, Control, and Measurement*. (accepted)

[48] D. Kum, H. Peng, and N. K. Bucknor, "Optimal control of plug-in hybrid electric vehicles for fuel economy under various travel distances," *6th IFAC Symposium Advances in Automotive Control*, Munich, Germany, 2010. (accepted)

[49] P. R. Kumar and P. Varaiya, *Stochastic Systems: Estimation, Identification, and Adaptive Control*. New Jersey: Prentice-Hall, 1986.

[50] J. Kwon, J. Kim, E. Fallas, S. Pagerit, and A. Rousseau, "Impact of drive cycles on PHEV component requirements," *SAE*, paper 2008-01-1337, 2008.

[51] P. M. Laing, M. D. Shane, S. Son, A. A. Adamczyk, and P. Li, "A simplified approach to modeling exhaust system emissions: SIMTWC," *SAE*, paper 1999-01-3476, 1999.

[52] C.-C. Lin and H. Peng, "Power management strategy for a parallel hybrid electric truck," *IEEE Trans. on Control Systems Technology*, vol. 11, no. 6, pp. 839-849, 2003.

[53] C.-C. Lin and H. Peng, "Modeling and control strategy development for hybrid vehicles." Ph.D. dissertation, University of Michigan, 2004.

[54] J. Liu and H. Peng, "Modeling and control of a power-split hybrid vehicle," *IEEE Trans. on Control Systems Technology*, vol. 16, no. 6, pp. 1242-1251, 2008.

[55] S. M. Lukic, and A. Emadi, "Emissions and fuel economy trade-off for hybrid vehicles using fuzzy logic," *Mathematics and computers in simulation*, vol. 66 no. 2-3, pp. 155-172, 2004.

[56] R. Mäki, P. Nyman, R. Olsson, and B. Ganemi, "Measurement and characterization of anti-shudder properties in wet clutch applications," *SAE*, paper 2005-01-0878, 2005.

[57] T. Markel and K. Wipke, "Optimization techniques for hybrid electric vehicle analysis using ADVISOR," *Proc. of Int. Mechanical Engineering Congress and Exposition*, New York, 2001.

[58] T. Markel and A. Simpson, "Plug-in electric vehicle energy storage system design," *Advanced Battery Conference*, Baltimore, MD, 2006.

[59] J. M. Miller, *Propulsion Systems for Hybrid Vehicles*. The Institution of Engineering and Technology, 2004.

[60] M. Mehaffy, "The urban dimensions of climate changes", [online] Available at http://www.planetizen.com/node/41801

[61] S. Moura, H. Fathy, D. Callaway, and J. Stein, "A Stochastic Optimal Control Approach for Power Management in Plug-in Hybrid Electric Vehicles," *Proc. of the 2008 ASME Dynamic Systems and Controls Conference*, Ann Arbor, MI, 2008.

[62] J. D. Murrell, G. M. Lewis, D. M. Baker, and D. N. Assanis, "An early-design methodology for predicting transient fuel economy and catalyst-out exhaust emissions," *SAE*, paper 971838, 1997.

[63] C. Musardo and G. Rizzoni, "A-ECMS: an adaptive algorithm for hybrid electric vehicle energy management," *Proc. 44th IEEE Conference on Decision and Control, 2005 European Control Conference*, Seville, Spain, 2005.

[64] K. Muta, M. Yamazaki, and J. Tokieda, "Development of new-generation hybrid system THS II - drastic improvement of power performance and fuel economy," *SAE*, paper 2004-01-0064, 2004.

[65] National Renewable Energy Laboratory, "Advanced Vehicle Simulator (ADVISOR)," [online], Available at http://www.ctts.nrel.gov/analysis/, 2002.

[66] A. Onorati, G. D'Errico, and G. Ferrari, "1D fluid dynamic modeling of unsteady reacting flows in the exhaust system with catalytic converter for SI engines," *SAE*, paper 2000-01-0210, 2000.

[67] W. Ortmann, D. Colvin, S. Fozo, M. Encelewski, and M. Kraska, "Incorporating an electric machine into the transmission control of Ford's modular hybrid transmission," *SAE*, paper 2004-01-0069, 2004.

[68] G. Paganelli, S. Delprat, T. M. Guerra, J. Rimaux, and J. J. Santin, "Equivalent consumption minimization strategy for parallel hybrid powertrains," *Proc. Fall VTC-01 Conference*, Atlantic City, NJ, 2002.

[69] P. Pisu, and G. Rizzoni, "A comparative study of supervisory control strategies for hybrid electric vehicles," *IEEE Trans. on Control Systems Technology* , vol. 15, no. 3, pp. 506-, 2007.

[70] G. Pontikakis, C. Papadimitriou, and A. Stamatelos, "Kinetic parameter estimation by standard optimization methods in catalytic converter modeling," *Chemical Engineering Communications*, vol. 191, no. 11, pp. 1473-, 2004.

[71] M. L. Puterman, *Markov Decision Processes: Discrete Stochastic Dynamic Programming*. 1st ed., Wiley-Interscience, 2005.

[72] G. Rizzoni, Y. Guezennec, A. Brahma, X. Wei, and T. Miller, "VP-SIM: A unified approach to energy and power flow modeling simulation and analysis of hybrid vehicles," *SAE*, paper 2000-01-1565, 2000.

[73] A. Rousseau, S. Pagerit, G. Monnet, and A. Feng, "The new PNGV System Analysis Toolkit PSAT V4.1 – evolution and improvement," *SAE*, paper 2001-01-2536, 2001.

[74] C. Samaras and K. Meisterling, "Life cycle assessment of greenhouse gas emissions from plug-in hybrid vehicles: implications for policy," *Environmental Science & Technology*, vol. 42, no. 9, pp. 3170-3176, 2008.

[75] P. R. Sanketi, J. K. Hedrick, and T. Kaga, "A simplified catalytic converter model for automotive cold-start control applications," *Proc. of IMECE2005*, Orlando, Florida, 2005.

[76] P.R. Sanketi, J. C. Zavala, and J. K. Hedrick, "Automotive engine hybrid modeling and control for reduction of hydrocarbon emissions," *International Journal of Control*, vol. 79, no. 5, pp. 449-464, 2006.

[77] N. Schouten, M. Salman, N. Kheir, "Fuzzy logic control for parallel hybrid vehicles," *IEEE Trans. on Control Systems Technology*, vol. 10, no. 3, pp. 460-468, 2002.

[78] F. Schäfer, and R. van Basshuysen, *Reduced Emissions and Fuel Consumption in Automobile Engines*. Wien, New York: Springer-Verlag, 1995.

[79] A. Sciarretta, M. Back, and L. Guzzella, "Optimal control of parallel hybrid electric vehicles," *IEEE Trans. on Control Systems Technology*, vol. 12, no. 3, pp. 352-363, 2004.

[80] A. Sciarretta, and L. Guzzella, "Control of hybrid electric vehicles: optimal energy-management strategies," *IEEE Control Systems Magazine*, vol. 27, no. 2, pp. 60-70, 2007.

[81] P. Sharer, A. Rousseau, S. Pagerit, and P. Nelson, "Midsize and SUV vehicle simulation results for plug-in HEV component requirements," *SAE*, paper 2007-01-0295, 2007.

[82] P. Sharer, A. Rousseau, D. Karbowski, and S. Pagerit, "Plug-in hybrid electric vehicle control strategy: comparison between EV and charge-depleting options," *SAE*, paper 2008-01-0460, 2008.

[83] B. T. Shaw, G. D. Fischer, and J. K. Hedrick, "A simplified cold-start catalyst thermal model to reduce hydrocarbon emissions," *IFAC 15th Triennial World Congress*, Barcelona, Spain, 2002.

[84] B. T. Shaw and J. K. Hedrick, "Closed-loop engine cold-start control to reduce hydrocarbon emissions," *Proc. of the American Control Conference*, Denver, Colorado, 2003.

[85] B. T. Shaw, "Modeling and control of automotive coldstart hydrocarbon emissions." Ph.D. dissertation, University of California, Berkeley, 2002.

[86] H. Shen, T. Shamim, and S. Sengupta, "An investigation of catalytic converter performances during cold starts," *SAE*, paper 1999-01-3473, 1999.

[87] C. M. Silva, M. Costa, T. L. Farias, and H. Santos, "Evaluation of SI engine exhaust gas emissions upstream and downstream of the catalytic converter," *Energy Conversion and Management*, vol. 47, no. 18, pp. 2811-2828, 2006.

[88] A. Simpson and T. Markel, "Cost-benefit analysis of plug-in hybrid electric vehicle technology," *22nd International Battery, Hybrid, and Fuel Cell Electric Vehicle Symposium and Exhibition*, Yokohama, Japan, 2006.

[89] C. Stephan and J. Sullivan, "Environmental and energy implications of plug-in hybrid-electric vehicles," *Environmental Science & Technology*, vol. 42, no. 4, pp. 1185-1190, 2008.

[90] J. Sun and N. Sivashankar, "Issues in cold start emission control for automotive IC engines," *Proc. of the American Control Conference*, Philadelphia, Pennsylvania, 1998.

[91] G. Tamai, M. A. Jeffers, C. Lo, C. Thurston, S. Tarnowsky, and S. Poulos, "Development of the hybrid system for the Saturn VUE hybrid," *SAE*, paper 2006-01-1502, 2006.

[92] E. Tate, J. Grizzle, and H. Peng, "Techniques for HEV Controller Synthesis," Ph.D. dissertation, University of Michigan, 2006.

[93] E. Tate, M. Harpster, and P. Savagian, "The electrification of the automobile: from conventional hybrid, to plug-in hybrids, to extended-range electric vehicles," *SAE*, paper 2008-01-0458, 2008.

[94] E. Tate and P. Savagian, "The CO_2 benefits of electrification E-REVs, PHEVs and Charging Scenarios," *SAE*, paper 2009-01-1311, 2009.

[95] S. Tomura, Y. Ito, K. Kamichi, and A. Yamanaka, "Development of vibration reduction motor control for series-parallel hybrid system," *SAE*, paper 2006-01-1125, 2006.

[96] K. Ueoka, Z. Mashiki, K. Maruyama, T. Ito, and M. Ito, "Hybrid system development for high-performance all wheel drive vehicle," *SAE*, paper 2007-01-0296, 2007.

[97] Union of Concerned Scientists, "The Plain English Guide to Tailpipe Standards," [online], Available at http://www.ucsusa.org/clean_vehicles/vehicle_impacts/cars_pickups_and_suvs/the-plain-english-guide-to.html

[98] U.S. Environment Protection Agency, [online] Available at http://www.epa.gov

[99] M. A. Wilcutts and J. K. Hedrick, "Model-based control for automotive cold start applications," *Vehicle System Dynamics*, vol. 45, no. 5, pp. 399-411, 2007.

[100] J.-S. Won, R. Langari, and M. Ehsani, "An energy management and charge sustaining strategy for a parallel hybrid vehicle with CVT." *IEEE Transactions on Control Systems Technology*, vol. 13, no. 2, pp. 313-320, 2005.

[101] J. C. Wurzenberger, G. Auzinger, R. Heinzle, and R. Wanker, “1D modeling of reactive fluid dynamics, cold start behavior of exhaust systems.” *SAE*, paper 2006-01-1544, 2006.

[102] G. Xizheng, W. Xuhui, L. Xu, Z. Feng, and L. Jun, “Vibration reducing in the process of engine start-stop for electric variable transmission,” *IEEE 6th IPEMC*, Hawaii, 2009.

[103] H. Yeo and H. Kim, “Hardware-in-the-loop simulation of regenerative braking for a hybrid electric vehicle,” *Proc. of the Institution of Mechanical Engineers*, vol. 216 Part D, 2002.

[104] T. Yoshioka and H. Sugita, “Noise and vibration reduction technology in hybrid vehicle development,” *SAE*, paper 2001-01-1415, 2001.

[105] J. C. Zavala, P. R. Sanketi, M. Wilcutts, T. Kaga, and J. K. Hedrick, “Simplified models of engine HC emissions, exhaust temperature and catalyst temperature for automotive cold-start,” *Fifth IFAC Symposium on Advances in Automotive Control*, Monterey Coast, California, 2007.

[106] E. Zgheib and D. Clodic, “CO_2 emissions and energy reduction evaluations of plug-in hybrid vehicles,” *SAE*, paper 2009-01-1324, 2009.

[107] J. Zhang, L. Chen, and G. Xi, “System dynamic modeling and adaptive optimal control for automatic clutch engagement of vehicles," *Proceedings of the Institution of Mechanical Engineers*, vol. 216, Part D, pp. 983-991, 2002.

[108] J. Zhang, X. Lu, L. Wang, S. Chen, and S. Li, “A study on the drivability of hybrid electric vehicle,” *SAE*, paper 2008-01-1572, 2008.